

## **Historic, Archive Document**

Do not assume content reflects current scientific knowledge, policies, or practices.



A99.9  
F7632U

C3



United States  
Department of  
Agriculture  
Forest Service

Rocky Mountain  
Forest and Range  
Experiment Station

Fort Collins,  
Colorado 80526

Research Paper  
RM-313



# RETENTION COPY

Provided by INFOSouth

INFOSouth  
MONTHLY ALERT  
MONTH Jan 94  
ITEM # 278

# Eddy Diffusivities for Sensible Heat, Ozone, and Momentum From Eddy Correlation and Gradient Measurements

K. F. Zeller



USDA  
NAT'L AGRIC LIBRARY  
RECEIVED  
FEB 3 '97

CURRENT SERIAL  
ACQ. / SERIALS  
BRANCH

## Abstract

The eddy-correlation measurement technique was used to obtain micrometeorological field measurements of the fluxes of momentum, sensible heat, and ozone at 3 and 8 meters at the Pawnee site. A method to accurately measure mass (ozone) gradients from surface-layer-based meteorological towers was developed and used. Both flux and gradient measurements were used for the determination of eddy diffusivities. Ozone was used as the mass tracer to explore similar relationships between the eddy diffusivities of momentum  $K_m$ , sensible heat  $K_h$ , and mass  $K_c$ .

Eddy-diffusivity ratios were computed using dimensionless-gradient ratios classified from the data and regression models. These ratios were classified by atmospheric stability determined at the geometric mean of the measurement heights.

The assumption of similarity between the eddy diffusivities of ozone and sensible heat,  $K_c = K_h$ , based on scalar turbulent transfer theory, was verified for unstable atmospheric conditions. Eddy diffusivities of sensible heat are, however, 50% greater than diffusivities of ozone for stable atmospheric conditions. Chemical reaction of ozone, and/or the need for flux-measurement corrections, decrease the resulting values for ozone diffusivities during stable periods. Established eddy-diffusivity ratios for water vapor and momentum are valid for ozone and momentum under stable atmospheric conditions over smooth terrain, but not under unstable conditions for flow disturbed by irregular terrain.

The relationships between the eddy diffusivities of momentum and ozone, as well as those between momentum and sensible heat, are controlled by free-convection conditions,  $K_m < K_c$  and  $K_m < K_h$ ; these results are inconclusive for unstable-atmospheric, smooth-terrain conditions for the Pawnee site during easterly winds. For disturbed-flow conditions at the Pawnee site during westerly winds, the eddy diffusivities for momentum were enhanced and both  $K_c/K_m$  and  $K_h/K_m$  become approximately constant (0.35 and 0.5, respectively) for both stable and unstable conditions.

Theoretical flux measurement corrections were applied to a subset of the data in an attempt to investigate the concept of a constant flux layer and to validate flux correction theory. The results indicate that flux corrections are warranted. However, improvements to flux correction theory are needed, especially for stable atmospheric conditions, as demonstrated by the significant increase in data variability as a result of these corrections. The "constant flux-layer" concept holds for momentum flux and sensible heat flux, but is questionable for ozone flux.

## Acknowledgments

This study was sponsored by the USDA Forest Service, Rocky Mountain Forest and Range Experiment Station. Support was also provided by the Environmental Protection Agency under Interagency Agreement DW12933093-01-0.

# Eddy Diffusivities for Sensible Heat, Ozone, and Momentum From Eddy Correlation and Gradient Measurements

K. F. Zeller, Meteorologist  
Rocky Mountain Forest and Range Experiment Station<sup>1</sup>

<sup>1</sup>Headquarters is in Fort Collins, CO in cooperation with Colorado State University. Paper is based on a thesis submitted to Colorado State University, in spring 1990.

## CONTENTS

	Page
MANAGEMENT IMPLICATIONS .....	1
INTRODUCTION .....	1
Governing Equations .....	1
Eddy Diffusivities .....	2
Goals and Hypotheses .....	2
SUMMARY OF PREVIOUS INVESTIGATIONS .....	3
Eddy Diffusivities .....	3
Eddy Correlation Flux Measurements .....	4
Surface-Layer Considerations .....	5
EXPERIMENTAL DESIGN .....	7
Field Site .....	7
Meteorological Measurements .....	8
Ozone Measurements .....	9
Ozone Analyzers .....	9
CAAM Response .....	9
CAAM Lag .....	9
Ozone Calibrations .....	10
TECO Response vs. Ambient Temperature .....	10
Ozone Depletion Due to NO <sub>x</sub> .....	11
RESULTS AND DISCUSSION .....	11
Gradients of Ozone, Temperature, and Horizontal Wind Speed .....	12
Variance of Ozone, Temperature, and Vertical Wind Speed .....	12
Surface Roughness .....	14
Fluxes of Ozone, Sensible Heat, and Momentum .....	14
Dimensionless Gradients of Ozone, Sensible Heat, and Momentum .....	17
Eddy Diffusivities of Ozone, Sensible Heat, and Momentum .....	19
CONCLUSIONS .....	24
Eddy Diffusivity Comparisons .....	24
Constant Flux Layer .....	25
Other Findings .....	25
Recommendations for Future Research .....	26
REFERENCES .....	26
APPENDIX A. DATA ACQUISITION AND HANDLING .....	30
Data Acquisition and Real-Time Computations .....	30
Data Editing .....	30
Ozone Gradient Determination .....	30
Flux Measurement Corrections .....	33
Effects of Heat and Water Vapor .....	33
Insufficient Averaging Time .....	34
Random Noise .....	34
Homogeneity and Stationarity .....	34
Sampling Height .....	35
Inadequate Fetch .....	35
Flow Distortion and Shadowing .....	35
Assumptions .....	35
Measurement Error .....	36
APPENDIX B. SPECTRA AND COSPECTRA .....	37
Temperature Spectra .....	37
Temperature Cospectra .....	37
Vertical Velocity Spectra .....	37
CAAM (Ozone) Spectra .....	38
CAAM (Ozone) Cospectra .....	39
APPENDIX C. DATA PLOTS .....	40
APPENDIX D. TABLE OF SYMBOLS .....	42

# Eddy Diffusivities for Sensible Heat, Ozone, and Momentum From Eddy Correlation and Gradient Measurements

K. F. Zeller

## MANAGEMENT IMPLICATIONS

Fluxes of trace gases ("greenhouse gases") in the atmospheric boundary layer have attracted the concerned interest of the scientific community because of the major climate changes projected for the present and the near future. Although concentrations of these trace gases are known and have been monitored for years, it is information on sources, sinks, and transport of these gases that is necessary for predicting future concentrations and the consequence of climate change. The measurement and analysis of fluxes and vertical gradients of ozone, as well as traditional micrometeorological fluxes of heat and momentum over long time periods, offer comparisons and better understanding of measured boundary layer eddy diffusivities of momentum, heat, and ozone. These measurements over dry grasslands provide region-specific fluxes, information on the transport behavior of ozone, and the documentation of how to make such flux measurements.

## INTRODUCTION

Since the mid 1960's with the advent of modern-environmental legislation, the horizontal transport and dispersion characteristics of the wind in the atmospheric surface layer have been studied and modeled with the goals not just of basic research, but of environmental management and protection. Modern environmental decisions have been based on modeled and measured pollutant concentrations within the ambient air (Cermak 1975; Kao 1984; Randerson 1984). Now, as a result of the "acid rain" issue, emphasis is being shifted to the amount of a pollutant delivered to and "taken up" by various components of the earth's surface: bare soil, water surfaces, biological canopy, or man-made or natural material surfaces (NRC 1983). The amount of a pollutant removed to a surface—mass per unit area per unit time—is the pollutant deposition flux. Knowledge of and predictions of pollutant deposition are required for acid rain related and other air pollutant related impact assessments. Deposition has consequently become an important consideration in recent modeling developments (Hicks 1984; NCAR 1985; Venkatram et al. 1988; Walcek et al. 1986; Walcek and Chang 1987). Deposition can be either "wet" or "dry," depending upon the delivery process. An air pollutant making its way to a surface without the aid of precipitation would be dry-deposited upon leaving the atmosphere.

The physical origin of the deposition of a pollutant,  $c$ , can be understood by visualizing its mass balance within any airshed as a simple control volume (McRea and Russell 1984):

$$\frac{\partial}{\partial t} \int_V c dv + \int_S \vec{F}_c \cdot \vec{n} ds - \int_V R dv = 0 \quad [1]$$

where the first term accounts for emissions of  $c$  [ $gm\ m^{-3}$  or parts per billion (ppb) by volume] integrated within the control volume,  $V$ ; the second term accounts for the flux  $\vec{F}_c$  [ $gm\ m^{-2}\ s^{-1}$ ], of  $c$  integrated across the boundaries  $S$  ( $\vec{n}$  is the unit normal) of the surface; and  $R$  is the rate of chemical production or reduction integrated within the control volume.

Assuming that the airborne pollutant in question is nonreactive and that it eventually exits the atmosphere at the earth's surface, the correct evaluation of the surface integral (second term) in [1] over the lower control volume boundary determines the ultimate correctness of the modeled scenario. The flux of material for a specified pollutant species  $c$  passing through the lower surface is its deposition flux  $F_c$ .

## Governing Equations

The expression for the concentration of a pollutant (scalar quantity) transported through a boundary layer is (Businger 1986; Rohsenow and Choi 1961):

$$\frac{\partial c}{\partial t} + \frac{\partial (u_i c)}{\partial x_i} = D_c \frac{\partial^2 c}{\partial x_i^2} + S \quad [2]$$

where

$c = c(t, x_i)$ , the instantaneous concentration (in  $gm\ m^{-3}$  or ppb) (Einstein's summation convention applies over repeated indices);

$u_i = u(t, x_i)$ , the instantaneous orthogonal components of wind velocity;

$D_c$  = the molecular diffusivity of  $c$ ; and

$S$  = a source or sink of  $c$ .

When the instantaneous concentration and instantaneous velocities are decomposed into their average,  $\bar{c}$ , and fluctuating or turbulent parts,  $c'$ , (i.e.,  $c = \bar{c} + c'$  and  $u_i = \bar{u}_i + u'_i$ ), and then combined and averaged, [2] becomes:

$$\frac{\partial \bar{c}}{\partial t} + \frac{\partial(\bar{u}_i \bar{c})}{\partial x_i} + \frac{\partial(\bar{u}'_i \bar{c}')}{\partial x_i} = D_c \frac{\partial^2 \bar{c}}{\partial x_i^2} + \bar{S} \quad [3]$$

Assuming steady-state, horizontal homogeneity, and no local sources or sinks allows the first, second, and fifth terms of [3] to be canceled leaving:

$$\frac{\partial \bar{w}' \bar{c}'}{\partial z} = D_c \frac{\partial^2 \bar{c}}{\partial z^2} \quad [4]$$

where  $w' = u'_3$  and  $z = x_3$ , the vertical wind velocity fluctuation and vertical distance coordinate, respectively. Integration of [4] between the earth's surface and height  $z$  yields a description of the vertical flux of  $c$  between those levels:

$$(\bar{w}' \bar{c}')_z - (\bar{w}' \bar{c}')_0 = D_c \left( \frac{\partial \bar{c}}{\partial z} \right)_z - D_c \left( \frac{\partial \bar{c}}{\partial z} \right)_0 \quad [5]$$

Since  $w'$  approaches zero at the surface,  $(\bar{w}' \bar{c}')_0$  is minimal and can be disregarded. Also  $(\bar{w}' \bar{c}')_z$ , the vertical turbulent transport at height  $z$  is many orders of magnitude greater than  $D_c (\partial \bar{c} / \partial z)_z$ , the vertical molecular diffusion transport at height  $z$ ; therefore, it can also be disregarded. This leaves the expression:

$$(\bar{w}' \bar{c}')_z = - D_c \left( \frac{\partial \bar{c}}{\partial z} \right)_0 \quad [6]$$

to describe the vertical transport, flux, or dry deposition of pollutant  $c$  (Businger 1986). Equation [6] is valid for any scalar (e.g., temperature, water vapor) given the same assumptions in the derivation. The surface molecular transport, second term in [6], cannot be measured directly (Businger 1986); therefore, the first term,  $\bar{w}' \bar{c}'$ , measured at height  $z$ , is the only opportunity to directly measure  $F_c$ , the vertical flux of  $c$ .

$$F_c = \bar{w}' \bar{c}' \quad [7]$$

The eddy correlation technique is used to measure the right-hand side of [7] directly, although indirect measurement techniques exist.

## Eddy Diffusivities

Specification of flux for momentum  $\tau$ , mass  $F_c$ , sensible heat  $H$ , and water vapor  $\lambda E$  have historically been based on the gradient (or profile) approach (Bache 1986; Munn 1966; Rosenberg 1974; Sellers 1965). The assumption is that the same type of equation for molecular diffusion transfer applies to turbulent transfer:

$$\tau = \rho K_m (\partial \bar{u} / \partial z) \quad [8a]$$

$$F_c = -K_c (\partial \bar{c} / \partial z) \quad [8b]$$

$$H = -\rho C_p K_h (\partial \bar{\theta} / \partial z) \quad [8c]$$

$$\lambda E = -\rho L K_v (\partial \bar{v} / \partial z) \quad [8d]$$

where  $K_m$  is the eddy (or turbulent) diffusion coefficient for momentum,  $K_c$  for ozone (mass),  $K_h$  for sensible heat, and  $K_v$  for water vapor;  $\rho$  is the density of air;  $\bar{v}$  is the average water vapor; and  $\bar{\theta}$  is the average potential temperature. The concept of an eddy diffusion coefficient for momentum is rooted in Prandtl's "mixing length theory" (Haltner and Martin 1957).

Two recent models have used the K approach. The Regional Acid Deposition Model, RADM (Chang et al. 1986; NCAR 1985), developed for EPA at NCAR, for instance, integrates [8b] as a starting point in the development of a method to calculate pollutant fluxes. In RADM,  $K_c$  is provided for through a similarity relationship with  $K_m$ . The Acid Deposition and Oxidant Model, ADOM (Venkatram et al. 1988), an internationally sponsored model similar to RADM, uses the same approach.

The recommended engineering approach to specifying  $K_c$  for ozone or for any other airborne mass is to assume the principle of similarity (Galbally 1971; Munn 1966; Oke 1978; Rider and Robinson 1951; Sellers 1965):

$$K_c = K_h = K_v = \alpha K_m \quad [9]$$

where  $\alpha$  is a constant ( $\sim 1.35$ ) for stable atmospheric conditions and a function of stability for unstable atmospheric conditions (Businger 1986).

## Goals and Hypotheses

This paper investigates exchange processes between the atmosphere's surface layer and the earth's surface. Pollutants are transported from the earth's air-surface layer to an underlying surface. Measurements of surface-layer fluxes and vertical gradients of sensible heat, ozone, and momentum were acquired over a relatively flat-terrain, shortgrass steppe prairie (Zeller et al. 1989). Diffusivities obtained directly from these measurements are compared to established empirical relationships, and the similarity assumptions, [9], are evaluated.

Mass diffusivities, such as the diffusivity for ozone, are used by the scientific and engineering communities to describe the diffusion of mass through the atmosphere. The results presented in this paper can be used to improve pollution impact assessments and to help establish relationships between pollutants and the damage they cause. More clearly understood and specifically defined mass diffusivities, for example, will more accurately account for actual mass deposition of pollutants.

This study had two main objectives:

1. To investigate the validity of using eddy diffusivities of sensible heat or momentum to specify the eddy diffusivity for ozone under various atmospheric stabilities.

- To investigate the assumption of a constant vertical flux layer for heat, momentum, and ozone within the lower atmospheric surface layer.

My aim was to investigate time-honored assumptions that are commonly used, but as yet have not been completely verified by experimental methods. In fact, attempts to prove or disprove these assumptions have met with mixed results (Businger 1986). The data collected at the Pawnee site were culled and edited to provide representative data records, which were then used to calculate and analyze dimensionless gradient, eddy diffusivity, and atmospheric stability quantities. Objective 1 was evaluated by comparing measured results and regression models of the measured results with accepted empirical theories for smooth terrain at various atmospheric stabilities. Objective 2 was evaluated by comparing pairs of observed corrected and uncorrected fluxes at two levels with the expected ratio of 1:1.

## SUMMARY OF PREVIOUS INVESTIGATIONS

### Eddy Diffusivities

Flux equations [8a-d] are the turbulent analogies to the basic physical law relating molecular viscosity to molecular diffusion. The eddy diffusivity (also called eddy viscosity, eddy exchange coefficient, and austausch coefficient)  $K_m$  is the turbulent analogy to Newton's law for molecular viscosity. The eddy diffusivities  $K_c$ ,  $K_h$ , and  $K_v$  are the eddy diffusivities analogous to Fourier's and Fick's laws for the molecular diffusion coefficients for mass, heat, and water vapor. The units of these coefficients are the same,  $\text{cm}^2\text{s}^{-1}$ ; however, the eddy diffusivities are several orders of magnitude greater than their molecular counterparts. Eddy diffusivities are based on assumptions about the similarity between molecular and turbulent transfer, not on sound physical laws (Arya 1988). They are properties of the flow, not simply fluid properties. Therefore, variations in measured  $K_q$ 's are expected as the atmospheric-surface-layer characteristics change.

Based on scaling arguments, Lettau (1951) limits the value of  $K_m$  to a maximum of  $10^8 \text{ cm}^2\text{s}^{-1}$ , and he predicts that  $K_m$  will vary from  $\sim 1$  to  $\sim 10^6 \text{ cm}^2\text{s}^{-1}$  between the earth's surface and 1-km height. Jacobi and André (1963) provide estimated height-dependent  $K_m$  values ( $\text{cm}^2\text{s}^{-1}$ ) based on atmospheric stability:

Height	Stability			
	Inversion	Stable	Neutral	Unstable
3 m	30	250	5,500	55,000
8 m	80	790	16,000	160,000

Given temperature and mass are both scalars, heat and mass transfer by the turbulent atmosphere should be similar, hence the expected ratio  $K_h/K_c$  is 1. Empirical data for various flows indicate that the ratio  $K_h/K_m = \alpha$  should be in the range 0.5 and 1 (Bird et al. 1960); however, based on atmospheric experiments,  $\alpha$  depends on stability and, as presented above, is sometimes estimated as 1.35 for stable conditions. Businger et al. (1971) provide an empirical relationship for the ratio  $\alpha$  as a function of atmospheric stability:

$$\alpha = \frac{1.35(1-9\zeta)^{1/2}}{(1-15\zeta)^{1/4}} \text{ for } \zeta < 0 \text{ (unstable)} \quad [10]$$

$$\alpha = \frac{(1+4.7z)}{(0.74+4.7z)} \text{ for } z > 0 \text{ (stable)}$$

where

$$\zeta = z/L, \text{ an atmospheric stability parameter;}$$

$$z = \text{height above ground; and}$$

$$L = \text{the Monin-Obukhov length, [13].}$$

Based on [10],  $\alpha$  is equal to 1.35 only when  $\zeta=0$ , then it quickly drops to  $\sim 1$  for  $\zeta>0$ . An earlier empirical result given by Swinbank (1968),  $\alpha=2.7\zeta^{0.25}$ , for  $\zeta<0$  better describes the Pawnee site results.

In an attempt to preview the behavior of  $K_c/K_m$ ,  $K_v/K_m$  is used here to represent a "mass" diffusivity as opposed to  $K_h/K_m$ . Rosenberg (1974) provides an empirical relationship for the ratio of  $K_v/K_m$  as a function of atmospheric stability based on experiments by Pruitt et al. (1971):

$$K_v/K_m = 1.13(1-60Ri)^{0.074} \text{ Ri}<0.017 \text{ (unstable)} \quad [11]$$

$$K_v/K_m = 1.13(1+95Ri)^{-0.11} \text{ Ri}<-0.011 \text{ (stable)}$$

where

$$Ri = \text{the gradient Richardson number,}$$

$$\text{another stability parameter, [14].}$$

Note that an asymptotic overlap exists in [11] around  $Ri=0$ . Panofsky and Dutton (1984) use the approximations  $\zeta=Ri$  for  $\zeta\leq 0$  and  $\zeta=Ri/(1-5Ri)$  for  $\zeta>0$ . Equations [10] and [11], the ratio  $K_h/K_v$ , [10] divided by [11], and  $\alpha=2.75\zeta^{0.25}$  are plotted in figure 1 as functions of  $\zeta$ . Figure 1 shows that the eddy-diffusivity similarity assumption, [9], does not hold exactly based on data reported in the literature, as the empirically determined ratio  $K_h/K_v$ , is not precisely 1. The ratio  $K_h/K_v$  reaches a constant value of 1.2 for  $\zeta>1$  and is still increasing at the value 1.8 for  $\zeta<-5$ . The ratio  $K_h/K_v$  plotted in figure 1, different from unity, is a good preview estimate based on reported data available for  $K_h/K_c$  because both  $K_c$  and  $K_v$  are mass diffusivities different from  $K_m$  and  $K_h$ , momentum and heat diffusivities.

Eddy-diffusivity similarity, [9], is used throughout the technical literature (e.g., Businger 1986). A variety

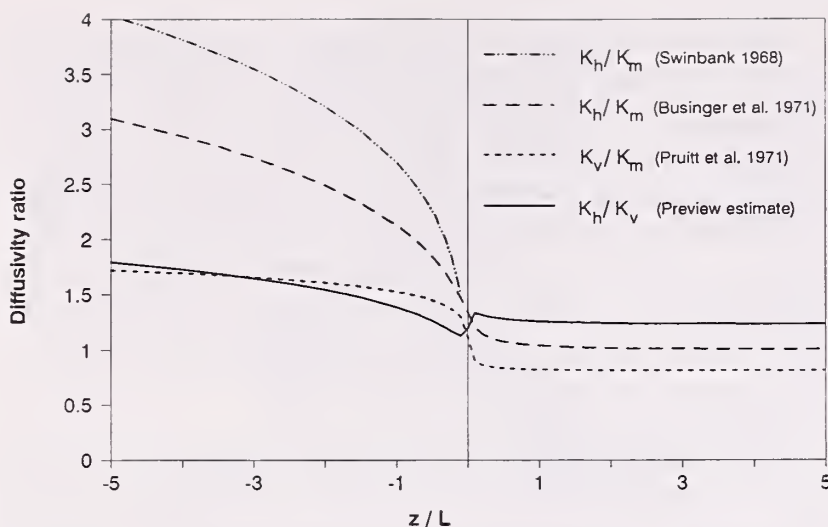


Figure 1—Empirically derived eddy diffusivities vs. stability parameter ( $z/L$ ).

of techniques can be used to estimate  $K_c$ . For instance, by specifying  $K_h = K_v$ ,  $H$  and  $\lambda E$  can be determined through [8c] and [8d] using the Bowen ratio method (Rosenberg 1974), which involves measuring the surface energy-balance components using well-proven, reliable instruments. Once  $\lambda E$  or  $H$  are known, either [8c] or [8d] with either calculated  $K_h$  or calculated  $K_v$  can be used to specify  $K_c$  by [9] (Sellers 1965). In another approach,  $\lambda E$  and  $H$  are determined by calculating  $\tau$  using the logarithmic wind profile and assuming the similarity relationship with  $\alpha K_m$  and the other eddy diffusivities, [9].

The mass eddy diffusivity  $K_c$  and flux  $F_c$  can also be estimated by applying a modified Bowen ratio, a gradient technique that involves measuring  $\partial \bar{C} / \partial z$ ,  $\partial \theta / \partial z$ ,

and  $H$ , then using [8b] with the similarity assumption. This approach has been used by many (Droppo 1985; Woodruff 1986); however, concentration differences measured over short vertical distances are difficult to resolve because of limited instrument resolution. To circumvent this limitation, one instrument is typically used with the sampling-intake height switched periodically between the chosen  $\delta z$  levels over the data averaging period (Businger 1986). Woodruff (1986) quantified errors up to 32% using this approach to the gradient technique.

Table 1, a review of experimental results from current literature, shows a paucity of  $\partial \bar{C} / \partial z$  data are available from which to estimate  $K_c$ . This paper includes the development of a better technique to measure  $\partial \bar{C} / \partial z$  specifically for ozone that will be applicable to other trace gases.

All of the methods that employ [8b] for determining  $K_c$  and  $F_c$  use the similarity assumption [9]. All of the acid deposition models developed to date use the similarity assumption, although proof of this assumption through experiment has not been thoroughly explored.

## Eddy Correlation Flux Measurements

The direct measurement of the flux  $w'c'$ , [7], is called the eddy correlation technique. It has long been considered the most reliable (Arya 1988) and most fundamental approach to flux measurements as mass, heat, and momentum are primarily transported by tur-

Table 1. — Ozone flux experiments.

Reference	Method*	Sample height location	Instruments	Sample freq. (Hz)	EC: (ppb m s <sup>-1</sup> )	Measured range GR: (ppb m <sup>-1</sup> )	V <sub>d</sub> : (cm s <sup>-1</sup> )
Delany et al. (1986)	EC	4 & 8 m	Chemiluminescence, sonic anemometer	10	0 to -0.7		
Droppo (1985)	EC	9.1 m	Chemiluminescence, uvw Gill anemometer	?	0 to -0.55		
	GR	0.75 & 5.5 m				-0.55 to 3.38	
Lenschow (1982)	EC/V <sub>d</sub>	Aircraft	Chemiluminescence	?			-0.05; 1.0
Meyers & Yuan (1987)	EC/V <sub>d</sub>	?	Summary report	?			0 to -0.04 (daily average)
Wesely et al. (1982)	EC/V <sub>d</sub>	5.2 m	Chemiluminescence, assume: uvw Gill	20			-0.05 to -0.3
Wesely et al. (1981)	EC	5 to 8 m (winter)	Chemiluminescence, uvw Gill	?			-0.01 to -0.13
Wesely et al. (1978)	EC	4 & 5 m	Chemiluminescence, uvw Gill	?			-0.2 to -0.55
Zeller et al. (1989)	EC	6 m uvw Gill	Chemiluminescence,	14	0 to -0.5		0 to -0.7
Zeller & Hazlett (1989)	EC	6 m sonic anemometer	Chemiluminescence,	14	0 to -0.3		0 to -0.35

\* GR: gradient  
EC: eddy correlation flux

EC/V<sub>d</sub>: eddy correlation with only deposition velocity reported ( $V_d = F_c / \bar{C}$ )  
?: not specified in report.

bulent motion. The eddy correlation method also provides the means to measure sensible heat flux  $H$ , and momentum flux  $\tau$ , directly:

$$H = \rho C_p \overline{w' \theta'} \quad [12a]$$

$$\tau = \rho \overline{u' w'} \quad [12b]$$

Requirements for valid eddy correlation measurements are stringent. Until the recent advent of fast-response chemical sensors and real-time data processing, eddy correlation was a preferred method in theory only. The data sampling rate has to be fast enough to measure most of the eddies contributing to the flux. According to Kaimal (1975) and his co-workers (Kaimal et al. 1972) a sampling frequency of about 10 Hz or greater is needed for typical surface-layer measurements that they consider valid for sampling heights above 3 meters. Below 3 meters the larger transporting turbulent eddies are restricted by the earth's surface, and some degradation in the measured flux can be expected because of instrument resolution when sonic anemometers are used (Haugen et al. 1971; Kaimal 1969). Although in theory ensemble averages are assumed when developing working [3]-[7], in practice they cannot be achieved and are replaced by time averages assuming homogeneous and stationary turbulence (Panofsky and Dutton 1984). Based on field experience, the averaging period for eddy correlation data collection should be between 0.25 and 1 hour; short enough to maintain stationarity, but long enough to capture the dominant energy contributing eddies that contribute to the surface-layer flux (Brutsaert 1988). Sampling details are examined in greater detail in appendix A.

To sample at 10 Hz or faster, fast-response sensors with short-time responses are required (Arya 1988). Restrictions on sensor size, placement, and sensing-element geometry also exist (Businger 1986). In cases where sensors are not exactly matched, are not collocated, do not sample a single point, or cause flow distortions, flux measurements can fall short of true values. In such cases, theoretically based transfer functions can be used to correct flux measurements to obtain the correct flux (Kristensen and Fitzjarrald 1984; Moore 1986; Zeller et al. 1989). (These transfer coefficients are detailed in appendix A, Zeller et al. 1989; Zeller 1990). In practice, however, correcting flux data can add considerable scatter to the results. It is therefore appropriate to design flux measurements in such a way as to eliminate these potential problems as much as possible (Wyngaard, 1989a).

The assumptions that lead to [4] require that eddy correlation measurements be made above flat, uniform terrain. In practice, flat, expansive, uniform terrain will provide an adequate fetch so that horizontal homogene-

ity can be assumed within a reasonable degree of error. Because most sites are not perfectly uniform and an ensemble average cannot be obtained, the vertical component in the second term of [3] is not always zero (i.e.,  $\overline{w} \neq 0$ ). Recent theoretical developments have allowed for some relaxation of this requirement by employing coordinate rotation forcing  $\overline{w} = 0$  (Wesely 1970), thus adjusting the measured eddy correlation to the value perpendicular to the mean calculated wind-flow streamline, (which is not always parallel to the earth's surface) for the sample period. This approach retains the validity of [7] and has been found reliable for calculated streamlines within  $\pm 5$  degrees of the surface plane (McMillen 1986).

Within the last decade several researchers, including this writer, have attempted to measure ozone fluxes by the eddy correlation and the gradient methods. Table 1 gives a representative list of these, including the investigator, method, sampling height, instruments used, sampling frequency, and general results (order of magnitude) in terms of either  $F_c$  for flux,  $\partial \bar{c} / \partial z$  for mass gradient, or  $V_d = F_c / \bar{c}$  for deposition velocity. Data reported herein are within the same orders of magnitude as reported in previous studies (table 1).

## Surface-Layer Considerations

As stated previously, eddy diffusivities describing turbulent transfer are functions of the fluid flow. Understanding the vertical flux or dry deposition of a mass to a surface, such as ozone to a shortgrass steppe prairie canopy, therefore, requires a knowledge of the flow properties or, in this case, the micrometeorological variables just above the surface being investigated. Monin-Obukhov (M-O) surface-layer similarity was the micrometeorological concept used to provide insight for studying the behavior of surface-layer turbulence (Wyngaard 1973). The basic premise for mean flow and turbulent characteristics proposed by Monin and Obukhov in 1954 for a horizontally homogeneous surface is that they depend on only four variables:  $z$ , the height above the surface;  $u_*$ , the friction velocity;  $H/\rho C_p$ , the surface kinematic heat flux; and  $g/T$ , a buoyancy variable. Here  $g$  is the acceleration due to gravity and  $u_*$ , the friction velocity, defined as  $(-u' w')^{1/2}$ . As these four M-O variables are constituted by only three fundamental dimensions—length, time, and temperature—Buckingham's PI theorem demands that only one independent dimensionless parameter can be formed by them. Obukhov chose the buoyancy length scale,  $L$ , in 1946 as the most appropriate (Arya 1988):

$$L = \frac{-u_*^3 \bar{T}}{kg \overline{w' \theta'}} \quad [13]$$

where  $\overline{w'\theta'} = H/\rho Cp$ . Since  $\overline{w'T'}$  was measured at the Pawnee site  $w'\theta' \approx 1.05$   $w'T'$  for 1,641 meters elevation is used to calculate  $L$ . When the height aboveground,  $z$ , is small compared to  $L$ , mechanical turbulence generated by wind shear prevails. For  $z > |L|$ , buoyancy effects start to outweigh mechanical effects (Clarke et al. 1982). Hence  $z/L = \zeta$  is an important buoyancy or atmospheric stability parameter and is traditionally used in most modern micrometeorological studies. As  $u_*$  and  $H$  have been difficult to measure directly, the gradient Richardson number ( $Ri$ ) stability parameter is often measured and used to indirectly calculate  $\zeta$  through the empirical relationships given in Panofsky and Dutton (1984) Chapter II:

$$Ri = \frac{g \frac{\partial \bar{\theta}}{\partial z}}{\bar{\theta} \left( \frac{\partial \bar{u}}{\partial z} \right)^2} \quad [14]$$

The M-O similarity theory predicts that the dimensionless wind shear, the dimensionless sensible heat gradient, and the dimensionless mass gradient are all universal functions of  $\zeta$  (Arya 1988; Busch 1973):

$$\frac{kz}{u_*} \cdot \frac{\partial \bar{u}}{\partial z} = \phi_m(\zeta) \quad [15a]$$

$$\frac{kz}{\theta_*} \cdot \frac{\partial \bar{\theta}}{\partial z} = \phi_h(\zeta) \quad [15b]$$

$$\frac{kz}{c_*} \cdot \frac{\partial \bar{c}}{\partial z} = \phi_c(\zeta) \quad [15c]$$

Here  $k$  = von Karman constant, a universal constant empirically derived from the “law of the wall” when  $\phi_m(0) = 1$ ;

$$\theta_* = \frac{\overline{w'\theta'}}{u_*}, \quad \text{the surface-layer temperature scale;}$$

$$c_* = \frac{\overline{w'c'}}{u_*}, \quad \text{the surface-layer ozone concentration scale;}$$

$$\frac{\partial \bar{\theta}}{\partial z} = \bar{\theta} \left( \frac{\partial \bar{T}}{\partial z} + \Gamma \right) \quad \text{the potential temperature gradient; and}$$

$$\Gamma = \quad \text{the adiabatic lapse rate.}$$

The empirical forms for  $\phi_m$  and  $\phi_h$ , determined from many field studies, are the subject of past and ongoing research (Brutsaert 1988; Fazu and Schwerdtfeger 1989; Högström 1988; Pruitt et al. 1971; Yaglom 1977):

$$\phi_m = \begin{cases} (1-b_1\zeta)^{-1/4} & \text{for } \zeta < 0 \quad (\text{unstable}) \\ 1+b_2\zeta & \text{for } \zeta \geq 0 \quad (\text{stable}) \end{cases} \quad [16a]$$

$$\phi_h = \begin{cases} b_3(1-b_4\zeta)^{-1/2} & \text{for } \zeta < 0 \\ b_1+b_2\zeta & \text{for } \zeta \geq 0 \end{cases} \quad [16b]$$

The relationships established from the 1968 Kansas Experiment are generally used (Arya 1988; Businger et al. 1971) and will be used here to compare the Pawnee site results with existing empirical theory. The following values were established for a flat grassland canopy and represent the case for smooth terrain:  $b_1 = 15$ ;  $b_2 = 4.7$ ;  $b_3 = 0.74$ ; and  $b_4 = 9$ . Typically,  $\phi_c$  is taken to be equal to  $\phi_h$ , which again is the similarity assumption.

Velocity, temperature, and mass profiles are determined by integrating [15a-c] with respect to height,  $z$  (Arya 1988):

$$\bar{u} = \frac{u_*}{k} \left[ 1n \frac{z}{z_0} - \psi_m(\zeta) \right] \quad [17a]$$

$$\bar{\theta} = \theta_0 + \frac{\theta_*}{k} \left[ 1n \frac{z}{z_0} - \psi_h(\zeta) \right] \quad [17b]$$

$$\bar{c} = \bar{u} = \frac{u_*}{k} \left[ 1n \frac{z}{z_0} - \psi_m(\zeta) \right] \quad [17c]$$

where  $z_0$ , the surface roughness, is a constant of integration evaluated at  $\bar{u} = 0$ . It is typically smaller in value compared to the physical height of the surface elements causing it. The temperature and mass concentration at  $z_0$  are  $\theta_0$  and  $c_0$ . The functions  $\psi_i(\zeta)$  are similarity functions related to  $\phi_i(\zeta)$  (Arya 1988):

$$\psi_i(z) = \int_{\zeta_0}^{\zeta} [1 - \phi_i(\zeta)] \frac{d\zeta}{\zeta}$$

so that

$$\psi_h = \psi_m = \psi_c = -5\zeta \quad \text{for } \zeta \geq 0 \quad [18a]$$

$$\psi_m = 1n \left[ \left( \frac{1+x^2}{2} \right) \left( \frac{1+x}{2} \right)^2 \right] - 2 \tan^{-1} x + \frac{\pi}{2} \quad \text{for } \zeta < 0 \quad [18b]$$

$$\psi_h = \psi_c = 2 \cdot 1n \left( \frac{1+x^2}{2} \right) \quad \text{for } \zeta < 0 \quad [18c]$$

where  $x = (1-15\zeta)^{1/4}$ .

The above relationships for  $\bar{u}$  and  $\psi_m$  in [17a] and [18b] are used to establish  $z_0$  for the Pawnee study site discussed in this paper.

## EXPERIMENTAL DESIGN

### Field Site

The data analyzed were obtained at the USDA Forest Service Pawnee eddy-correlation research site. The Pawnee site (fig. 2) is 50 km northeast of Fort Collins, Colorado, at the Central Plains Experimental Range (CPER), a research area adjacent to and west of the Pawnee National Grasslands. The CPER is a 6,500-ha area of shortgrass prairie that is administered by the USDA Agricultural Research Service. Also located at the CPER is a long-term ecological research (LTER) station managed by Colorado State University (CSU) and funded by the National Science Foundation. The exact location of the eddy-correlation measurement site is within a 6-ha grazing enclosure in Weld County: section 27, 1,641 m elevation, latitude  $40^{\circ}28'23''$  N, and longitude  $104^{\circ}45'15''$  W. The enclosure was established in 1969 as an appropriate and "representative" site for meteorological measurements. The area is mostly level, bordered on all sides by gently undulating plains, and is not near major ridges or bluffs that would seriously influence measurements. There is, however, a drainage swale—Little Owl Creek—that runs north-south ca. 400 m west of the meteorological tower. This swale demonstrated an effect on the momentum gradient data, as discussed later. A complete discussion of the site, including biota and climate, is given by Zeller et al. (1989).

Figure 3 is a photograph of the physical layout of the site, which includes: a 10-meter meteorology tower

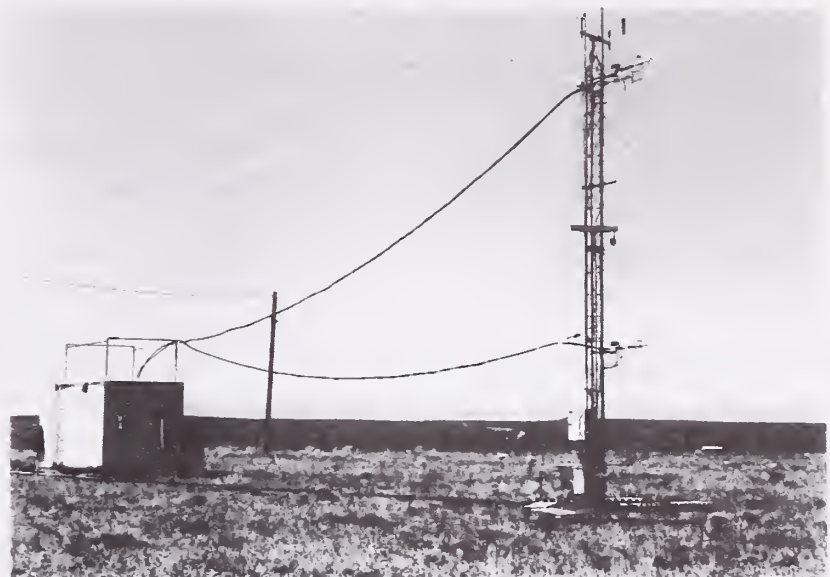


Figure 3—Pawnee site meteorological tower and instrument shelter.

equipped with micrometeorological sensors at 8 and 3 meters; an instrument shelter located 21 m southwest ( $21^{\circ}$  true north (TN) azimuth) of the tower; fast- and slow-response chemical ozone sensors; a personal computer; data acquisition system; and the plumbing and wiring necessary to sample the air at the tower adjacent to the meteorological sensors. A schematic of the site is given by Zeller et al. (1989) (fig. 1). Table 2 lists the major instrumentation used to collect the data used in this analysis. The following sections present further discussions of these instruments, and possible chemical and temperature effects on ozone measurements. Data acquisition and real-time computations made during data acquisition are discussed in appendix A. Measure spectra and cospectra are presented in appendix B.

The Pawnee site was operated on a weekly Tuesday morning to Tuesday morning basis to correspond with other acid deposition related programs and experiments

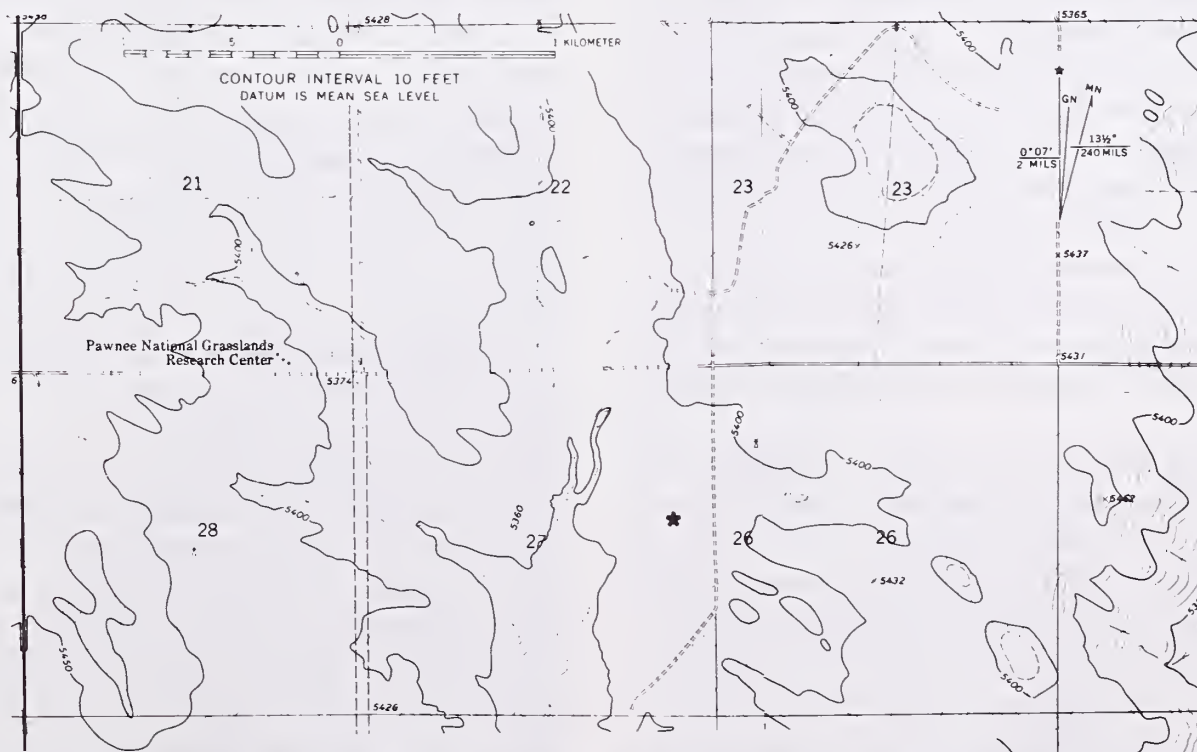


Figure 2—Topographic map of Pawnee site area and Pawnee site (\*) location.

Table 2. — Instrumentation used at Pawnee site.

Instrument or model	Type	Quantity	Response time	Range
Denver University CAAM (1 & 2)	Chemiluminescence	Ozone flux	0.5 s	0.2 to 400 ppb
TECO 49 (1 & 2)	UV adsorption	Ozone concentration, ozone gradient	2 min	1.0 to 500 ppb
AIR, Inc. Model FT-1AO-T	Platinum resistance	Temperature	0.01 s (4 m s <sup>-1</sup> wind)	-50 to +50°C
Atmos. Tech. Inc. Model BH-478/B3	3-axis sonic	Wind velocity momentum flux	0.05 s	0 to 20 m s <sup>-1</sup>
Compaq 386/20	PC computer (80386)	Data collection and processing		
Data Translations, Inc.	DT2805 board	A/D conversion		0 to 10 v
Thermocouple	copper-constantan	Temperature gradient		± 10°C

involving weekly averaged samples requiring adherence to national acid-deposition, data-collection protocols. Therefore, weekly calibrations, routine maintenance, sensor chemical reagent changes, and data archival were always accomplished on Tuesday mornings.

### Meteorological Measurements

The eddy-correlation approach to measuring the vertical fluxes of momentum, heat, and mass requires simultaneous measurements of vertical velocity fluctuations, sensible heat fluctuations, and chemical mass fluctuations. Figure 3 shows the eddy-correlation instrumentation at 8 and 3 meters. The fast-response measurements required to capture the eddy fluctuations were routinely made at  $14 \pm 1$  Hz. Wind sensors, temperature sensors, and chemical sensors must all have short response times to respond at this sampling rate, which requires very sensitive transducers. All sensors, however, have measurement limitations that must be considered and accounted for. This is particularly true for eddy-correlation instruments (Businger 1986) because the ability to measure eddy fluctuations is limited by sensor response. Specific corrections for measured limitations that can be applied to eddy-correlation flux data are presented in appendix A and elsewhere (Zeller et al. 1989).

Scalar gradient data were acquired using slower response sensors. Temperature-gradient measurements were made with 3-mil copper-constantan thermocouples connected in series. Solar heating of the thermocouples was accounted for in the results. Ozone gradient measurement are discussed in appendix A. Wind gradients were obtained from average sonic-anemometer data.

It is appropriate to investigate the response of the meteorological and chemical sensors as a function of

frequency in order to evaluate the ability of each sensor/data-logging combination to detect the full range of energy-containing eddies. This is accomplished by transforming a time series data record, e.g., the vertical velocity component  $w(t)$  or any other measure  $q(t)$  as a function of real time to its power spectrum, a function of frequency. In this way the measured variance density at each frequency can be examined and compared to  $M_0$  similarity predictions:

$$\overline{q'^2} = \int_0^\infty S_q(f) df = \int_0^\infty f S_q(f) d \ln f \quad [19]$$

where

$$\begin{aligned} S(f) &= \text{special density;} \\ f &= \text{frequency (s}^{-1}\text{); and} \\ q &= \text{measured quantity.} \end{aligned}$$

Equation [19] assumes that a temporal record can be used to represent the spatial "size" of turbulent eddies. This assumption, that means and variances measured in time are equal to those measured in space, is Taylor's "frozen wave" hypothesis and is valid for stationary-homogeneous turbulence (Panofsky and Dutton 1984).

During the measurement program, half-hour time series records of instantaneous or "raw" time series data were collected at either ca. 40 Hz or ca. 14 Hz. These data were translated to the frequency domain using the fast Fourier transform (FFT) and power-spectrum Fortran programs provided in "Numerical Recipes" (Press et al. 1986). The data-handling approach, normalizations, and data presentations are similar to those used by Kaimal et al. (1972): block averaging was applied to the spectra and cospectra. Individual spectra,  $S(f)$ , are typically normalized and plotted as  $f S(f) / q_*^2$  vs.  $fz / \bar{u}$  on a log-log plot, where  $fz / \bar{u}$  is the nondimensional

frequency. Monin-Obukhov similarity predicts a  $-5/3$  slope in the inertial subrange for both velocity and scalar spectra when plotted against frequency. This translates to a  $-2/3$  slope for  $fS(f)$  plotted against frequency. Temperature, vertical velocity, and ozone power spectra are presented in appendix B along with vertical velocity-temperature cospectra and vertical velocity-ozone cospectra.

### Ozone Measurements

By combining [7] and [8b], the eddy diffusivity for ozone can be determined by measuring both the flux by eddy correlation and the concurrent ozone gradient:

$$K_c = \frac{-F_c}{\left( \frac{\partial \bar{c}}{\partial z} \right)} \approx \frac{-\overline{(w'c')} \Delta z}{\Delta \bar{c}} \quad [20]$$

The measurement of  $w'c'$  by eddy correlation requires a fast-response chemical sensor. The  $\Delta \bar{c} = \bar{c}(8 \text{ m}) - \bar{c}(3 \text{ m})$  measurement is very sensitive to both instrument accuracy and precision. Ozone measurements at the Pawnee site were made with four ozone instruments (see table 2), two fast-response chemiluminescent ambient air monitors (CAAM), and two slow-response Thermo Electron Corp. (TECO) model 49 UV absorption ambient air monitors.

### Ozone Analyzers

The TECO 49 ozone analyzer has been used for years in environmental monitoring programs and is known for its stability (TECO 1986). It can provide a very precise and relatively accurate continuous ozone record month after month. It has been accepted by the U.S. Environmental Protection Agency as an "equivalent method" (EQA-0880-047). The TECO 49 measures the extinction of 254 nm wavelength light by ozone. Beer's law with corrections for pressure and temperature is used to calculate the ozone concentration in parts per billion (ppb). The TECO measures mixing ratio as opposed to mass per volume.

The CAAM ozone analyzer is a prototype instrument developed and constructed by Dr. Donald Stedman of the University of Denver. Its response is linear to the number of ozone molecules in the sample air stream (i.e., mass per volume). Due to its sensitivity, it is not as accurate over long time periods as the TECO 49; however, its linear response gives it a relative precision that allows for its use in measuring ozone fluctuations. The CAAM uses a blue-sensitive photomultiplier tube to detect the light produced by the reaction of ozone with the chemiluminescent dye eosin-y mixed in solution with water, ethylene glycol, and copper nitrate. For

more detail on the CAAM, see Ray et al. (1986), and appendix A in Zeller et al. (1989).

### CAAM Response

The square-wave response time to an ambient-air to clean-air step change for the CAAM analyzer, assuming a first-order sensor, was measured in the laboratory to be about 0.14 second. In situ this response time deteriorated to either 0.7 second if the step change of clean air was introduced at the tower end of the 20 m intake line, or 0.3 second if the step change of clean air was introduced at the intake manifold just prior to entering the CAAM. Figure 4 shows both these response times. Diagrams and details are provided in Zeller et al. (1989). For the ozone flux correction considerations, a time response of 0.5 second was used as representative of the actual response time seen by the CAAM as the intake line is actually in equilibrium with the ambient air during routine sampling but tends to adsorb and desorb during zero air tests.

### CAAM Lag

The sample transfer time for a sample of air to travel from the tower inlet to the CAAM was ca. 2 seconds. This transfer time depended on the flow rate of the high-volume pump and the time-in-use of the pump filters. The flow rate averaged ca. 155 liters per minute, which included the additional time from the intake manifold inside the instrument shelter to the CAAM instrument itself. Since the measure  $w'c'(t)$  requires simultaneous values at any given  $t$  for both  $w'(t)$  and  $c'(t)$ , it was important to know the lag time required for the sampled air to be detected. The lag time was checked for both intake lines routinely on Tuesday mornings and incorporated into the flux calculations. The lag time for both instruments remained constant within  $\pm 0.05$  seconds throughout the study. The initial 2 seconds shown on figure 4 is the lag time, as the data recording for the data plotted commenced with the injection of zero air at the

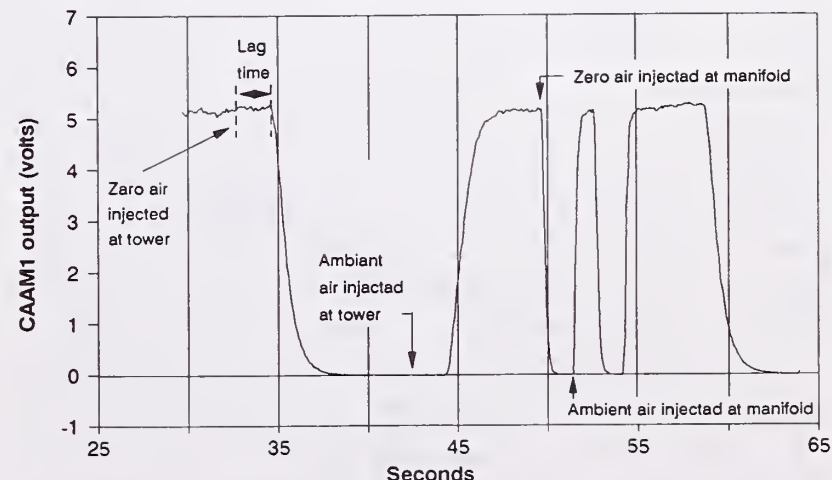


Figure 4—CAAM signal response to square-wave ozone input—April 23, 1989 (13:48 MST)

tower. The dampening of turbulent fluctuations of ozone in the intake tube was found to be insignificant relative to measurement of atmospheric turbulent fluxes (Massman 1991).

## Ozone Calibrations

The TECO 49 ozone analyzers were calibrated on a weekly basis with a primary standard ozone analyzer maintained by the USDA Forest Service, Rocky Mountain Range and Experiment Station, strictly for the purpose of ozone calibrations. The local Forest Service primary standard instrument is a TECO model 49PS. This instrument is traceable to, and compared yearly, with an official EPA ozone standard.

The CAAM ozone analyzers were calibrated continuously against the TECO analyzers. For each half-hour period, the average CAAM output signal was compared with the average output of the TECO sampling the same air arriving through the same intake manifold. Figure 5 is an example of the data scatter between the half-hour average TECO1 and CAAM2 outputs for the 1-week period between Tuesday morning June 27, 1989 and Tuesday morning July 4, 1989. The two TECO 49 and two CAAM ozone analyzers were named TECO1, TECO2, CAAM1, and CAAM2 at the Pawnee site for calibration and maintenance purposes. The CAAM instruments were calibrated to the TECO instruments on a half-hour to half-hour basis because the TECOs were very stable over a 1-week period whereas the CAAMs were not as stable over the same period (note there is some scatter in fig. 5). The CAAM/TECO calibrations were done after TECO1 and TECO2 analyzers were aligned with each other to provide for accurate  $\partial \bar{c} / \partial z$  ozone gradient data. The alignment procedure is described in appendix A.

Figure 6 is an example of a nine-point calibration of a CAAM with a TECO when each instrument was compared against known ozone concentrations under controlled conditions. The figure demonstrates the linear response of the CAAM instrument; however, the cali-

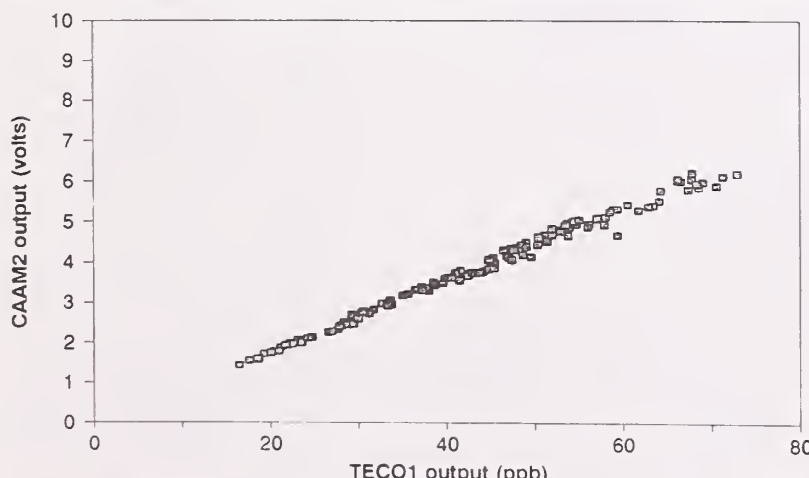


Figure 5—CAAM2 (volt) averages vs. TECO1 (ppb) averages for the week June 27-July 4, 1989.

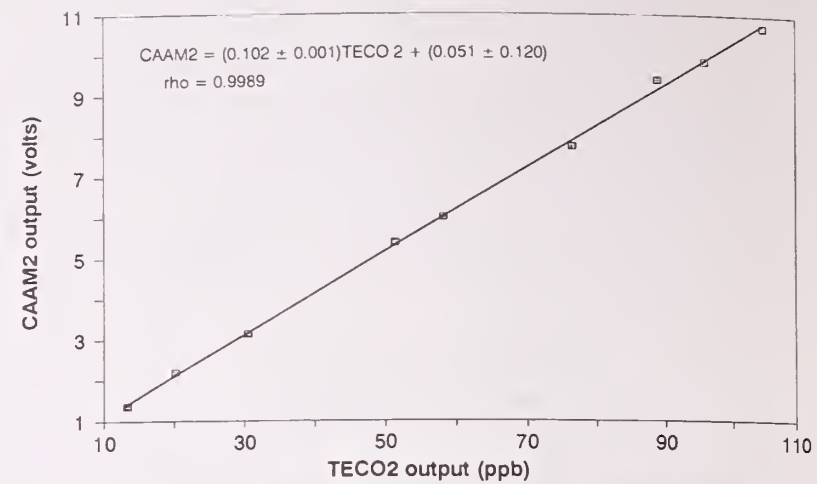


Figure 6—CAAM vs. TECO 9-point calibration—April 5, 1989 (12:30 MST).

bration shown would not necessarily hold over a 1-week period even though the CAAM response would remain linear at all times. When challenged with a constant ozone calibration gas, the CAAM instrument outputs a white-noise signal that varies  $\pm 1.7\%$  of the expected value. For instance, for a 30-ppb ozone calibration gas the CAAM output range would fluctuate between 29.5 and 30.5 ppb.

## TECO Response vs. Ambient Temperature

One of the more interesting results of this study is the similarity in variation with time of the  $\Delta \bar{c}(t)$  and  $\Delta \bar{\theta}(t)$  measurements between 8 and 3 meters. Since  $\Delta \bar{c}(t)$  is measured by subtracting the averages of the two TECO analyzers, one might suspect that the TECOs are responding to temperature as well as to ozone. Although the TECO 49 has an internal adjustment for inlet air temperature (TECO 1986) it is appropriate to verify its response to varying inlet temperatures. Figure 7 is a plot of inlet concentration divided by the TECO output concentration while the TECO is challenged with a continuous stream of 20-ppb ozone calibration gas inlet air during the process of heating the inlet air from 25°C to 51°C over a period of 20 minutes. Additional

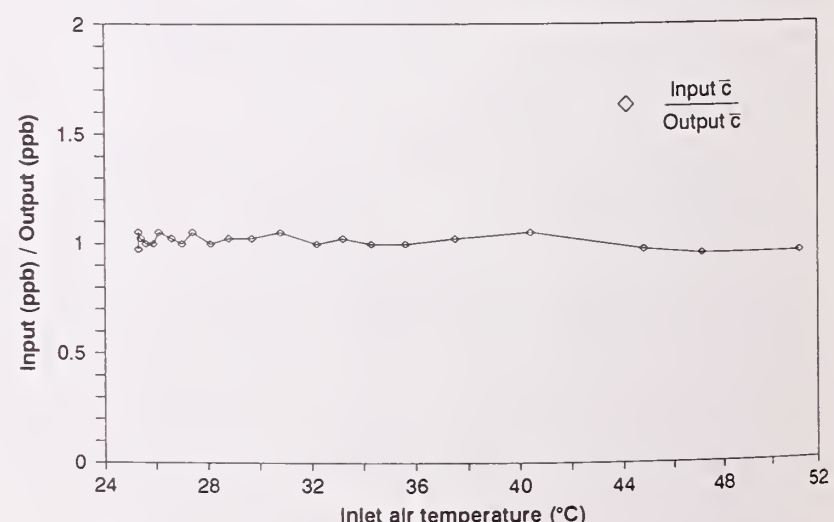


Figure 7—TECO response to varying inlet air temperature over 20-minute period—September 27, 1989.

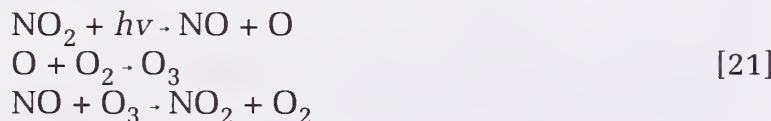
temperature response tests were made by challenging the TECO with 80-ppb inlet air at 22°C continuously for 10 minutes and again at 51°C continuously for 10 minutes with the following results:

Inlet temperature (° C)	Calibration gas input $\bar{c}$ (ppb $O_3$ )	TECO 49 output $\bar{c}$ (ppb $O_3$ )
22.1	80.0	79.8
51.4	79.9	80.8

It was concluded that the TECO 49 analyzer is not sensitive to ambient temperature.

### Ozone Depletion Due to NOx

Ozone is a very reactive gas. The assumption that no ozone is lost to chemical reactions within the layer of air between 3 and 8 m is questionable (Lenschow 1982). Ozone is a member of the  $O_3$ -NO- $NO_2$  triad that takes part in the following-reactions:



The first and third reactions are much slower than the second and are therefore of primary concern (Lenschow and Delany 1987).

Models that calculate ozone flux based on reactions with NOx [21] and without NOx give similar results and compare well with measured data if certain criteria are met (Fitzjarrald and Lenschow 1983). Fitzjarrald and Lenschow (1983) give the criteria

$$\frac{\bar{c}_{NO}}{\bar{c}_{NOx}} \leq 0.1 \quad [22]$$

(where NOx is  $NO + NO_2 +$  other oxides of nitrogen) as a limit to the importance of incorporating [21] into ozone flux calculations below 2 m. In effect, [22] is a criterion for disregarding a net change (production or loss) of ozone due to [21]. Based on the fact that ozone concentrations are typically an order of magnitude greater than NOx concentration, Lenschow and Delany (1987) state that any error in triad  $O_3$ -NO- $NO_2$  flux measurements is least serious for ozone, particularly in a non-urban environment. They claim flux errors should be  $\leq 10\%$ . Concentrations of NO and NOx were measured, albeit not simultaneously, at the Pawnee site during the summer of 1988 (Stocker et al. 1989). The average NO concentration during July 19 through August 2, 1988 was  $0.6 \text{ ppb} \pm 0.4 \text{ ppb}$ . The average NOx concentration during June 21-28, 1988 was  $5 \text{ ppb} \pm 3 \text{ ppb}$ . Stocker et al. (1989) also noted that higher values of NO and  $NO_2$  flux were seen up to 8 hours following rainfall events. Concentrations for both pollutants vary diurnally and

were not measured simultaneously as the same instrument is used to measure both NOx and NO (Zeller 1988; appendix A). Using the above-measured average concentrations for characteristic values of NO and NOx at the Pawnee site provides an order-of-magnitude ratio [22] of:  $0.6/5 = 0.12$  (12%) for NO compared to NOx. Therefore, the chemical reaction of ozone with NO is a possible source of error; however, these measurements were taken above 2 m where it is most likely that an equilibrium in the  $O_3$ -NO- $NO_2$  triad exists (Lenschow and Delany 1987). In addition to NO, aerosols suspended in the atmosphere will also reduce ozone concentrations.

Nonmethane hydrocarbons (NMHC) also play a role in the production of ozone, particularly for NOx concentrations above 1.5 ppb (Liu et al. 1987) which have been measured at the Pawnee site. The emission of NMHC at the Pawnee site is unknown; however, it is expected to be small (Williams 1990) and not a large contributor to ozone production.

For the purpose of this paper, it is assumed that ozone approximates a nonreactive trace gas, although this assumption is actually dependent upon NOx concentrations.

### RESULTS AND DISCUSSION

Based on completeness and continuity of the quantities measured and the operating integrity of the overall data-collection system, the data periods edited and analyzed are May 16-23, 1989 (Julian dates 136-143) and June 6 through July 11, 1989 (Julian dates 157-192). Appendix C shows the crucial data records—fluxes, averages, and gradients of ozone, temperature, and wind speed along with net and total radiation—plotted in their entirety (unedited). The diurnal nature of these measures is evident. The data in appendix C represent approximately 1,900 half-hour sampling periods. After applying the editing criteria presented in appendix A, table A-2, approximately 730 data records were available to provide for the micrometeorological analyses presented below. All the data presented below are edited and all the ozone flux data are corrected for heat flux, as discussed in appendix A. Other flux corrections discussed in appendix A and in Zeller et al. (1989) are tested and discussed below, but they are not included in the determinations of  $\phi_q$ 's nor  $K_q$ 's. Reference to edited, uncorrected data will, therefore, mean that they were corrected for heat flux as just discussed; however, they were not corrected for frequency response or the other response-related flux corrections just alluded to.

Several of the following discussions present data distributions as functions of  $\zeta = z/L$ . The value of  $\zeta$  was calculated from the data using  $L$  from [13], with the values of  $u_*$  and  $w'\theta'$  provided by averaging the mea-

sured values at 3 and 8 meters.<sup>2</sup> Because the flux data from two heights are averaged, an applicable average height must be chosen. In as much as wind distributions in the surface layer are theoretically logarithmic with height during neutral conditions (Businger 1986), the elevation for which calculated  $\zeta$ ,  $\phi_q$  and  $K_q$  values presented herein are applicable is 4.9 meters, the geometric mean measurement height:  $(3 \times 8)^{1/2}$ .

### Gradients of Ozone, Temperature and Horizontal Wind Speed

The approach used to obtain gradients of ozone, temperature, and wind speed is discussed in appendix A. The structures of the simultaneous time-series for ozone- and temperature-gradient measurements are similar and appear to track each other, as shown in the appendix C plots of the ozone and temperature gradients and also in Zeller et al. (1990, fig. 1). Care was taken to ensure that the TECO sensors were monitoring ozone and they were not sensitive to temperature (see appendix A). To demonstrate the variation with time of each measure, figure 8 shows the gradients of ozone and temperature for the period June 13-21, 1989 (Julian dates 164-172). Note that although the two gradients track in general, they do not track exactly. Both ozone and temperature gradients are sensitive to cloud cover which can be inferred by examining the solar-radiation data corresponding to the periods when the extent of the day/night gradient cycles are minimal (e.g., Julian days 164 and 168 compared to days 165, 166, 167, and 169 in fig. 8). The Julian day plotted in all figures represents midnight beginning the new Julian day; for example, the data for June 17, 1989 starts at Julian day 168 and ends at Julian day 169 on figure 8. This convention is followed in all figures and in appendix C.

The ozone-gradient data appear to reach a minimum each morning at 7:30 MST (Mountain Standard Time) and increase slowly with time of day until early evening, 17:30 MST, when they increase rapidly. Figure 9, a diurnal plot of the mean, and variance ozone-gradient data for the entire period, shows this behavior in detail. On average, the ozone-gradient value falls rapidly from a nighttime value of ca.  $0.6 \text{ ppb m}^{-1}$  to  $0.16 \text{ ppb m}^{-1}$  between sunrise (~4:30 MST) and 7:30 MST, then slowly increases to ca.  $0.2 \text{ ppb m}^{-1}$  by 16:00 MST, levels off, and increases rapidly after 17:30 MST as sunset approaches. Ozone concentrations in the surface layer behave in the reverse (fig. 10): the concentration of ozone is lowest at night, increases at sunrise to a maximum at midday, then decreases with sunset. Ozone is known to pool above the surface layer at night when vertical transport is minimal (ozone near the surface is lost to deposition

<sup>2</sup>Both Kaimal (1989) and Wyngaard (1989a) agreed that this averaging approach is reasonable for applying the information available from both levels.

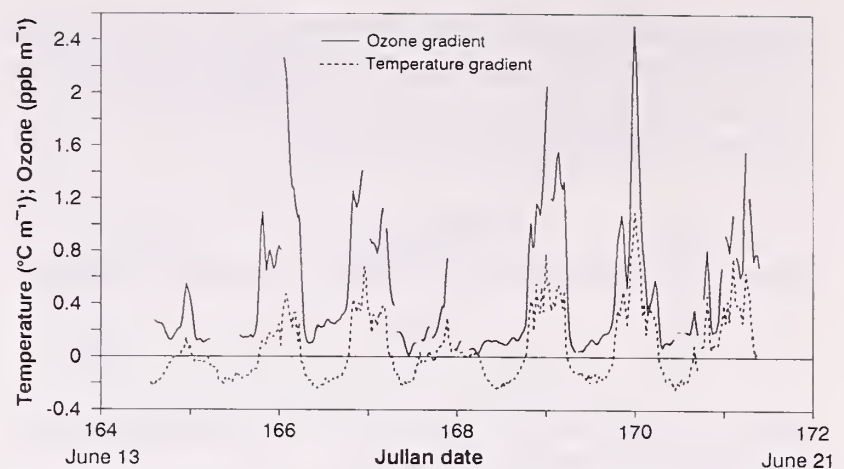


Figure 8—Ozone and temperature gradient data for June 13-21, 1989.

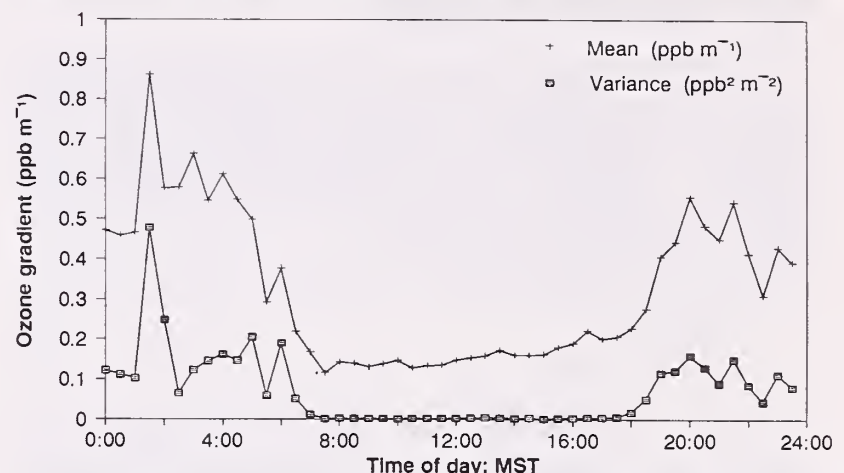


Figure 9—Mean and variance diurnal ozone-gradient data for the entire period: May 16-23 and June 7-11, 1989.

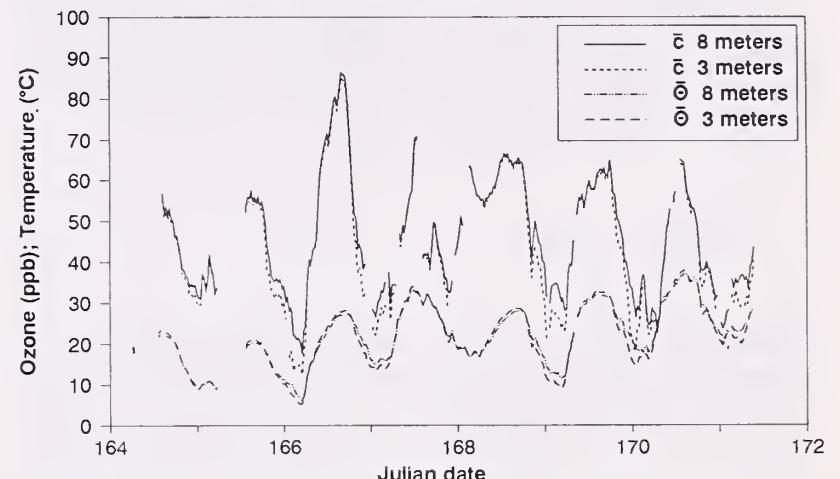


Figure 10—Ozone concentration and temperature at 3 and 8 meters for June 13-20, 1989.

and chemical reactions with surface elements), then mix rapidly downward during daylight with the eradication of the nighttime inversion as a result of surface solar heating (Edinger 1973; Vukovich et al. 1985; Zeller et al. 1977). This phenomenon explains the average values presented in figure 9: initial morning mixing of air from the surface up is rapid and the source of ozone is limited vertically, hence the vertical gradient is rapidly reduced to a minimum. As the inversion base continues to lift, additional ozone from aloft or possibly generated in situ is available for downward transport. The gradient increases until an equilibrium is reached

in the late afternoon between regional ozone production, advection, and surface ozone deposition.

Figure 11 plots ozone gradient data vs. temperature gradient data. Negative temperature gradients are associated with daylight hours and positive temperature gradients with nighttime hours. Note that in general there is no correlation between the two gradients during the day, but at night there is some correlation. The nighttime correlation line plotted is  $\Delta \bar{O}_3 = (1.62 \pm 0.13) \Delta \bar{T} + (0.17 \pm 0.13)$  ( $\pm$  values are standard errors for slope and intercept, respectively) with a correlation coefficient (rho) of 0.65. Strong positive temperature gradients are indicative of limited mixing, which accounts for limited ozone turbulent transport and hence larger ozone gradients.

### Variance of Ozone Temperature, and Vertical Wind Speed

The variances of scalars and vertical velocity appear to obey M-O scaling in the unstable surface layer better than fluxes and gradients (Panofsky and Dutton 1984). With the goal of investigating the similarity of  $K_q$ 's, it is worthwhile to verify the behavior of the Pawnee site data variances for  $w$ ,  $\theta$ , and  $c$  with the empirical relationships provided by other researchers. Equations [23a] and [23b] are two empirical relationships for vertical velocity and scalar quantities, respectively (Panofsky and Dutton 1984):

$$\frac{\sigma_w}{u_*} = 1.25(1 - 3\zeta)^{1/3} \quad \text{for } \zeta < 0 \quad [23a]$$

$$\frac{\sigma_q}{|q_*|} = 5(1 - 16\zeta)^{-1/2} \quad \text{for } \zeta < 0 \quad [23b]$$

where  $\sigma_q = (q'^2)^{1/2}$ , scalar quantities, and  $\sigma_w = (w'^2)^{1/2}$ .

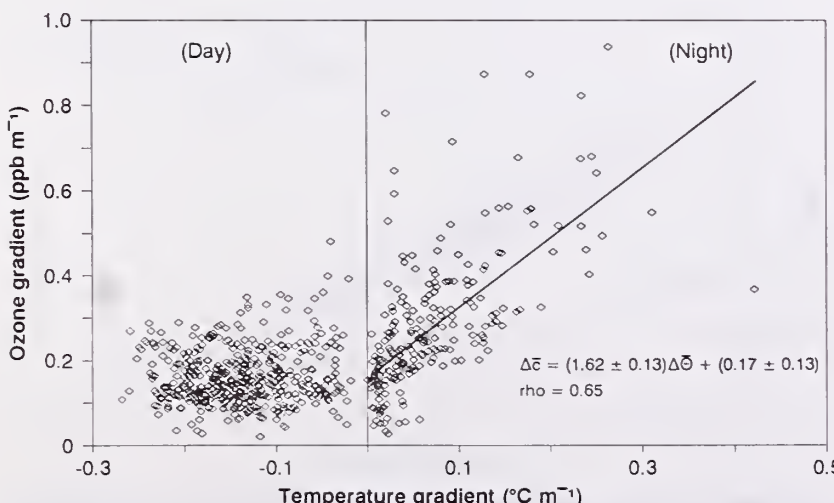


Figure 11—Ozone gradient vs. temperature gradient for the entire data collection period.

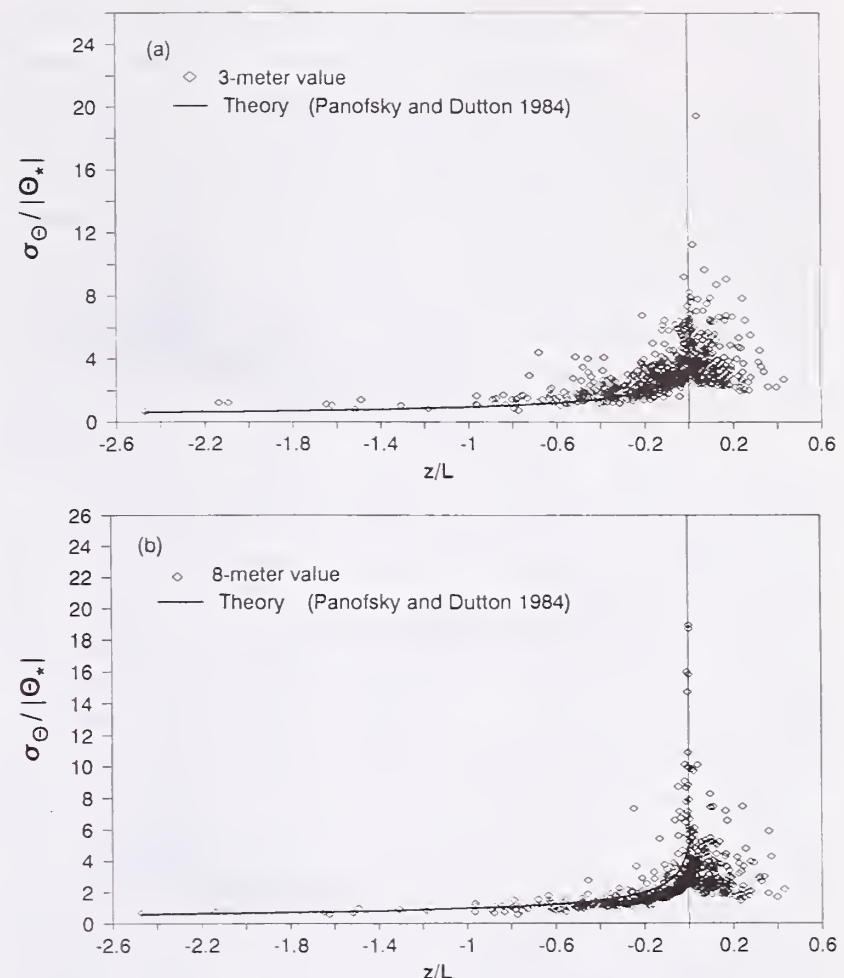


Figure 12—Nondimensional ozone variance  $\sigma_c / |c_*|$  vs. stability parameter ( $z/L$ ) for (a) 3-meter and (b) 8-meter data—May 16-July 11, 1989.

The constants in these equations are not particularly well established and vary from investigator to investigator. The  $1/3$  and  $-1/2$  powers, however, do describe typical slopes of measured variances versus  $\zeta$  for  $\zeta < -0.5$ , the local free-convection regime (Wyngaard 1989b). Figure 12 shows  $\sigma_c / |c_*|$  for ozone variance for 3 and 8 meters as measured by the CAAM ozone sensors; the theoretical plots of [23b] are adjusted for  $z = 3$  and  $z = 8$  meters, respectively. The data scatter, less at 8 meters than at 3 meters, is typical of that experienced by others (Panofsky and Dutton 1984); also, the trend with unstable  $\zeta$  follows the  $-1/2$  slope (solid line) closely.

Figure 13 shows  $\sigma_\theta / |\theta_*|$  for temperature. Again the data scatter at 3 meters is greater than that at 8 meters and the data slope,  $-1/2$ , follows the theory closely (Panofsky and Dutton 1984). The relative vertical location of the theoretical line is a function of the constants used in [23b]. This investigation does not attempt to establish constants specific to the Pawnee site for [23a] and [23b].

Figure 14 shows  $\sigma_w / u_*$  for momentum. For this quantity the measured data scatter at 8 meters is greater than at 3 meters. Vertical turbulence is a function of  $z$ ; hence the spectrum of eddies contributing to  $\sigma_w$  at 8 meters is broader than the spectrum of eddies contributing to  $\sigma_w$  at 3 meters. The data follow the  $1/3$  slope of the theoretical curves, [23a], as plotted.

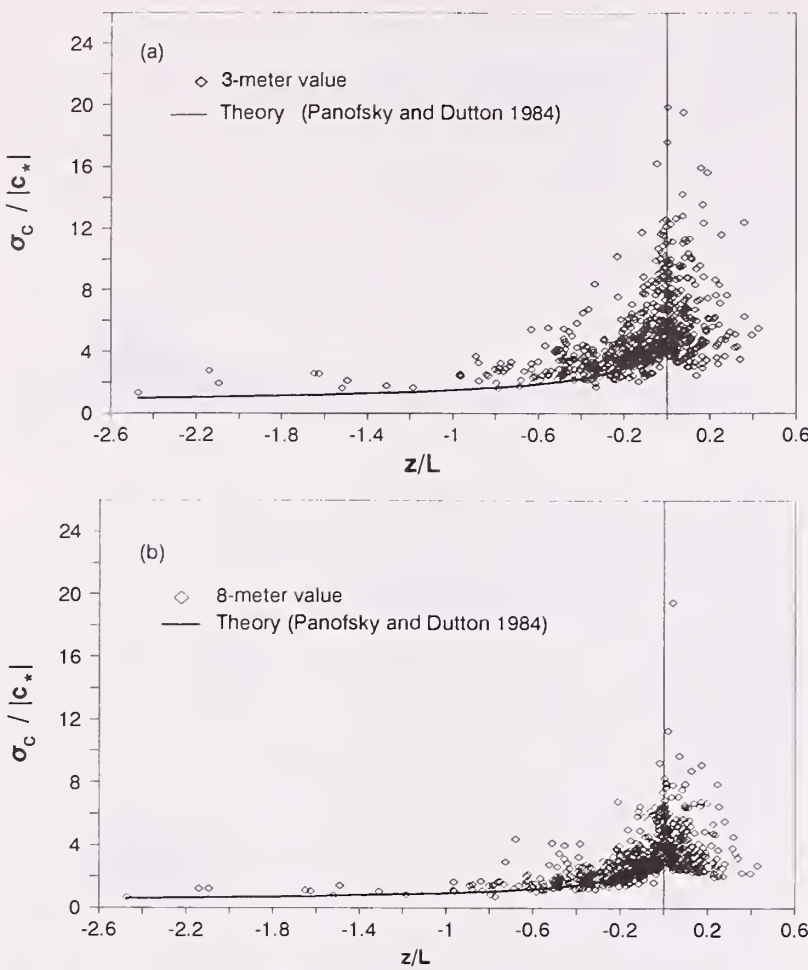


Figure 13—Nondimensional temperature variance  $\sigma_c / |\theta_1|$  vs. stability parameter ( $z/L$ ) for (a) 3-meter and (b) 8-meter data—May 16–July 11, 1989.

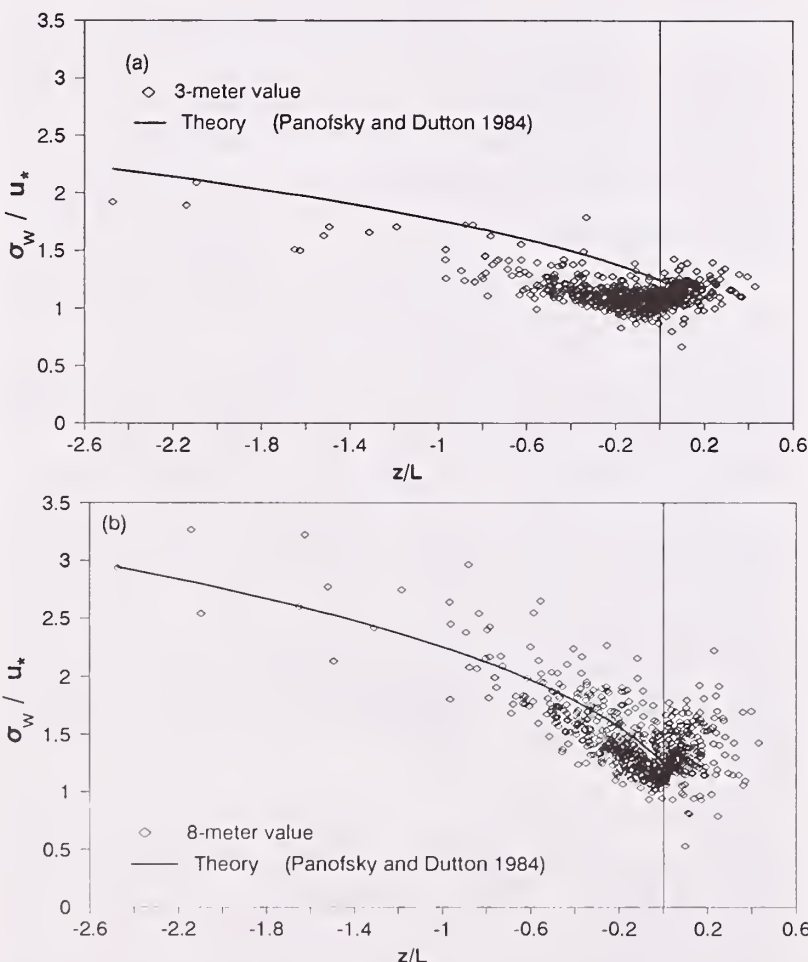


Figure 14—Nondimensional vertical-velocity variance  $\sigma_w / u_*$  vs. stability parameter ( $z/L$ ) for (a) 3-meter and (b) 8-meter data—May 16–July 11, 1989.

Figures 12–14 demonstrate that individual eddy measurements for ozone, temperature and momentum at 3 and 8 meters are reasonable and follow M-O scaling within the bounds typically experienced by micrometeorological researchers.

## Surface Roughness

The determination of velocity, temperature, and mass profiles in the surface layer requires a knowledge of the surface roughness,  $z_0$ , and the zero-plane displacement. For the Pawnee site, the zero-plane displacement is essentially zero due to the shortgrass prairie canopy environment (individual grass element heights ca. 25 cm); hence [17a–c] do not include it. It is appropriate to limit the determination of  $z_0$  to near-neutral-stability data where  $|\zeta| < 0.03$  (eg., Fazu and Schwerdtfeger 1989). Figure 15 shows the results of 133  $z_0$  calculations meeting this condition plotted against their corresponding wind speeds at 8 meters. The value  $z_0$  was calculated by combining [17a] with [18a] and [18b]. In this way  $z_0$  is based on measured  $u_*$  not  $\Delta \bar{u}$ . The average  $z_0$  for the Pawnee site, for the data period analyzed, is 1.60 cm with standard deviation of 0.89 cm. This value falls within the expected value for “fairly level grass plains” (Arya 1988).

## Fluxes of Ozone, Sensible Heat, and Momentum

The unedited and uncorrected fluxes of ozone,  $\overline{w'c'}$  (ppb  $m s^{-1}$ ) sensible heat,  $\overline{w'\theta'}$  ( $^{\circ}C m s^{-1}$ ) and momentum,  $\overline{u'w'}$  ( $m^2 s^{-2}$ ) are presented in appendix C. This section presents edited-corrected and edited-uncorrected fluxes measured at 3 and 8 meters.

The concept of a constant-flux layer is often confused with the idea that the flux of a given quantity at

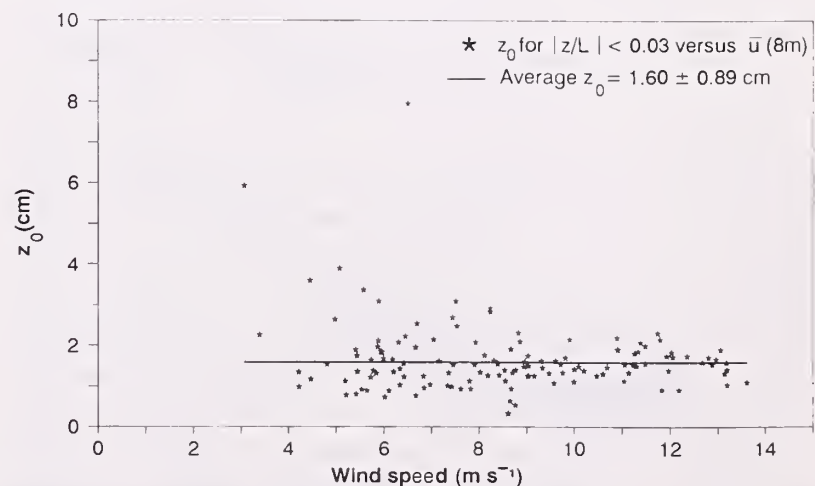


Figure 15—Surface roughness  $z_0$  vs. 8-meter wind speed for  $|\zeta| < 0.03$ . Average  $z_0 = 1.60$  cm standard deviation = 0.89 cm.—May 16–July 11, 1989.

two separate elevations must be the same (Wyngaard 1989a). Rather it is the flux divergence,  $\partial \overline{w'q'} / \partial z$ , that should be constant with height in the surface and convective boundary layers (Wyngaard 1989b). This implies, for instance, that the flux,  $w'q'$ , would be a maximum for heat and momentum at the earth's surface or source of these fluxes, and decrease linearly to approximately zero at the top of the boundary layer. On the other hand, the source of ozone is above the surface layer (at least initially in the morning) in non-ozone-producing rural locations like the Pawnee site. For ozone the flux,  $w'c'$ , would be a maximum at some elevated location experiencing maximum ozone concentrations (i.e., its source for vertical transport), and decrease linearly to the surface where it doesn't quite become zero but is continually deposited at the surface. One would, therefore, expect measured  $\overline{u'w'}$  and  $\overline{w'\theta'}$  to be greater at 3 meters compared to 8 (Wyngaard 1989b), and measured  $w'c'$  for ozone to be greater at 8 meters compared to 3 based on the above argument.

Haugen et al. (1971) have used the criterion  $\pm 20\%$  to declare a given flux constant within the surface layer. In practice, daytime boundary layers exceed 1 km; therefore, the distance between 8 and 3 meters relative to the top of the boundary layer would not be enough to detect flux differences given the limits of measurement

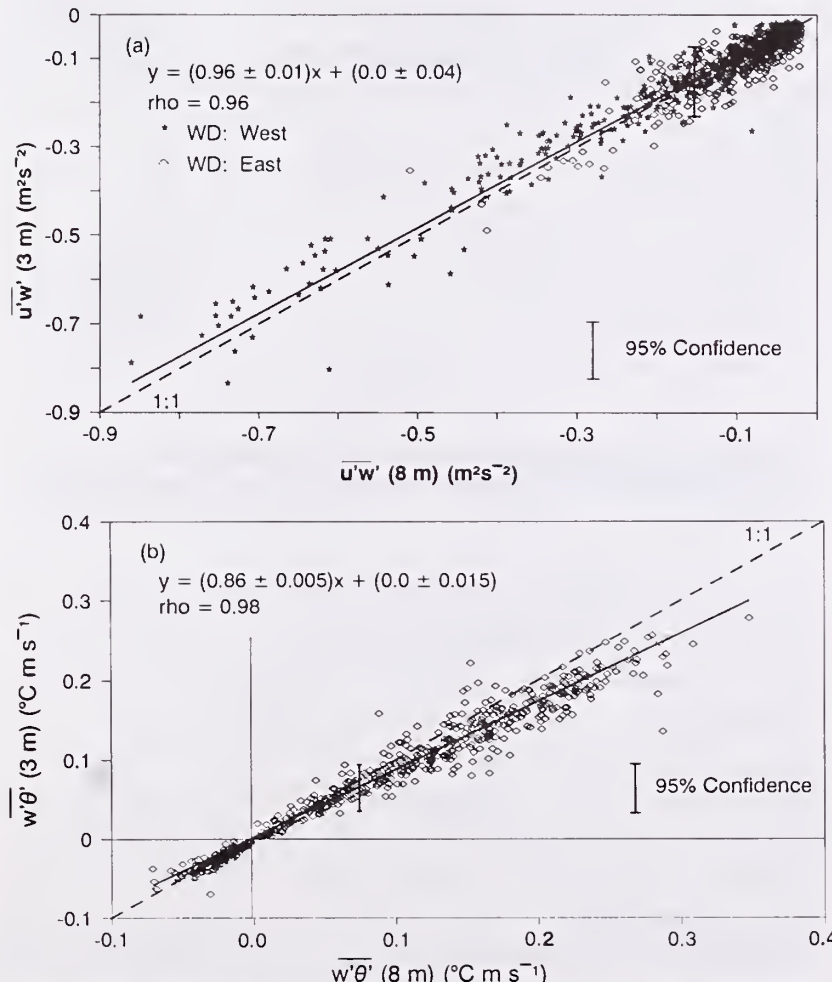


Figure 16—Comparisons of the uncorrected fluxes of (a) momentum (Reynolds stress) and (b) sensible heat, as measured at 8 and 3 meters—May 16–July 11, 1989.

accuracy and all flux measurements between 3 and 8 meters ought to be equal statistically.

Figure 16 compares the uncorrected fluxes of (a) momentum (Reynolds stress) and (b) sensible heat as measured at 8 and 3 meters. Although in both figures the measured fluxes at 3 meters are less than the measured fluxes at 8 meters contrary to the above argument, the statistical differences are not significant as the 95% confidence intervals fall within the range where they are equal. For a subset of this uncorrected momentum-flux data, the 3-meter flux tended to be slightly greater (see discussion below in this section).

The differences between the 8- and 3-meter uncorrected fluxes of ozone, as shown in figure 17 do not behave the same as heat and momentum. The range for constant ozone flux at both heights falls at the edge, practically outside, of the 95% confidence interval, which is statistically significant. That is, there is 95% statistical confidence that the 1:1 ratio line falls outside the measured data. Based on the constant flux divergence argument, the flux of ozone in particular should be a little greater at 8 compared to 3 meters but it shouldn't be as discernible in the measurements made. It is possible that ozone is depleted chemically at 3 meters faster than at 8 meters because of surface ozone sinks: surface canopy, soil, and nitrogen species. However, as presented previously, ozone should be in chemical equilibrium above 2 meters (Lenschow and Delany 1987).

One possibility, emissions of NO (see [21]) at the Pawnee site, is somewhat dependent on soil moisture. The greater the soil moisture experienced following rain events, the more NO emitted from the surface. Emissions of NO are neither constant with time nor diurnal in variability (Stocker et al. 1989); therefore, figure 17 should show even more scatter, particularly about the 1:1 ratio if NO emissions were responsible, because the data represent both moist and dry periods. Another possibility, based on the analysis to follow, is that the known errors in flux measurements as discussed in appendix A and Zeller et al. (1989) may

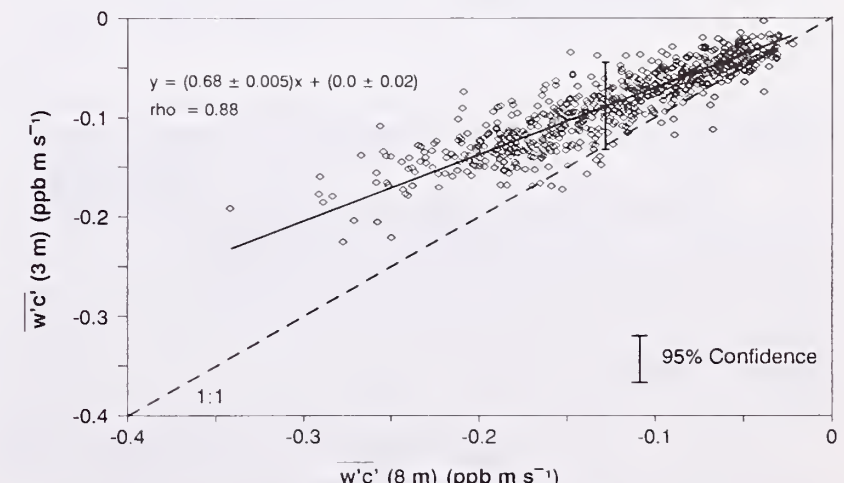


Figure 17—Ozone flux at 3 meters vs. ozone flux at 8 meters—May 16–July 11, 1989.

account for the measured difference in ozone flux between the two heights.

Figure 18 compares the corrected ozone flux at the two measurement heights for two weeks of data: May 16-23 and June 6-13, 1989, subsets of the total data base analyzed. (Corrections were limited to this 2-week test period because the corrections are considerably complicated to make, they are based on theoretical cospectra, and they add uncertainty to the data.) The figure demonstrates that the flux corrections may account for the difference in measured ozone flux. The 95% confidence interval, although considerably larger, now includes the range (1:1 ratio line) where the fluxes would be equal statistically. The corrected fluxes have been plotted indicating stability because corrections for stable ozone fluxes tend to be very large; greater than 10 times the original data in some cases (Zeller et al. 1989). In general, the corrected data (fig. 18) are broadly scattered compared to the uncorrected data (fig. 17). On average, the corrected flux at 8 meters is 1.45 times greater than the original uncorrected flux data, and 1.84 times greater than the original uncorrected data for 3 meters.

Figure 19 shows the uncorrected residuals for uncorrected ozone flux  $[(w'c' (8 \text{ m}) - w'c' (3 \text{ m}))]$  of figure 17 plotted against time of day. The data are too scattered to imply much except that the differences tend

to be slightly greater during midday when the maximum ozone flux is occurring. This tends to support the need for flux corrections, particularly with slower response sensors sited at elevations where frequency response of the sensors are inadequate. The larger correction values for stable cases are worrisome however.

Flux corrections were also made on the momentum flux and sensible heat flux data for the same data subset: May 16-23 and June 6-13, 1989 (fig. 20). For momentum flux (a) the corrections are not as severe as those for ozone flux. Note that the uncorrected and corrected momentum flux experienced slightly greater values at 3 meters than at 8 meters for this data subset. The 95% confidence interval shown in figure 20a is only 20% larger for the corrected momentum flux compared to uncorrected flux, considerably less than the 300% increase in the 95% confidence interval experienced for ozone flux corrections. On the average, corrected momentum flux for both heights were the same: 1.34 times the original flux. Sensible heat-flux corrections (fig. 20b) behave similarly to those for momentum flux: data scatter as reflected in the data and in the 95% confidence interval is ca. 20% greater; corrections for 8 meters are 1.21 times the uncorrected flux for stable and unstable situations; corrections for 3 meters are 1.21 times the positive (unstable) flux and 1.32 times the

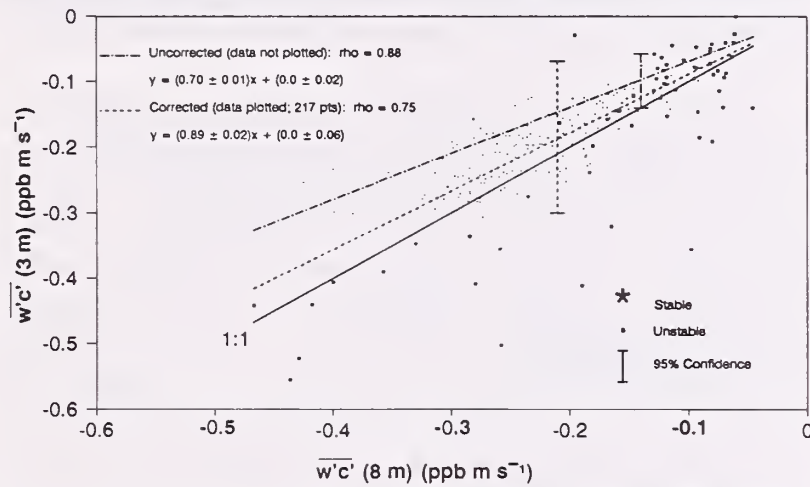


Figure 18—Corrected ozone flux at 3 meters vs. corrected ozone flux at 8 meters—May 16-23 and June 6-13, 1989.

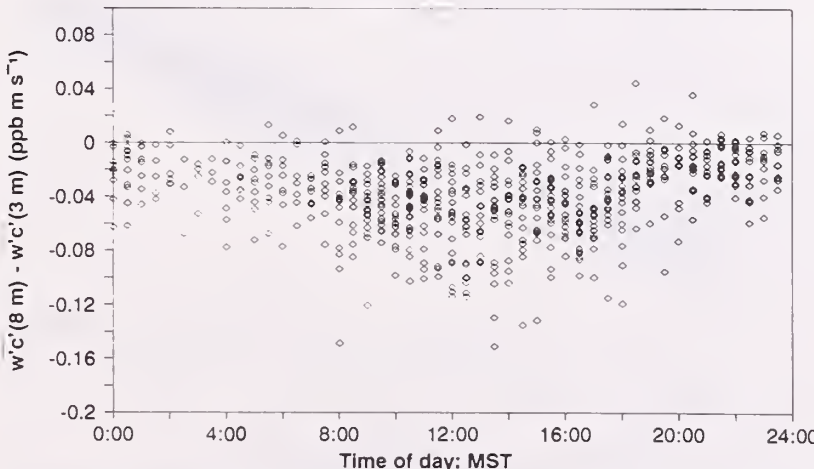


Figure 19—Ozone flux residuals:  $[(8\text{-meter flux}) - (3\text{-meter flux})]$  vs. time of day—May 16-July 11, 1989.

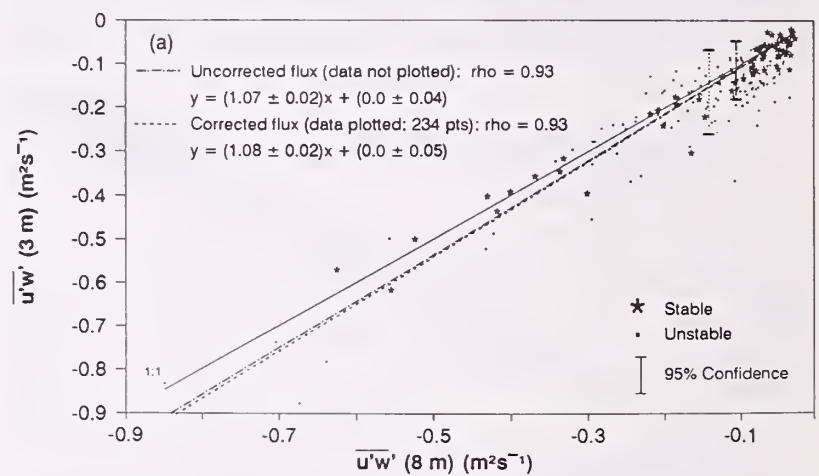


Figure 20a—Corrected momentum flux at 3 meters vs. corrected momentum flux at 8 meters—May 16-23 and June 6-13, 1989.

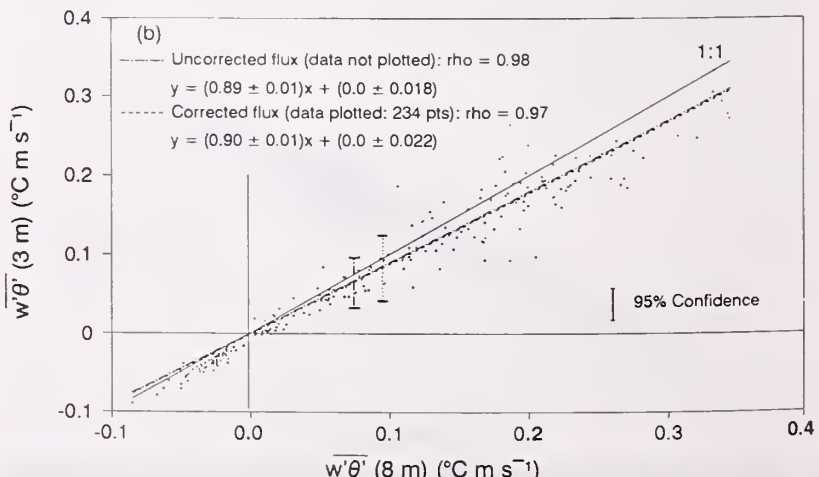


Figure 20b—Corrected sensible heat flux at 3 meters vs. corrected sensible heat at 8 meters—May 16-23 and June 6-13, 1989.

negative (stable) flux. Momentum-flux corrections are slightly greater because of the added correction for horizontal wind shadowing, while both sensible-heat and momentum-flux corrections are less than ozone because their sensor frequency responses are considerably faster than those of the ozone CAAM sensors.

### Dimensionless Gradients of Ozone, Sensible Heat, and Momentum

As discussed, the dimensionless gradients of momentum, sensible heat, and mass, [15a-c], are expected to be universal functions of  $\zeta$  according to M-O similarity. Figure 21 shows the values of  $\phi_m$ ,  $\phi_h$ , and  $\phi_c$  using the edited, uncorrected (see first paragraph under “Results and Discussion”) Pawnee site data plotted linearly as functions on  $\zeta$ . The results are valid for  $z = 4.9$  m as the measured data from both 3 and 8 m are used to calculate the  $\phi$  values. The empirical lines annotated in figure 21 are [16a-b] where [166] is used for  $\phi_c$  in figure 21c (i.e.,  $\phi_c = \phi_h$ ). These are the expressions for  $\phi$  established by Businger (1971). The other lines are regression models of the data using  $\zeta$  as the independent variable (discussed below). Table 3 presents the linear regression results obtained by comparing the measured values of  $\phi$ :  $\phi_{mm}$ ,  $\phi_{hm}$ , and  $\phi_{cm}$ , with the empirical or theoretical values  $\phi_{mT}$ ,  $\phi_{hT}$ , and  $\phi_{cT}$  (the second subscript is added to distinguish between measured, m, and theoretical, T). These regression results are included to show the statistical differences between the Pawnee-site measurement and those established for smooth terrain. The regression results were separated by wind direction because of the wind-direction dependence on  $\phi_{mm}$  shown in figure 21a. Measured values,  $\phi_{mm}$ , are considerably lower for wind directions with azimuth 250° clockwise through azimuth 030°. This dramatic wind direction related distribution in the values of  $\phi_{mm}$  is surprising as the  $z_0$  analysis based on measured  $u_*$  (fig. 15) did not reveal a dependence on wind direction. This is also true when  $z_0$  is calculated for all stabilities. There are two possible causes for the dependence of wind direction on  $\phi_m$ : climatological—westerly through northerly wind speeds tend to be greater at the Pawnee site; and/or terrain induced—as described previously, there is a drainage swale ca. 400 m west of the site. Measured momentum flux tends to be greater for faster wind speeds regardless of the wind direction, while measured wind shear,  $\partial \bar{u} / \partial z$ , at the Pawnee site tends to be smaller by a factor of two for westerly through northerly winds. None of the other measured flux nor gradient data, ( $w' \theta'$ ,  $w' c'$ ,  $\partial \bar{\theta} / \partial z$ , and  $\partial \bar{c} / \partial z$ ) show dependence on wind direction. The fact that  $\partial \bar{u} / \partial z$  shows a dependence on wind direction and that larger  $u' w'$  values are simply related to faster wind speeds explains why the terrain effect shows up for  $\phi_m$ ,

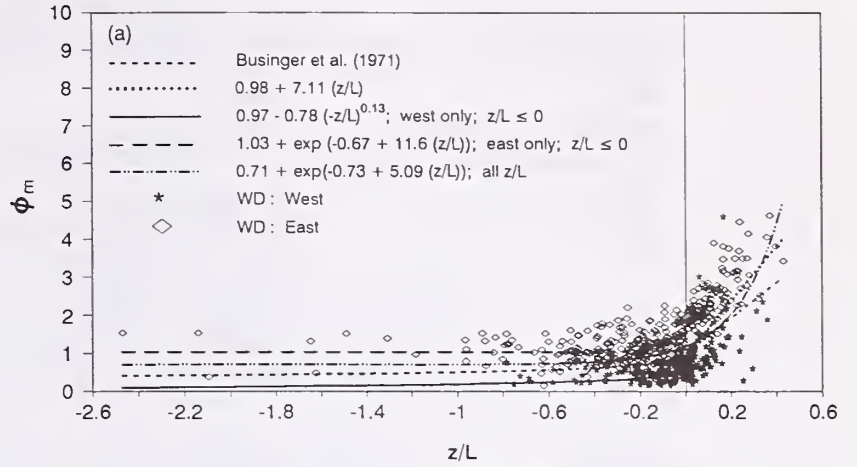


Figure 21a—Dimensionless wind shear (momentum) ( $\phi_m$ ) data results—theoretical dimensionless wind shear; and best regression model wind shear for east- and west-wind categories vs. stability parameter ( $z/L$ ).

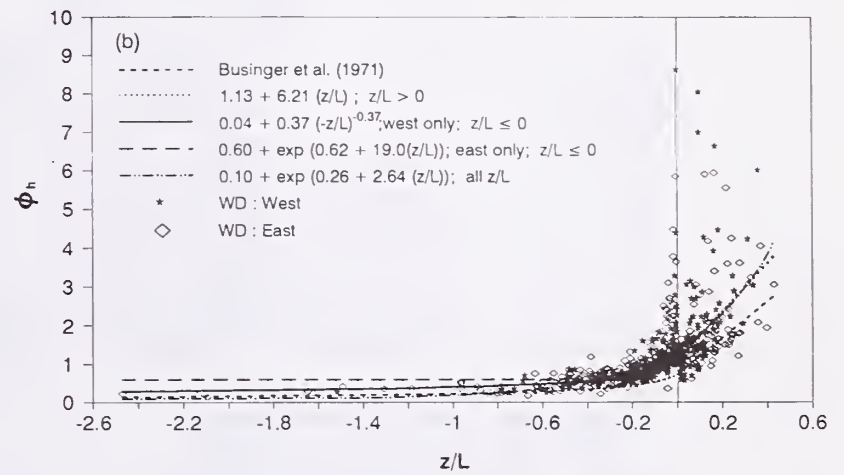


Figure 21b—Dimensionless sensible-heat gradient ( $\phi_h$ ) data results; theoretical sensible-heat gradient; and regression-model sensible-heat gradients vs. stability parameter ( $z/L$ ).

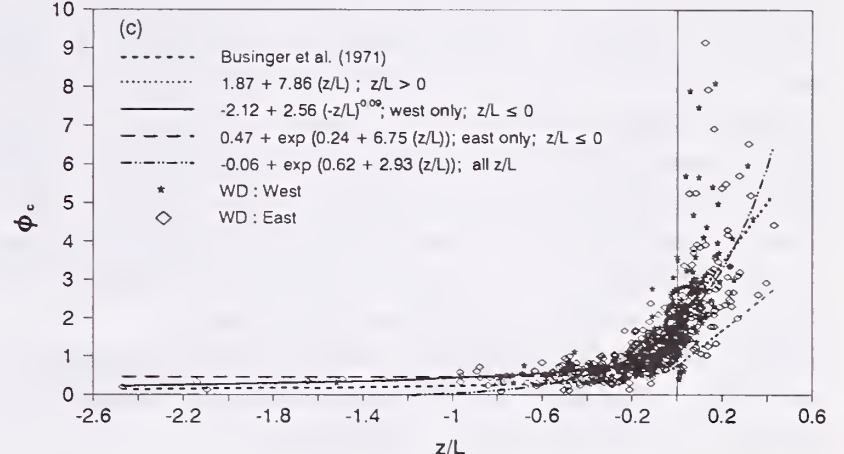


Figure 21c—Dimensionless ozone gradient ( $\phi_c$ ) data results; theoretical sensible-heat gradient; and regression-model ozone gradients vs. stability parameter ( $z/L$ ).

[15], and not for  $z_0$ , [17]. The data results specific to momentum will hereafter be segregated by wind direction where azimuth 250° clockwise through 030° will be referred to as “west” and representative of “irregular or rough terrain,” and wind direction azimuth 030° clockwise through 250° will be referred to as “east” and representative of “smooth terrain.”

The best correlations with smooth terrain (table 3) for  $\phi$  values are for unstable  $\phi_c$ , unstable  $\phi_h$  and stable  $\phi_m$ . The data distribution for values shown in figure 21

Table 3. — Linear regression  $\phi_{qm}$  (measured) vs.  $\phi_{qT}$  (theory).

Parameter	Stability <sup>+</sup>	Wind* dir.		$\phi_{qT}$			No data points	Corr. coeff. (rho)
			slope	$\pm SE$	offset	$\pm SE$		
$\phi_{cm}$ vs $\phi_{cT}$	§ u	West	3.52	$\pm 0.27$	-0.79	0.42	160	0.72
	u	East	2.50	0.07	-0.24	0.33	293	0.69
	u	All	2.81	0.13	-0.38	0.37	453	0.71
	u	All	2.06	0.04	0.00	0.38	453	0.68
	s	West	2.40	0.36	-0.05	1.23	104	0.55
	s	East	1.35	0.26	0.95	1.20	127	0.42
	s	All	1.66	0.21	0.63	1.23	231	0.47
	s	All	2.16	0.07	0.00	1.24	231	0.45
$\phi_{hm}$ vs $\phi_{hT}$	u	West	3.35	0.41	-0.80	0.66	173	0.53
	u	East	3.73	0.20	-0.76	0.45	318	0.72
	u	All	3.32	0.19	-0.65	0.54	491	0.63
	u	All	2.04	0.05	0.00	0.57	491	0.58
	s	West	1.98	0.30	-0.39	1.11	100	0.56
	s	East	1.08	0.20	0.30	0.87	114	0.46
	s	All	1.32	0.17	0.15	1.02	214	0.47
	s	All	1.43	0.05	0.00	1.02	214	0.47
$\phi_{mm}$ vs $\phi_{mT}$	u	West	0.77	0.13	-0.20	0.19	159	0.43
	u	West	0.52	0.02	0.00	0.19	159	0.41
	u	East	0.91	0.17	0.49	0.36	319	0.29
	u	East	1.58	0.03	0.00	0.37	319	0.19
	s	West	0.95	0.13	-0.44	0.51	120	0.56
	s	West	0.64	0.03	0.00	0.52	120	0.53
	s	East	1.13	0.10	0.67	0.48	131	0.71
	s	East	1.53	0.03	0.00	0.51	131	0.66

+ u: unstable; s: stable

\* east:  $030^\circ$  -  $250^\circ$  azimuth (clockwise)west:  $250^\circ$ - $030^\circ$  azimuth (clockwise)

all: all wind directions combined.

 $\S \phi_{cT} = \phi_{hT}$ 

SE: Standard Error

is typical in the literature (e.g., Korrell et al. 1992; Fazu and Schwerdtfeger 1989) where reported unstable values for  $\phi_m$  and  $\phi_h$  are widely scattered with values ranging between 0.0 and 1.5. Standard errors for  $\phi_{qm}$  comparisons with  $\phi_{qT}$  theory as given in table 3 are not typically presented in the literature; however, the relatively large values for y-standard errors associated with the Pawnee site results appear to be normal judging by the similar ranges in published data scatter.

Four regression models with  $\zeta$ , the independent variable, were fitted to the measured  $\phi$  data to provide a means to evaluate eddy diffusivities:

$$\phi_{qm} = b_1 + b_2 \zeta \quad \zeta > 0 \quad [24a]$$

$$\phi_{qm} = b_1 + b_2 (-\zeta)^{-b_3} \quad \zeta \leq 0 \quad [24b]$$

$$\phi_{qm} = b_1 + \exp(b_2 + b_3 \zeta) \quad \zeta \leq 0 \quad [24c]$$

$$\phi_{qm} = b_1 + \exp(b_2 + b_3 \zeta) \quad \text{all } \zeta \quad [24d]$$

Here  $b_i$  are the separate parameter constants for each model and for each comparison (i.e.,  $b_1$  [24a]  $\neq$   $b_1$  [24b]). Table 4 presents the regression results including the standard errors on each parameter and the correlation coefficient for each model result. Regressions were made for separated east- and west-wind categories in addition to an "all" wind-direction category. The corre-

lation coefficients are similar in value to those in table 3 for the linear regressions with existing empirical values as the independent variable, which is expected as they are also functions of  $\zeta$ . Selected regression models that best fit the data are plotted on figure 21. Regression [24b] fits both measured and  $\phi_c$  and  $\phi_h$  better for  $\zeta < -1$  (figs. 21b and c), while [24c] appears to fit better for  $-1 < \zeta < 0$ . For  $\phi_m$  (fig. 21a), [24b] is plotted for the west data while [24c] was chosen for the east data.

Measured values of  $\phi$  for non-ideal terrain can be compared with established values of  $\phi$  for smooth terrain using  $\gamma$  to illustrate deviations in the measured results. This approach was previously established to investigate the roughness sublayer (Garratt 1978) but also serves as a useful comparative tool here.

$$\gamma_q = \frac{\phi_{qT}}{\phi_{qm}} \quad \begin{array}{l} \text{(smooth)} \\ \text{(measured)} \end{array} \quad [25]$$

Figure 22 plots the results for  $\gamma_m$ ,  $\gamma_h$ , and  $\gamma_c$  vs.  $-\zeta$  [25] on a log scale using [16a-b] for  $\phi_{qT}$ . The surface layer  $\gamma_h$  and  $\gamma_m$  results obtained by Garratt (1978) for tall vegetation ( $z_o = 40$  cm) and by Fazu and Schwerdtfeger (1989) for bushland ( $z_o = 43$  cm) are also plotted on the figure for comparison even though the canopy, terrain, and pro-

Table 4. — Regression model results

Model Equation	Wind dir.	Parameters $\pm$ SE			Corr. coeff. (rho)
		$b_1$	$b_2$	$b_3$	
$\phi_{cm} = b_1 + b_2 \zeta$	All	1.87 $\pm$ 0.12	7.86 $\pm$ 0.97	—	0.47
	East	1.96 $\pm$ 0.18	6.41 $\pm$ 1.23	—	0.42
	West	1.72 $\pm$ 0.17	11.40 $\pm$ 1.71	—	0.55
$\phi_{cm} = b_1 + b_2 (-\zeta)^{-b_3}$	All	-2.12 $\pm$ 1.89	2.56 $\pm$ 1.86	0.09 $\pm$ 0.05	0.69
	East	-1.50 $\pm$ 1.70	1.95 $\pm$ 1.86	0.11 $\pm$ 0.08	0.68
	West	-2.83 $\pm$ 5.11	3.23 $\pm$ 5.01	0.08 $\pm$ 0.10	0.66
$\phi_{cm} = b_1 + \exp(b_2 + b_3 \zeta)$	All	0.47 $\pm$ 0.05	0.24 $\pm$ 0.05	6.75 $\pm$ 0.80	0.71
	East	0.39 $\pm$ 0.06	0.14 $\pm$ 0.06	4.37 $\pm$ 0.72	0.69
	West	0.46 $\pm$ 0.10	0.39 $\pm$ 0.07	9.49 $\pm$ 1.87	0.73
$\phi_{cm} = b_1 + \exp(b_2 + b_3 \zeta)$	All	-0.06 $\pm$ 0.13	0.62 $\pm$ 0.08	2.93 $\pm$ 0.23	0.74
$\phi_{hm} = b_1 + b_2 \zeta$	All	1.13 $\pm$ 0.11	6.21 $\pm$ 0.79	—	0.47
	East	1.11 $\pm$ 0.15	5.10 $\pm$ 0.92	—	0.46
	West	1.07 $\pm$ 0.16	9.30 $\pm$ 1.40	—	0.56
$\phi_{hm} = b_1 + b_2 (-\zeta)^{-b_3}$	All	0.04 $\pm$ 0.13	0.37 $\pm$ 0.09	0.37 $\pm$ 0.04	0.74
	East	-0.45 $\pm$ 0.27	0.76 $\pm$ 0.23	0.30 $\pm$ 0.05	0.79
	West	0.51 $\pm$ 0.11	0.07 $\pm$ 0.03	0.62 $\pm$ 0.08	0.76
$\phi_{hm} = b_1 + \exp(b_2 + b_3 \zeta)$	All	0.06 $\pm$ 0.03	0.62 $\pm$ 0.06	19.0 $\pm$ 2.22	0.67
	East	0.55 $\pm$ 0.04	0.78 $\pm$ 0.06	14.2 $\pm$ 1.45	0.77
	West	0.81 $\pm$ 0.05	1.38 $\pm$ 0.10	132.0 $\pm$ 19.5	0.72
$\phi_{hm} = b_1 + \exp(b_2 + b_3 \zeta)$	All	0.10 $\pm$ 0.13	0.26 $\pm$ 0.11	2.64 $\pm$ 0.30	0.62
$\phi_{mm} = b_1 + b_2 \zeta$	All	0.89 $\pm$ 0.08	7.11 $\pm$ 0.59	—	0.82
	East	1.79 $\pm$ 0.07	5.29 $\pm$ 0.47	—	0.71
	West	0.51 $\pm$ 0.06	4.46 $\pm$ 0.61	—	0.56
$\phi_{mm} = b_1 + b_2 (-\zeta)^{-b_3}$	All	0.96 $\pm$ 0.59	-0.05 $\pm$ 0.54	0.18 $\pm$ 1.33	0.04
	East	2.31 $\pm$ 3.00	-1.36 $\pm$ 2.97	-0.09 $\pm$ 0.23	0.30
	West	0.97 $\pm$ 0.83	-0.78 $\pm$ 0.78	-0.13 $\pm$ 0.20	0.43
$\phi_{mm} = b_1 + \exp(b_2 + b_3 \zeta)$	All	0.70 $\pm$ 0.58	-1.82 $\pm$ 3.42	-0.54 $\pm$ 1.18	0.08
	East	1.03 $\pm$ 0.03	-0.67 $\pm$ 0.18	11.60 $\pm$ 4.07	0.33
	West	0.31 $\pm$ 0.03	-1.11 $\pm$ 0.16	17.50 $\pm$ 6.79	0.47
$\phi_{mm} = b_1 + \exp(b_2 + b_3 \zeta)$	All	0.71 $\pm$ 0.05	-0.73 $\pm$ 0.14	5.09 $\pm$ 0.41	0.33

file conditions at the Pawnee site are different. Figure 22a for  $\gamma_m$  illustrates the dramatic effect of the westerly winds on the Pawnee site  $\phi_m$  measurements; figures 22b and c do not show this effect. With the exception of west  $\gamma_m$  values, the  $\gamma$  values are generally less than 1 for  $\zeta < 0$ , indicating that in general  $\phi_{qm} > \phi_{qT}$  for momentum (east direction), heat, and ozone. The  $\gamma$  results for  $\zeta > 0$  (fig. 23) are similar in distribution to unstable  $\gamma_c$  and east  $\gamma_m$  values. Stable west  $\gamma_m$  values (fig. 23a) are also similar to unstable west  $\gamma_m$  values. The stable  $\gamma_h$  results are closer to the ratio 1 but they are widely distributed.

If the geometric mean height, 4.9 m, selected as the representative height applicable for combining data from 3 and 8 meters were replaced with a slightly lower value, say 4 m, the  $\gamma$  values in figures 22 and 23 would increase and be closer to the ratio 1. The choice of z does

not, however, affect the eddy-diffusivity ratio results presented next.

#### Eddy Diffusivities of Ozone, Sensible Heat, and Momentum

Theoretically, eddy diffusivities are directly related to atmospheric stability and wind gradients and can be estimated knowing  $u^*$  without flux information. This is seen by combining [15a] with either [8a], [8b], or [8c]:  $K_q$  can be calculated for any z, at any stability  $\zeta$ , knowing  $u^*$  and  $\phi_q$ :

$$K_q = \frac{k u^* z}{\phi_q(\zeta)} \quad [26]$$

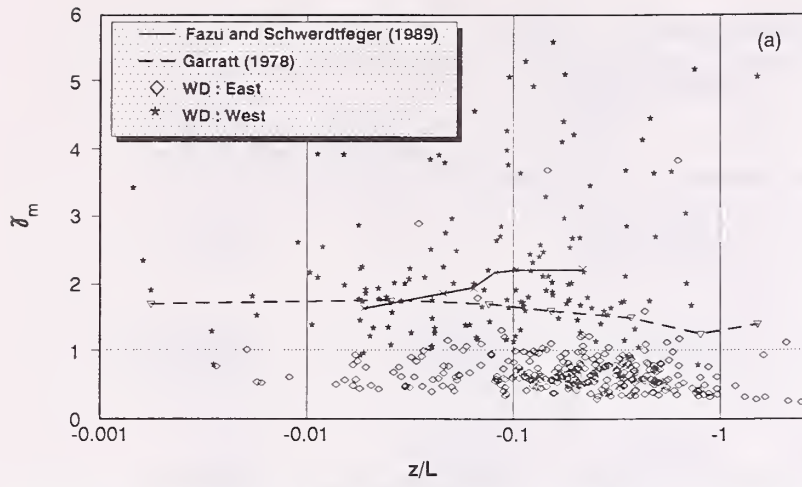


Figure 22a—Ratio of dimensionless wind shear (momentum) for empirically-established smooth-terrain conditions and measured dimensionless windshear [ $\gamma_m = \phi_m(\text{smooth})/\phi_m(\text{measured})$ ] vs. stability parameter ( $z/L$ ) for unstable conditions.

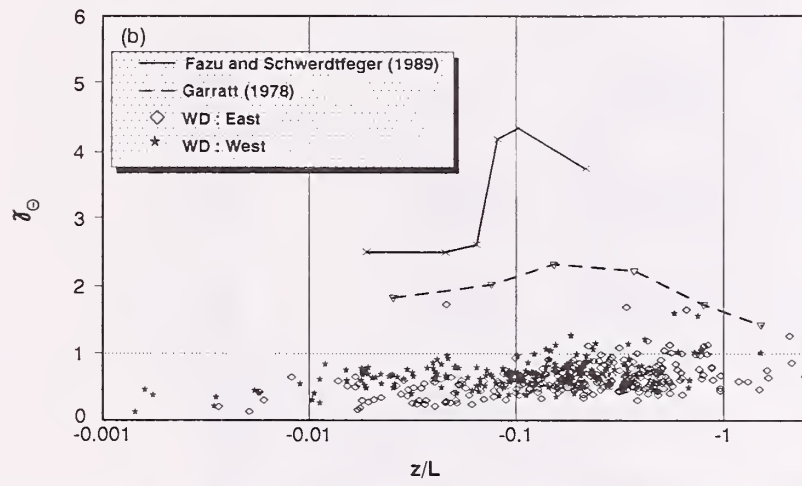


Figure 22b—Ratio of dimensionless sensible-heat gradient for empirically-established smooth-terrain conditions and measured dimensionless sensible-heat gradient [ $\gamma_h = \phi_h(\text{smooth})/\phi_h(\text{measured})$ ] vs. stability parameter ( $z/L$ ) for unstable conditions.

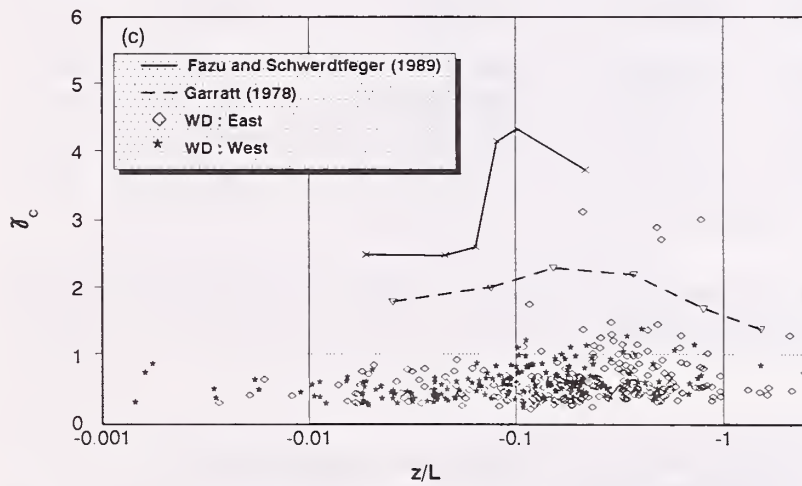


Figure 22c—Ratio of dimensionless sensible-heat gradient for empirically-established smooth-terrain conditions and measured dimensionless ozone gradient [ $\gamma_c = \phi_h(\text{smooth})/\phi_c(\text{measured})$ ] vs. stability parameter ( $z/L$ ) for unstable conditions.

Figure 24 shows the resulting  $K_q$  values for (a) ozone, (b) sensible heat, and (c) momentum vs.  $\zeta$  as determined strictly from field measurements, [21], and as determined using measured  $u_*$  and empirical  $\phi_q(\zeta)$ , [16a-b] and [26]. Except for measured  $K_m$  (west) and a

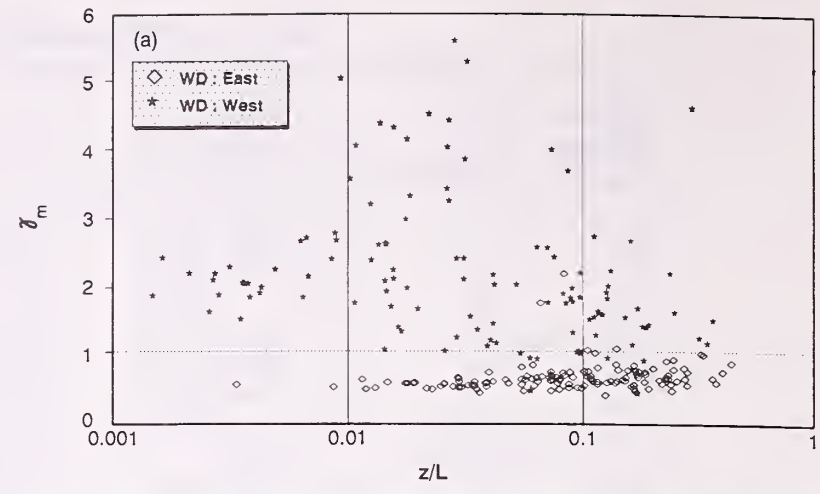


Figure 23a—Ratio of dimensionless wind shear (momentum) for empirically-established smooth-terrain conditions and measured dimensionless wind shear [ $\gamma_m = \phi_m(\text{smooth})/\phi_m(\text{measured})$ ] vs. stability parameter ( $z/L$ ) for stable conditions.

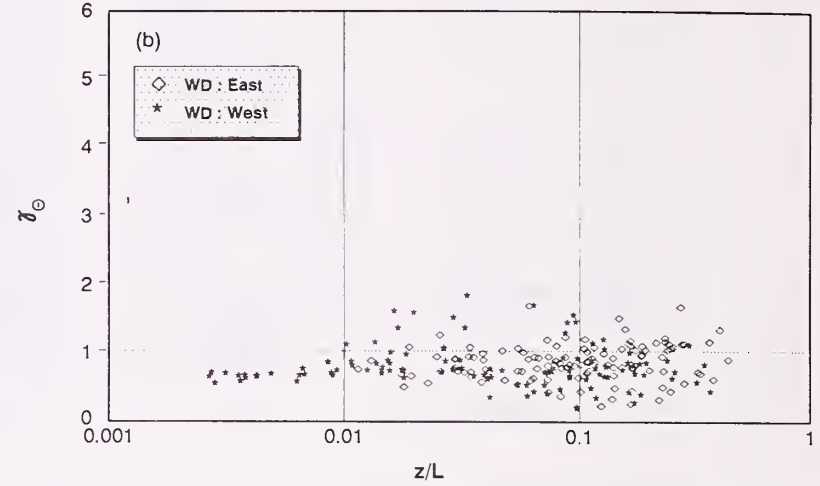


Figure 23b—Ratio of dimensionless sensible-heat gradient for empirically-established smooth-terrain conditions and measured dimensionless sensible-heat gradient [ $\gamma_h = \phi_h(\text{smooth})/\phi_h(\text{measured})$ ] vs. stability parameter ( $z/L$ ) for stable conditions.

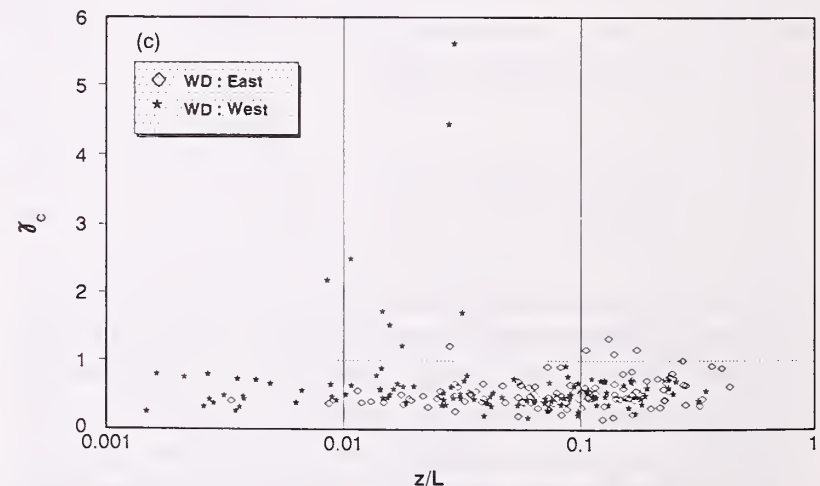


Figure 23c—Ratio of dimensionless sensible-heat gradient for empirically-established smooth-terrain conditions and measured dimensionless ozone gradient [ $\gamma_c = \phi_h(\text{smooth})/\phi_c(\text{measured})$ ] vs. stability parameter ( $z/L$ ) for stable conditions.

few scattered points, the measured values of  $K_q$  tend to be less than the corresponding calculated values. Again the choice of  $z$  plays a role in calculated  $K_m$ , [26]. The data distribution patterns vs. stability are very similar, however.

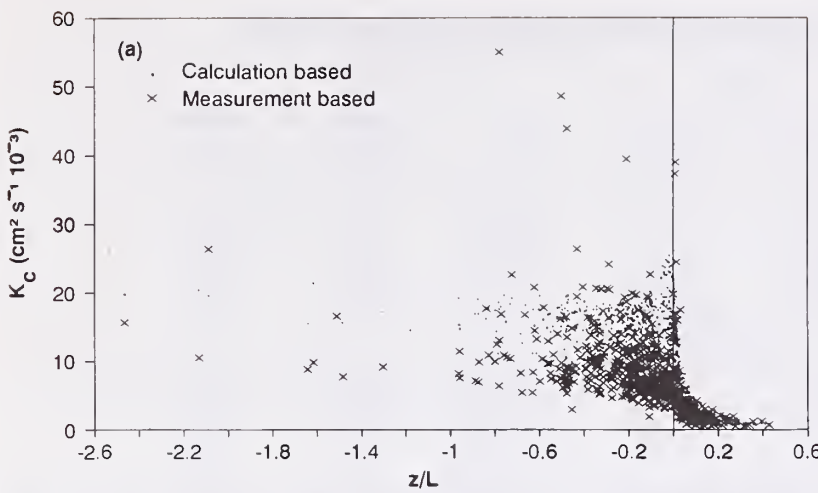


Figure 24a—Ozone eddy-diffusivity ( $K_c$ ) results; and calculated ozone eddy diffusivity based on measured friction velocity ( $u_*$ ) vs. stability parameter ( $z/L$ )—May 16-July 11, 1989.

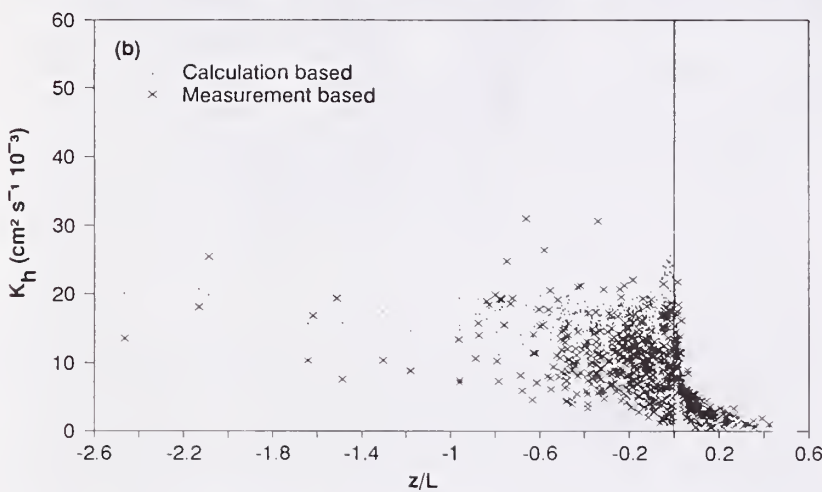


Figure 24b—Sensible-heat eddy-diffusivity ( $K_h$ ) results; and calculated sensible-heat eddy diffusivity based on measured friction velocity ( $u_*$ ) vs. stability parameter ( $z/L$ )—May 16-July 11, 1989.

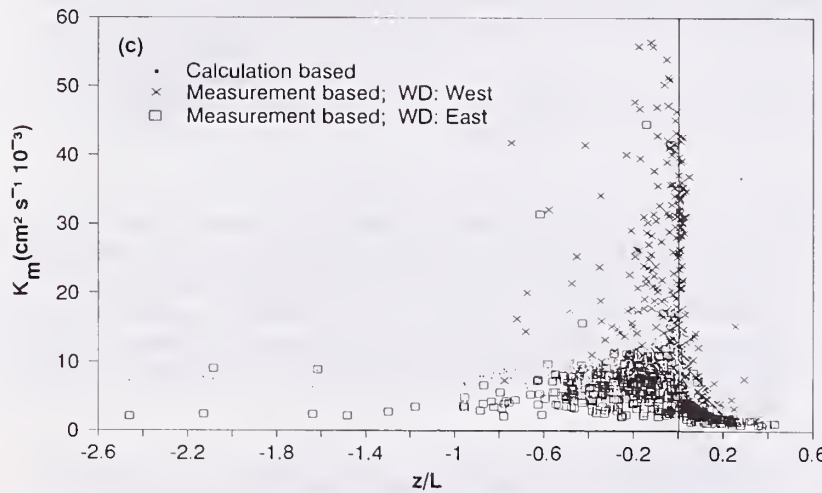


Figure 24c—Momentum eddy-diffusivity ( $K_m$ ) results for east- and west-wind categories; and calculated momentum eddy diffusivity vs. stability parameter ( $z/L$ )—May 16-July 11, 1989.

Calculated unstable  $K_c$  and  $K_h$  [26] tend to converge to about  $20,000 \text{ cm}^2 \text{s}^{-1}$  with increased  $-\zeta$ , while measured values tend to be lower and scattered ranging from below  $10,000$  to  $30,000 \text{ cm}^2 \text{s}^{-1}$  for both, with a few outliers above  $30,000$  for measured  $K_c$ . Stable eddy-diffusivity values for measured  $K_c$  and measured  $K_h$  follow the calculated values with considerably less data

scatter. Measured stable  $K_c$  values are generally less than calculated, and measured stable  $K_h$  values are about the same but exhibit more scatter.

Calculated unstable  $K_m$  values tend to converge to about  $9,000 \text{ cm}^2 \text{s}^{-1}$  with increased  $-\zeta$ , while measured values for the east-wind category tend toward lower values: about  $3,000 \text{ cm}^2 \text{s}^{-1}$ . Unstable, west-wind category, measured  $K_m$  values range from  $10,000 \text{ cm}^2 \text{s}^{-1}$  to as high as  $135,000$  (there are eight  $K_m$  values beyond  $60,000 \text{ cm}^2 \text{s}^{-1}$  not shown on fig. 24c). The swale west of the site is responsible for these extremely high values—measured  $\Delta \bar{u}$  values are considerably lower for the west-wind category measurements, resulting in higher  $K_m$  values. Stable, measured, east-wind category  $K_m$  values behaved similar to those of  $K_h$  when compared to calculated values, while west-wind category stable values are considerably higher.

Table 5 gives the linear regression results comparing measured  $K_{qm}$  (y-axis) and calculated  $K_{qT}$  (x-axis) values presented in figure 24 (the second subscript, m, refers to measured and T refers to empirical theory). Correlation coefficients (table 5) are reasonably good for all  $K_h$  values and stable values of  $K_c$  and  $K_m$ . Surprisingly, unstable measured  $K_{cm}$  values for ozone did not correlate well with calculated  $K_{cT}$  values. Remember unstable  $\phi_c$  values had better correlation coefficients compared to empirical theory than  $\phi_h$  values (see table 4).

The results presented in figure 24 and table 5 are not conducive to generating conclusions concerning possible relationships between  $K_c$  and  $K_m$  or  $K_h$ . Therefore, the ratios  $K_c/K_m$ ,  $K_h/K_m$ , and  $K_h/K_c$ , along with the empirical relationships plotted in figure 1, and the results determined from the regression [24a-d] are plotted in figures 25-27 (note  $K_h/K_c = \phi_c/\phi_h$ , etc.). [The  $K_h/K_c$  results are presented in figure 27 for all wind directions, the east-wind category, and the west wind category, respectively.]

The modeled eddy-diffusivity ratio lines in figures 25-27 are obtained by fitting the appropriate  $\phi$  regression, [24a-d], with the related regression parameters given in table 3. For instance, in figure 25 the  $K_c/K_m$  ratio line (large dashes) is  $\phi_m[24c]/\phi_c[24b]$  using the parameters from table 3 for the east regression results: for  $\phi_m[24c]$ ,  $b_1 = 1.03$ ,  $b_2 = -0.67$ , and  $b_3 = 11.6$ ; for  $\phi_c[24b]$ ,  $b_1 = -1.50$ ,  $b_2 = 1.95$ , and  $b_3 = 0.11$ .

In figure 25, the empirical ratio  $K_v/K_m$ , (Pruitt et al. 1971) for unstable conditions doesn't fit either the east- or the west-category data. The empirical ratio  $K_h/K_m$  (Swinbank 1968) is actually closer to the east  $K_c/K_m$  regression-based line for unstable conditions. The east  $K_c/K_m$  regression line for stable conditions is practically congruent with empirical  $K_v/K_m$ . For the west-wind category, the results are dominated by large-terrain-influenced  $K_m$  values— $K_c/K_m$  values are all small.

Table 5. — Regression results: eddy diffusivities of ozone, sensible heat, and momentum vs. calculated values.

Parameter	Stability <sup>+</sup>	Wind* dir.	K <sub>qT</sub>				No data points	Corr. coeff. (rho)
			slope	SE	const.	SE		
K <sub>cm</sub> vs K <sub>cT</sub>	u	All	0.37	±0.06	3590	±5200	453	0.26
	u	All	0.59	0.02	0	5260	453	0.20
	s	All	0.66	0.04	-593	3410	231	0.69
	s	All	0.60	0.03	0	3420	231	0.69
K <sub>hm</sub> vs K <sub>hT</sub>	u	All	0.97	0.04	-4920	3070	491	0.76
	u	All	0.67	0.01	0	3280	491	0.72
	s	All	0.74	0.03	402	1990	214	0.87
	s	All	0.78	0.02	0	2000	214	0.87
K <sub>mm</sub> vs K <sub>mT</sub>	u	West	1.81	0.49	8800	19800	159	0.28
	u	West	2.54	0.14	0	19900	159	0.26
	u	East	0.92	0.10	-1790	3600	319	0.44
	u	East	0.72	0.02	0	3610	319	0.44
	s	West	2.33	0.18	226	8860	120	0.77
	s	West	2.35	0.10	0	8830	120	0.77
	s	East	0.55	0.03	386	750	131	0.82
	s	East	0.63	0.02	0	768	131	0.81

+ u: unstable; s: stable

\* East: 030° - 250° azimuth (clockwise)

West: 250°-030° azimuth (clockwise)

All: all wind directions combined.

SE: Standard Error

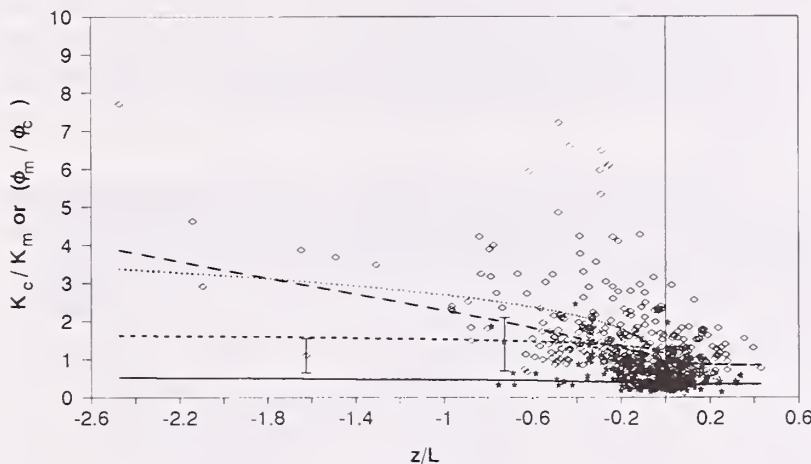


Figure 25—Ratio of the eddy diffusivities for ozone with the east- and west-wind category momentum eddy diffusivities (K<sub>c</sub>/K<sub>m</sub>); theoretical ratio of eddy diffusivities for sensible heat and momentum (K<sub>h</sub>/K<sub>m</sub>); theoretical ratio of eddy diffusivity for water vapor and momentum (K<sub>v</sub>/K<sub>m</sub>); and the ratio between regression-model east- and west-wind category dimensionless wind shear and the dimensionless ozone gradient vs. stability parameter (z/L).

(See Table 4. for equation and regression parameters.)

- K<sub>v</sub> / K<sub>m</sub> (Pruitt et al. 1971)
- ..... K<sub>h</sub> / K<sub>m</sub> (Swinbank 1968)
- φ<sub>m</sub>[24b] / φ<sub>c</sub> [24b]; z/L ≤ 0; west
- φ<sub>m</sub>[24a] / φ<sub>c</sub> [24a]; z/L > 0; west
- φ<sub>m</sub>[24c] / φ<sub>c</sub> [24b]; z/L ≤ 0; east
- φ<sub>m</sub>[24a] / φ<sub>c</sub> [24a]; z/L > 0; east
- \* WD : West
- ◇ WD : East
- Measurement error (precision)

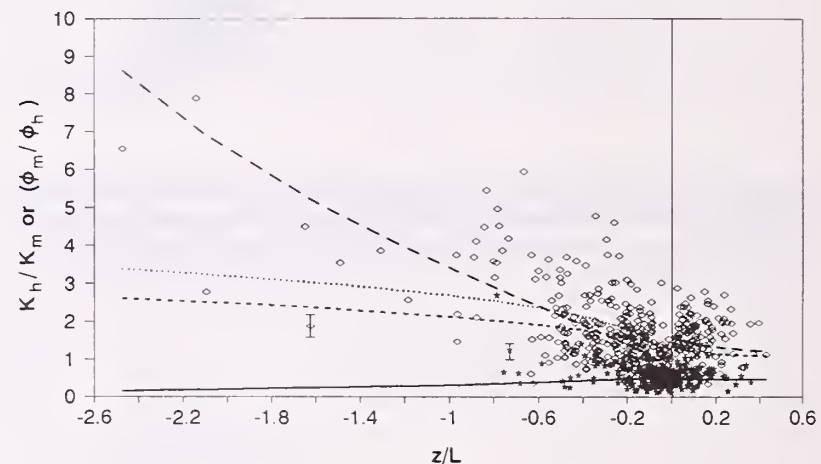


Figure 26—Ratio of the eddy diffusivity for sensible heat with the east- and west-wind category momentum eddy diffusivities (K<sub>h</sub>/K<sub>m</sub>); theoretical ratio of eddy diffusivity for sensible heat and momentum (K<sub>h</sub>/K<sub>m</sub>); and the ratio between regression-model east- and west-wind category dimensionless wind shear and the dimensionless sensible-heat gradient vs. stability parameter (z/L).

(See Table 4. for equation and regression parameters.)

- K<sub>h</sub> / K<sub>m</sub> (Businger et al. 1971)
- ..... K<sub>h</sub> / K<sub>m</sub> (Swinbank 1968)
- φ<sub>m</sub>[24b] / φ<sub>h</sub> [24b]; z/L ≤ 0; west
- φ<sub>m</sub>[24a] / φ<sub>h</sub> [24a]; z/L > 0; west
- φ<sub>m</sub>[24c] / φ<sub>h</sub> [24b]; z/L ≤ 0; east
- φ<sub>m</sub>[24a] / φ<sub>h</sub> [24a]; z/L > 0; east
- \* WD : West
- ◇ WD : East
- Measurement error (precision)

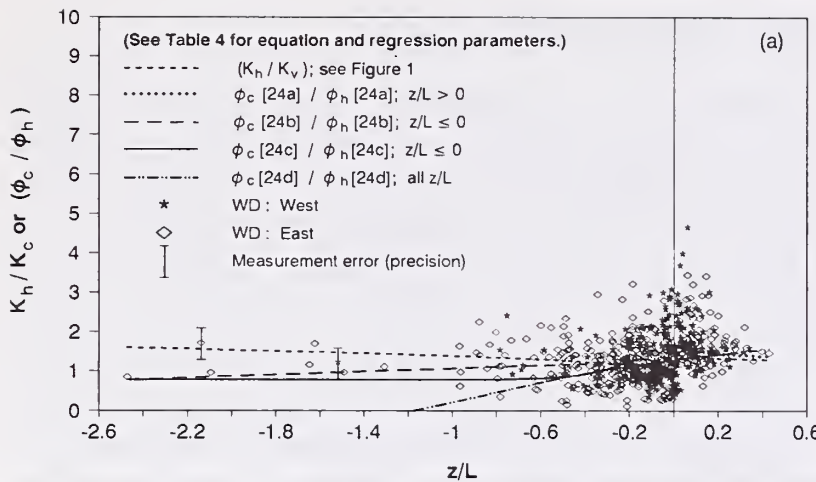


Figure 27a—Ratio of the eddy diffusivities for sensible heat with ozone eddy diffusivities ( $K_h/K_c$ ); theoretical ratio of eddy diffusivity for sensible heat and water vapor ( $K_h/K_v$ ); and the ratio between regression-model dimensionless ozone gradient with the dimensionless sensible-heat gradient for all wind directions vs. stability parameter ( $z/L$ ).

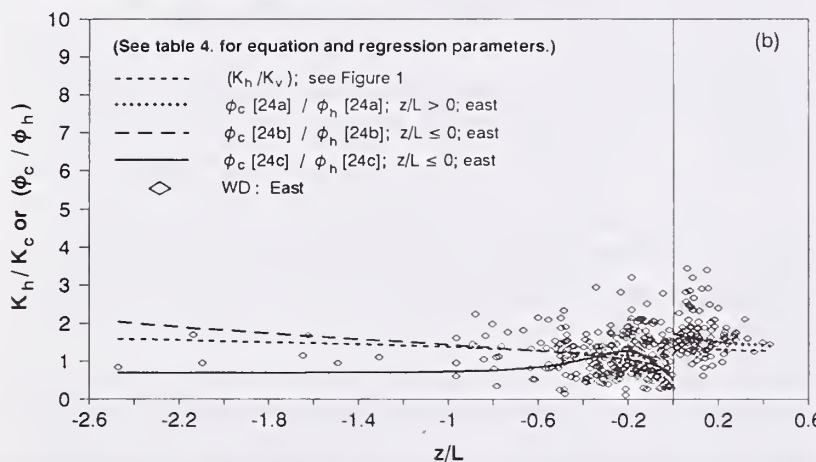


Figure 27b—Ratio of the eddy diffusivities for sensible heat with ozone eddy diffusivities ( $K_h/K_c$ ); theoretical ratio of eddy diffusivity for sensible heat and water vapor ( $K_h/K_v$ ); and the ratio between regression-model dimensionless ozone gradient with the dimensionless sensible-heat gradient for the east-wind category vs. stability parameter ( $z/L$ ).

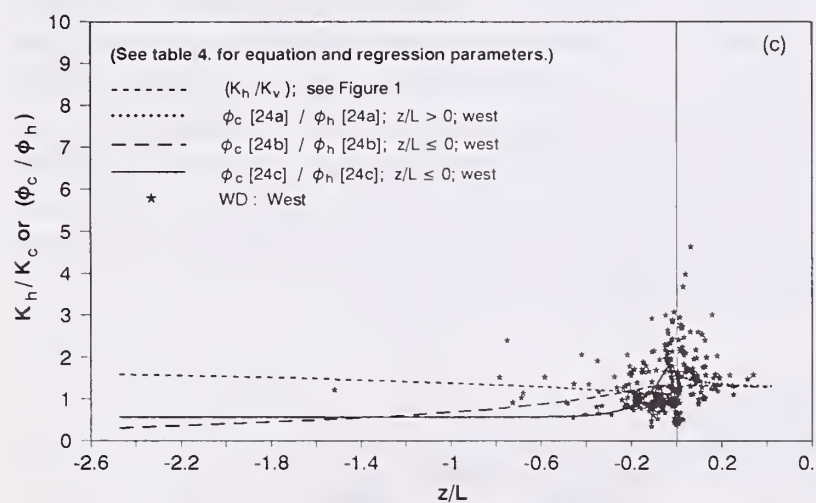


Figure 27c—Ratio of the eddy diffusivities for sensible heat with the ozone eddy diffusivities ( $K_h/K_c$ ); theoretical ratio of eddy diffusivity for sensible heat and water vapor ( $K_h/K_v$ ); and the ratio between regression-model dimensionless ozone gradient with the dimensionless sensible-heat gradient for the west-wind category vs. stability parameter ( $z/L$ ).

The  $K_h/K_m$  results in figure 26 are similar to the  $K_c/K_m$  results except that the east regression-based  $K_h/K_m$  line for unstable conditions increases dramatically as  $-\zeta$  gets larger. The shape and location of this line, particularly at larger values of  $-\zeta$ , is strongly influenced

by the few measured  $\phi$  values available for larger  $-\zeta$ . The ratio  $K_h/K_m$  is expected to increase to a constant value as  $\zeta \ll -1$  based on an argument that free convection dominates under these conditions and that turbulence is no longer dependent on  $u_*$  (Monin and Yaglom 1971). Monin and Yaglom (1971) also point out the idealized possibility that  $K_h/K_m \rightarrow \infty$  as  $u_* \rightarrow 0$  in free convection. However, they quickly recognize that vertical turbulence from thermals will continue to contribute to  $K_m$ , so that  $K_h/K_m$  should approach a constant as  $\zeta \ll -1$ . The results shown in figure 26 are inconclusive relative to an asymptotic value for  $K_h/K_m$  as measured  $\zeta$  only extends to -2.6; however, the tendency for greater  $K_h/K_m$  values for larger  $-\zeta$  is evident in the data.

The effect of free convection has been observed to begin at  $\zeta < -0.03$  (Fazu and Scwerdtfeger 1989, Monin and Yaglom 1971). In figure 26 there appears to be an explosion of east-category  $K_h/K_m$  values for  $\zeta < -0.1$ , which is not evident for  $K_c/K_m$  (fig. 25). Values of  $w'\theta'$  measured at the Pawnee site increase rapidly at  $\zeta < -0.1$ , also marking the beginning of stronger heat fluxes. For stable conditions the  $K_h/K_m$  results are similar to  $K_c/K_m$  with the east-category ratios slightly greater (fig. 26).

The  $K_h/K_c$  results in three figures (figs. 27a-c) show the effect of wind direction on the regression results. The ratios of the regression models for the all-wind category plotted in figure 27a show a tendency for  $K_h/K_c$  to decrease with slightly larger  $-\zeta$ . With the exception of the east-category, [24b], regression ratio in figure 27b, all the data-fitted regression ratios show the same tendency. This is not immediately evident upon examining the  $K_h/K_c$  data distribution by itself. If  $K_h/K_c$  does diminish with larger  $-\zeta$ , it is possible that the superadiabatic lapse rates associated with free convection (strong solar insulation and low wind speed), could be the influencing factor as  $K_h/K_c$  is inversely proportional to  $\Delta\theta$ . For stable situations, a good average for  $K_h/K_c$  appears to be at  $\sim 1.5$  for east-wind conditions and  $\sim 1.4$  for west-wind conditions.

For neutral conditions as  $\zeta \rightarrow 0$ ,  $\phi_q(\zeta)$  should approach the value 1 (Monin and Yaglom 1971). Hence, the eddy-diffusivity ratios should also approach 1. Diffusivity ratios were tested for this behavior by taking the average ratio of all values with  $|\zeta| < 0.03$ ; the numbers in parenthesis are the number of cases averaged and the  $\pm$  values are standard deviations of the averages:

Ratio	Wind Direction Category		
	All	East	West
$(K_c / K_m)$	$0.64 \pm \phi \sim 53$ (118)	$1.16 \pm 0.53$ (34)	$0.33 \pm 0.28$ (79)
$(K_h / K_m)$	$0.66 \pm 0.48$ (103)	$1.15 \pm 0.56$ (29)	$0.46 \pm 0.25$ (74)
$(K_h / K_c)$	$1.34 \pm 0.76$ (91)	$1.07 \pm 0.56$ (27)	$1.45 \pm 0.80$ (64)

The east-category neutral-stability results are very close to the value 1 for all three ratios, while the west-category results involving  $K_m$  are considerably less than 1, showing the effect of small measured  $\Delta \bar{u}$  values.

The west-category neutral-stability result for  $K_h/K_c$  is considerably larger than the east-category, which appears to contradict the claim that the measured values involved are not wind-direction dependent. Examination of the individual records used for these calculations revealed that there are a larger number of small positive  $\Delta \bar{\theta}$  values as a result of editing for the west-category compared to the east-category, thereby artificially raising the average. Figure 27a also shows that  $K_h/K_c$  values for the west-wind category close to  $\zeta = 0$  are somewhat larger but as a whole are distributed similar to the east-wind category.

The plotted  $K_h/K_c$  values in figure 27a appear to take a step jump at  $\zeta = 0$ , with higher values for  $\zeta > 0$  and lower values for  $\zeta < 0$ . The  $K_h/K_c$  values also tend to converge from a broad spread of data at  $\zeta = 0$  to a value  $\sim 1.5$  as  $\zeta \rightarrow 0.4$ , the largest  $\zeta$  values in this analysis. This behavior is not as evident for  $K_c/K_m$  (fig. 25) or for  $K_h/K_m$  (fig. 26). The effect is controlled by  $\Delta \bar{c}/\Delta \bar{\theta}$ ;  $\Delta \bar{\theta}$  is very small relative to  $\Delta \bar{c}$  near  $\zeta = 0$ , then  $\Delta \bar{\theta}$  gradually increases to provide a relatively fixed ratio for  $\Delta \bar{c}/\Delta \bar{\theta}$  between 2 and 3 ppb/°C for  $\zeta > 0.2$ .

## CONCLUSIONS

The reliability and validity of the Pawnee site flux and gradient data are established in the previous sections and in Zeller et al. (1989). In some cases the Pawnee site results verify existing knowledge, and in other cases the results are site-specific and deviate from the results of other investigators. The conclusions of this study relative to the Pawnee site measurements and to the vertical turbulent transport of ozone are given below. Table 6 provides a summary of the eddy-diffusivity ratio results for  $K_h/K_c$ ,  $K_h/K_m$  and  $K_c/K_m$ .

## Eddy Diffusivity Comparisons

The data and regression model eddy-diffusivity ratio results presented in figures 25-27, and the dimensionless gradient and regression results presented in figure 21, provide the basis for conclusions (table 6). The values of  $\phi_q$  for ozone, sensible heat, and momentum (even though the momentum results are wind-direction sensitive), are well behaved and add credence to the broadly distributed eddy-diffusivity ratios presented in figures 25-27. The  $\phi_q$  values obtained using data from two heights are sensitive to choice of  $z = 4.9$  m, which is evident in the plotted values of  $\gamma_q$  (figs. 22-23). It is also evident that Monin-Obukhov (M-O) similarity does not completely explain the behavior of  $\phi_m$  for west winds.

For  $K_h/K_c$  (fig. 27a) the conclusion  $K_c \approx K_h$  for unstable cases is reasonable within the experimental error of the study. The regression models for  $K_h/K_c$  ( $=\phi_c/\phi_h$ ) call attention to the possibility that  $K_h/K_c$  actually decreases with  $-\zeta$ . This is physically plausible if  $\bar{w}'c'$ ,  $\bar{w}'\theta'$  and  $\Delta \bar{c}$  are limited while  $\Delta \bar{\theta}$  increases with free convection. Since  $\Delta \bar{\theta}$  is also eventually limited, a lower asymptotic limit with  $\zeta \ll -1$  is most probable however.

For the stable case, results indicate  $K_c \neq K_h$ . The appropriate conclusion is that on the average  $K_h \approx 1.5 K_c$  for east winds and  $K_h \approx 1.4 K_c$  for west winds. It is most likely for stable situations that the chemical reactivity of ozone with surface constituents is playing a role and that this result is specific to ozone. During stable periods ozone is not replenished from above as rapidly as during unstable periods. This allows the ozone in the lowest layer to be depleted chemically while this would not happen to a nonreactive mass, hence larger  $\Delta \bar{c}$  values for ozone and consequently lower  $K_c$  values; therefore larger  $K_h/K_c$  ratios. The waning in  $K_h/K_c$  data scatter as  $\zeta$  increases from 0 supports the above argument as it indicates that a transition is taking place for measured  $\Delta \bar{\theta}/\Delta \bar{c}$  as stability intensifies.

Table 6. — Eddy diffusivities ratio results.

Ratio	Unstable		Stable	
	East* (smooth terrain)	West (irregular terrain)	East (smooth terrain)	West (irregular terrain)
$K_h/K_c$	$K_h \approx K_c$	$K_h \approx K_c$	$K_h \approx 1.5 K_c$	$K_h \approx 1.4 K_c$
$K_h/K_m$	+	$K_h \approx 0.5 K_m$	$K_h \approx 1.35 K_m$	$K_h \approx 0.5 K_m$
$K_c/K_m$	+	$K_c \approx 0.35 K_m$	$K_c \approx 0.9 K_m$	$K_c \approx 0.35 K_m$

\* East: wind direction 030° - 250° Azimuth.  
West: Wind direction 250°-030° Azimuth.  
+ conclusions not possible.

The regression results for  $K_h/K_m = \alpha$  (east-wind direction), as shown in figure 26 for unstable cases, provides an interesting argument for the theoretical free-convection ratio  $K_h/K_m \rightarrow \infty$ . There are too few data points to take this conclusion seriously: however, measured  $K_h/K_m$  are definitely larger than results presented for smooth terrain. A plausible explanation is that  $\Delta \bar{u}$  values are affected (increased) by the -1% terrain slope experienced by east winds. For stable  $K_h/K_m$  (east-wind direction) the measured results plotted in figure 26 indicate an average of 1.3:  $K_h/K_m \rightarrow 1.3$  as  $\zeta \rightarrow 0.4$ . Although the data scatter is significant, it is a reasonable result for stable cases where the constant  $\alpha \approx 1.35$  was expected. The results for  $K_h/K_m \approx \alpha$  (west-wind direction) are significant in that they demonstrate that the effect of irregular terrain is to lower the ratio of  $K_h/K_m$ . This is plausible as  $K_m$  would increase with increased turbulence mechanically generated by irregular terrain features. The average result  $K_h/K_m \approx 0.5$ , a constant for both stable and unstable conditions, should be restricted to the lower surface layer as the irregular-terrain effect would lessen with increased  $z$ .

The conclusions for  $K_c/K_m$  (fig. 25) are similar to the conclusions for  $K_h/K_m$ . The data distribution shown in figure 25 is very similar to figure 26, although the data values are different enough to generate a plausible regression-based  $K_c/K_m$  result for the unstable east-wind category (i.e.,  $K_c/K_m$  approaches an asymptotic limit as  $\zeta \rightarrow -\infty$ ). The regression-based  $K_c/K_m$  in figure 25 for  $\zeta < 0$  isn't too different from the  $K_h/K_m$  ratio provided by Swinbank (1968). For the stable east-wind category, the average  $K_c/K_m \approx 0.9$ , which is very close to the result provided by Pruitt et al. (1971) for  $K_v/K_m$ . For both stable and unstable west-wind categories, the average ratio  $K_c/K_m \approx 0.35$  is perhaps a useful result for the lower surface layer in irregular terrain.

The comparison  $K_c = K_v$ , with  $K_v$  (different from  $K_h$ ) based on the empirical expression given in [11] seems reasonable for stable conditions but not for unstable conditions (with the exception of the east-wind regression model [24b]) based on the results shown in figures 25 and 27a. Because of the chemical nature of ozone this conclusion is specific to ozone.

Table 6 provides a summary of the conclusions discussed above. All results for stable conditions are consistent within respective wind-direction categories (i.e.,  $K_h/K_c = (K_h/K_m)/(K_c/K_m)$ ). There are no conclusions for the unstable east category. The unstable west category conclusions are not consistent within themselves (i.e.,  $K_h \neq K_c$  if  $K_h \approx 0.5K_m$  and  $K_c \approx 0.35K_m$ ) because the results  $K_h \approx K_c$  for unstable west-wind conditions are based on data that for the most part are associated with near neutral stability,  $\zeta > -0.2$  (fig. 27c); they are, however, the best conclusions that can be reached given the distribution in eddy-diffusivity ratio results.

## Constant Flux Layer

The 8- and 3-meter measurement heights used at the Pawnee site are too closely spaced to expect detection of any significant flux differences; hence, the terms "constant flux" and "constant flux divergence" are synonymous for this analysis. The measurement results for corrected fluxes (fig. 20) compared to those for uncorrected fluxes (fig. 16), show that the constant-flux layer assumption for sensible heat and momentum is reasonable, as the results are essentially the same for both.

For ozone, the constant flux or flux-divergence layer assumption is not as easy to evaluate. Figure 17, the results for uncorrected ozone flux (corrected for heat flux), shows that there is definitely less flux measured at the 3-meter height compared to the 8-meter height. These data show strong flux divergence in the downward direction (i.e. less flux at 3 meters compared to 8) as would be expected. This is based on assuming ozone is supplied from above 8 meters and is not generated between 8 and 3 meters. It is unknown in this study if the measured rate of flux divergence for  $w'c'$  would continue above 8 meters; however, it is unlikely based on aircraft measurements at higher elevations that report flux-related values for ozone in the same range as measured at the Pawnee site (Lenschow 1982). The results for corrected ozone flux shown in figure 18, obtained by applying all known and/or theorized flux corrections, show that a constant flux layer (as opposed to a constant flux-divergence layer) for ozone is statistically acceptable in that  $w'c'(8 \text{ m}) = w'c'(3 \text{ m})$  within a 95% confidence interval.

The results in figure 18 are quite scattered and are produced by flux corrections that average +45% for 8 meters and +85% for 3 meters. The corrections for stable cases are particularly large and uncertain, and the corrections for unstable cases are large compared to the heat-flux correction for  $w'c'$  (maximum: -25%). After evaluating the corrected and uncorrected ozone flux, there are still two questions: how valid are the flux corrections; and, can reactions with NOx species, aerosols, and NMHC's above 3 meters really be discounted? For these reasons the constant flux or the constant flux-divergence question for ozone flux is still open to further research. However, assuming the flux corrections tested are at least partially correct and that net ozone production between 3 and 8 meters is minimal, the assumption of a constant flux for ozone is reasonable.

## Other Findings

The vertical transport and gradients of ozone and sensible heat behave similarly. Dimensionless gradient

values,  $\phi_q$ , for both parameters follow M-O similarity. The gradient of ozone has a diurnal pattern that appears to be controlled by a combination of sources and sinks as well as boundary-layer mixing height.

Terrain features have a dramatic effect on  $K_m$  and  $\phi_m$  by affecting  $\Delta \bar{u}$ , while terrain effects on  $z_o$  (calculated with [17a] and  $\zeta$  as well as  $K_c$ ,  $K_h$ ,  $\phi_c$ , and  $\phi_h$  are not discernible.

Flux-measurement corrections for inadequate sensor response are measurement-height sensitive and play a factor in measured results at lower measurement elevations for ozone. Flux corrections for sensible heat flux and momentum flux are not as sensitive to elevation.

## Recommendations for Further Research

The following list of questions, based on the results of this investigation, provide recommendations for future research.

- Does the ratio  $K_c/K_h$  for ozone and heat diminish with increasing  $-\zeta$ ?
- Is the measured flux divergence for ozone within the surface layer as strong as indicated by the Pawnee site measurements and how high does it extend before becoming constant? (The answer will require simultaneous flux measurements from more than two heights.)
- What controls the transition of  $\Delta \bar{c}/\Delta \bar{\theta}$  for  $0 > \zeta > 0.2$  from widely fluctuating values to a relatively stable ratio?
- How important are the response-related flux corrections for fluxes measured under stable conditions, and what can be done to improve the corrections in general?
- Does  $K_h/K_c$  for a nonreactive depositing mass tracer, where  $c$  is not ozone, behave differently from  $K_h/K_c$  where  $c$  is ozone?

## REFERENCES

Arya, S.P. 1988. Introduction to micrometeorology. Volume 42. Academic Press, Inc. International Geophysics Series. San Diego, CA. 307 p.

Bache, D.H. 1986. Momentum transfer to plant canopies: influence of structure and variable drag. *Atmospheric Environment*. 20(7): 1369-1378.

Baker, C.B. 1988. Private communication between C.B. Baker (U.S. Environmental Protection Agency, NC) and W.J. Massman (U.S. Forest Service, Fort Collins, CO).

Bird, R.B.; Stewart, W.E.; Lightfoot, E.N. 1960. Transport phenomena. John Wiley and Sons, Inc., NY: 379 and 629.

Brutsaert, W. 1988. Evaporation into the atmosphere: theory, history, and application. D. Reidel Publishing Company. Boston. 299 p.

Busch, N.E. 1973. On the mechanics of atmospheric turbulence. In: Haugen, D.A., ed. Workshop on micrometeorology. American Meteorological Society. Boston: 1-65.

Businger, J.A. 1986. Evaluation of the accuracy with which dry deposition can be measured with current micrometeorological techniques. *Journal of Climate and Applied Meteorology*. 25: 1100-1124.

Businger, J.A.; Wyngaard, J.C.; Izumi, Y.; Bradley, E.F.; 1971. Flux profile relationships in the atmosphere surface layer. *Journal of Atmospheric Sciences*. 28: 181-189.

Caughey, S.J. 1981. Observed characteristics of the atmosphere boundary layer. In: Nieuwstadt, F.T.M.; Van Dop, H., ed. Atmospheric turbulence and air pollution modelling. D. Reidel Publishing Company. Dordrecht, Holland: 107-158.

Cermak, J.E. 1975. Simulation of atmospheric boundary layers in wind tunnels. In: Lenschow, D.H.; ed. Instruments and techniques for probing the atmospheric boundary layer. NCAR. Boulder, CO: 66-71.

Cermak, J.E.; Horn J.D. 1968. Tower shadow effect. *Journal of Geophysical Research*. 73(6): 1869-1876.

Chang, J.S.; Brost R.A.; Isaksen, I.S.A.; Madronich, S.; Middleton, W.R.; Stockwell, W.R.; Walcek, C.J. 1986. A three-dimensional eulerian acid deposition model: physical concepts and formulation. *Journal of Geophysical Research*. 92(D12): 14681-14700.

Clarke, J.F.; Ching, J.K.S.; Godowitch, J.M. 1982. An experimental study of turbulence in an urban environment. Environmental Protection Agency Report EPA/600/09. Research Triangle Park, NC. 167 p.

Conklin, P.S. 1988. Private communication between P.S. Conklin (Duke University, N.C.) and W.J. Massman (U.S. Forest Service, Fort Collins, CO).

Conklin, P.S.; Knoerr, K.R., Schneider, T.W.; Baker, C.B. 1988. A wind tunnel test of probe shadow effects on a sonic anemometer in two orientations. Eighth symposium on turbulence and diffusion. American Meteorological Society. San Diego, CA. 4 p.

Delany, A.C.; Fitzjarrald, D.R.; Lenschow, D.H. [and others]. 1986. Direct measurement of nitrogen oxides and ozone fluxes over grassland. *Journal of Atmospheric Chemistry*. 4: 429-444.

Droppo, J.G., Jr. 1985. Concurrent measurements of ozone dry deposition using eddy correlation and profile flux methods. *Journal of Geophysical Research*. 90: 2111-2118.

Edinger, J.G. 1973. Vertical distribution of photochemical smog in Los Angeles basin. *Environmental Science and Technology*. 7(3): 247.

Fazu, C.; Schwerdtfeger, P. 1989. Flux-gradient relationships for momentum and heat over a rough

natural surface. *Quarterly Journal of the Royal Meteorological Society*. 115: 335-352.

Fitzjarrald, D.R.; Lenschow, D.H. 1983. Mean concentration and flux profiles for chemically reactive species in the atmospheric surface layer. *Atmospheric Environment*. 17: 2505-2512.

Galbally, I.E. 1971. Ozone profile and ozone fluxes in the atmosphere surface layer. *Quarterly Journal Royal of the Meteorological Society*. 87: 18-29.

Garratt, J.R. 1978. Flux profile relations above tall vegetation. *Quarterly Journal of the Royal Meteorological Society*. 104: 199-211.

Haltner, G.J.; Martin, F.L. 1957. *Dynamical and physical Meteorology*. McGraw-Hill, NY: 222-223.

Haugen, D.A.; Kaimal, J.C.; Bradely, E.F. 1971. An experimental study of Reynolds stress and heat flux in the atmospheric surface layer. *Quarterly Journal of the Royal Meteorological Society*. 97: 168-180.

Hicks, B.B. 1984. Volume 4. Deposition both wet and dry. Acid precipitation series. Butterworth Publishers. Boston. 9 Volume.

Högström, U. 1988. Non-dimensional wind and temperature profiles in the atmospheric surface layer: a re-evaluation. *Boundary-Layer Meteorology*. 42: 55-78.

Højstrup, J. 1981. A simple model for the adjustment of velocity spectras in unstable conditions downstream of an abrupt change in roughness and heat flux; *Boundary-Layer Meteorology*. 21: 341-356.

Jacobi, W.; André, K. 1963. The vertical distribution of radon 222, radon 220 and their decay products in the atmosphere. *Journal of Geophysical Research*. 68(13): 3799-3814.

Kaimal, J.C. 1969. Measurement of momentum and heat flux in the surface boundary layer. *Radio Science*. 4: 1147-1153.

Kaimal, J.C., 1975. Sensors and techniques for direct measurement of turbulent fluxes and profiles in the atmospheric surface layer. In: Lenschow, D.H., ed. *Instruments and techniques for probing the atmospheric boundary layer*. NCAR. Boulder, CO: 7-14.

Kaimal, J.C. 1989. Private communication.

Kaimal, J.C.; Wyngaard, J.C.; Izumi, Y.; Cote, O.R. 1972. Spectral characteristics of surface-layer turbulence. *Quarterly Journal Royal of the Meteorological Society*. 98: 563-589.

Kao, S.K. 1984. Theories of atmospheric transport and diffusion. In: Randerson, D., ed. *Atmospheric science and power production*. U.S. Department of Energy DOE/TIC-27601.

Korrel, A.; Panosky, H.A. [Panofsky]; Rossi, R.J.; 1982. Wind profiles at the Boulder tower. *Boundary Layer Meteorology*. 22: 295-312.

Kristensen, L.; Fitzjarrald, D.R. 1984. The effect of line averaging on scalar flux measurements with a sonic anemometer near the surface. *Journal of Atmospheric and Oceanic Technology*. 1: 138-146.

Lenschow, D.H. 1982. Reactive trace species in the boundary layer from a micrometeorological perspective. *Journal of the Meteorological Society of Japan*. 60: 472-480.

Lenschow, D.H.; Delany, A.C.. 1987. An analytic formulation for NO and N02 flux profiles in the atmospheric surface layer. *Journal of Atmospheric Chemistry*. 5: 301-109.

Lettau, H. 1951. Diffusion in the upper atmosphere. In: *Compendium of meteorology*. American Meteorological Society. Boston: 320-333.

Liu, S.C.; Trainer, M.; Fehsenfeld, F.C.; Parrish, D.D.; Williams, E.J.; Fahey, D.W.; Hubler, G.; Murphy, P.C. 1987. Ozone production in the tural troposphere and the implications for regional and global ozone distribution. *Journal of Geophysical Research*. 92: 4191-4207.

Massman, W.J. 1991. The attenuation of concentration fluctuations in turbulent flow through a tube. *Journal of Geophysical Research*. Volume 96, Number D8: 15.

Massman, W.J.; Fox, D.G., Zeller, K.F., Lukens, D. 1990. Verifying eddy correlation measurements: a study of the energy balance components of the pawnee grasslands. US Department of Agriculture, Forest Service, Rocky Mountain Forest and Range Experiment Station. Research Paper RM-288. Fort Collins, CO. 14 p.

McMillen, R.T. 1986. A basic program for eddy correlation in non-simple terrain. NOAA Technical Memorandum; ERL ARL-147. ATDD. Oak Ridge, TN. 32 p.

McRae, G.J., Russell, A.G. 1984. Dry deposition of nitrogen-containing species. Chapter 9. In: Hicks, B.B., ed. *Deposition both wet and dry*. Volume 4. Butterworth Publishers. Boston: 153-193.

Meyers, T.P.; Yuen, T.S. 1987. An assessment of averaging strategies associated with day/night sampling of dry deposition fluxes of  $\text{SO}_2$  and  $\text{O}_3$ . *Journal of Geophysical Research*. Volume 192, Number D6. 6705-6712.

Monin, A.S.; Yaglom, A.M. 1971. *Statistical fluid mechanics: mechanics of turbulence Volume 1*. The MIT Press. Cambridge. 769 p.

Moore, C.J. 1986. Frequency response corrections for eddy correlation systems. *Boundary Layer Meteorology*. 37: 17-35.

Munn, R.E. 1961. *Descriptive micrometeorology*. Academic Press. NY 245 p.

NCAR. 1985. The NCAR eulerian regional acid deposition model. ADMP-85-3 NCAR/TN-256+STR. Boulder, CO.

NRC. 1983. *Acid deposition atmospheric processes in North America*. National Academy Press. Washington, D.C. 375 p.

Oke, T.R. 1978. Boundary layer climates. Methuen & Co Ltd. London. 372 p.

Panofsky, H.A.; Dutton, J.A. 1984. Atmospheric Turbulence. John Wiley and Sons. NY. 397 p.

Press, W.H.; Flannery, B.P.; Teukolsky, S.A.; Vetterling, W.T., 1986. Fourier transform spectral methods. In: Numerical recipes. Cambridge University Press: 381-453.

Pruitt, W.O.; Morgan, D.L.; Lawrence, F.J. 1971. Evaluation of eddy-transfer coefficients and diabotic-profile functions under turbulent flow in the lower atmosphere. Chapter 3 In: Analysis of energy, momentum and mass transfer. ECOM Report 68-F10-F. University of California, Davis.

Randerson, D. 1984. Atmospheric science and power production. Editor. U.S. Department of Energy DOE/TIC-27601. 805 p.

Ray, J.D.; Stedman, D.H.; Wendel, G.J. 1986. Fast chemiluminescent method for measurement of ambient ozone. *Analytical Chemistry*. 58: 598-600.

Rider, N.E.; Robinson, G.D. 1951. A study of the transfer of heat and water vapor above a surface of short-grass. *Quarterly Journal of the Royal Meteorological Society*. 77: 375-401.

Rohsenow, W.M.; Choi, H. 1961. Heat, mass and momentum transfer. Prentice-Hall, Inc. Englewood Cliffs, NJ. 411 p.

Rosenberg, N.J. 1974. Microclimate: the biological environment. John Wiley and Sons, NY. 315 p.

Sandborn, V.A. 1981. Class notes for experimental methods in fluid mechanics. Department of Civil Engineering. Colorado State University. Fort Collins, Colorado.

Sellers, W.D. 1965. Physical climatology. University of Chicago Press. 272 p.

Stocker, D.W.; Lukens, D.L. 1988. Research protocol methodology and quality assurance plans for the USFS Pawnee eddy correlation dry deposition site. Appendix B. In: Zeller, K.F. USFS Pawnee dry deposition research site (western core site), FY-88 operation: progress report number 1, EPA/ORD IA DW12933093-01-0, November.

Stocker, D.W.; Stedman, D.H.; Massman, W.J.; Zeller, K.F.; Fox, D.G; 1989. Measurement of the dry deposition of nitrogen oxides to a prairie ecosystem by eddy correlation. Air and waste management association 82nd annual meeting. Paper Number 89-157.5. 12 p.

Swinbank, W.C. 1968. A comparison between predictions of dimensional analysis for the constant-flux layer and observations in unstable conditions. *Quarterly Journal of the Royal Meteorological Society*. 94: 460-467.

TECO; 1986. Model 49/49PS U.V. photometric ambient  $O_3$  analyzer/calibrator instruction manual. Thermo Electron Corporation. Hopkinton, Mass.

Venkatram, A.; Karamchandani, P.K.; Misra, P.K. 1988. Testing a comprehensive acid deposition model. *Atmospheric Environment*. 22(4): 737-747.

Volkov, Y.A.; Yelagina, L.G.; Lazarev, A.I., Lomadze, S.O. 1986. Simultaneous measurements of moisture and carbon dioxide fluxes in the atmosphere near the earth. *Izvestiya, Atmospheric and Ocean Physics*. 22(7): 591-595.

Vukovich, F.M.; Fishman, J.; Browell, E.V. 1985. The reservoir of ozone in the boundary layer of the Eastern United States and its potential impact on the global tropospheric ozone budget. *Journal of Geophysical Research*. 90: D3 5687-5698.

Walcek, C.J.; Brost R.A., Chang J.S.; Wesely, M.L. 1986.  $SO_2$ , sulfate and  $HNO_3$  deposition velocities computed using regional land use and meteorological data. *Atmospheric Environment*. Volume 20 (5): 949-964.

Walcek, C.J.; Chang, J.S. 1987. A theoretical assessment of pollutant deposition to individual land types during a regional-scale acid deposition episode. *Atmospheric Environment*. Volume 21(5): 1107-1113.

Webb, E.K.; Pearman; G.I.; Leuning, R. 1980. Correction of flux measurements for density effects due to heat and water vapor transfer. *Quarterly Journal of the Royal Meteorological Society*. 106: 85-100.

Wesely, M.L. 1970. Eddy correlation measurements in the atmospheric surface layer over agricultural crops. University of Wisconsin. 102p. Ph.D. thesis.

Wesely, M.L.; Cook, D.R.; Williams, R.M. 1981. Field measurements of small ozone fluxes to snow, wet bare soil, and lake water. *Boundary Layer Meteorology*. 10: 459-471.

Wesely, M.L., Eastman, J.A., Cook, D.R. and Hicks, B.B. 1978. Daytime variations of ozone eddy fluxes to maize. *Boundary Layer Meteorology*. 15: 361-373.

Wesely, M.L.; Eastman, J.A.; Stedman, D.H.; Yalvac, E.D. 1982. An eddy-correlation measurement of  $N_2O$  flux to vegetation and comparison to  $O_3$  flux. *Atmospheric Environment*. 16 (4): 815-820.

Wesely, M.L.; Lenchow, D.H.; Denmead, O.T. 1989. Flux measurement techniques. Chapter 2 In: Lenchow, D.H.; Hicks, B.B., ed. *Global tropospheric chemistry-chemical fluxes in the global atmosphere*. NCAR. Boulder, CO: 31-46.

Williams, E.J. 1990. Private communication.

Woodruff, B. 1986. Sampling error in single-instrument vertical gradient measurements in the atmospheric surface layer. Colorado State University. 79 p. M.S. thesis.

Wyngaard, J.C. 1973. On surface-layer turbulence. In: Haugen, D.A., ed. *Workshop on micrometeorology*. Boston, MA. American Meteorological Society: 101-147.

Wyngaard, J.C. 1989a. Private communication. December 5, 1989.

Wyngaard, J.C. 1989b. Scalar fluxes in the planetary boundary layer - theory, modeling, and measurement. To be published in Volume 50. *Boundary Layer Meteorology*.

Wyngaard, J.C.; Zhang S.F. 1985. Transducer - shadow effects on turbulence spectra measured by sonic anemometers. *Journal of Atmospheric and Oceanic Technology*. 2: 548-558.

Yaglom, A.M. 1977. Comments on wind and temperature flux-profile relationships. *Boundary-Layer Meteorology*. 11: 89-102.

Zeller, K.F. 1988. USFS Pawnee dry deposition research site (western core site), FY-88 operation: progress report number 1, EPA/ORD IA DW12933093-01-0, November.

Zeller, K.F. 1990. Eddy diffusivities for sensible heat, ozone and momentum from eddy correlation and gradient measurements: Colorado State University. 140p. PhD. thesis.

Zeller, K.F.; Evans, R.B.; Fitzsimmons, C.K.; Siple, G.W. 1977. Mesoscale analysis of ozone measurements in the Boston Environs. *Journal of Geophysical Research* 82(37): 5879-5888.

Zeller, K.F.; Fox, D.; Massman, W. 1990. Simultaneous measurements of the eddy diffusivities and gradients of ozone, sensible heat, and momentum. Ninth symposium on Turbulence and Diffusion. April 30 - May 3, 1990. AMS. Roskilde, Denmark: 110-114.

Zeller, K.F.; Hazlett, D.L. 1989. Ozone deposition and leaf area index at the Pawnee National Grassland for the 1988 growing season. In: Olson, R.K., Lefohn, A.S., ed. *Effects of air pollution on western forests*. Air Waste and Management Association. Pittsburgh, PA: 177-192.

Zeller, K.F.; Massman, W.J.; Stoker, D.W.; Fox, D.G.; Stedman, D.H.; Hazlett, D. 1989. Initial results from the Pawnee eddy correlation system for dry acid deposition research. US Department of Agriculture Forest Service, Rocky Mountain Forest and Range Experiment Station, Research Paper RM-282. Fort Collins, CO. 32 p.

## APPENDIX A. DATA ACQUISITION AND HANDLING

### Data Acquisition and Real-Time Computations

Data collection and processing were accomplished using a PC (Compaq 386) interfaced with an analog-to-digital conversion board (DT2805). Eight channels were available on each of two boards for data acquisition. A total of 16 channels (table A-1) were sampled at ca. 14 Hz. Output measures include means, variances, covariances, and other micrometeorological quantities. The software used for real-time data processing was adapted from the BASIC flux program for eddy correlation in nonsimple terrain developed by McMillen (1986). The compiled flux program is capable of running the entire eddy-correlation measurement system unattended for several days. Tasks accomplished in real-time by this program include real-time data acquisition and processing, raw data storage if required, statistical summaries at the end of the assigned averaging period (usually one-half hour), and instrumentation zero each half hour to ensure accurate chemical measurements. Fluctuations for each data point ( $c'(t)$ ,  $\theta'(t)$ ,  $w'(t)$ , etc.) were calculated in real-time by subtracting the instantaneous signal from a 200-second running mean generated by using a recursive digital filter:

$$\bar{c}(t) = [c(t) / (200 * n)] - \left[ \bar{c}(t-1) \left( 1 - \frac{1}{200 * n} \right) \right]$$

$$c'(t) = c(t) - \bar{c}(t) \quad [A-1]$$

where  $n$  = sampling frequency.

The value 200 seconds was chosen to maximize the covariance based on test calculations and experience with other surface-layer eddy correlation experiments (McMillen 1986). The covariance calculations involving wind and ozone concentration were handled in real-time by saving the wind data,  $u(t)$ ,  $v(t)$ , and  $w(t)$  for lagtime \*  $n$  data collection loops. For example, if lagtime = 2 seconds and the data were collected at 14 Hz,  $14 * 2 = 28$ , then:

$$w'c'(t) = w'(t - 28)c'(t)$$

$$u'c'(t) = u'(t - 28)c'(t) \quad [A-2]$$

$$v'c'(t) = v'(t - 28)c'(t)$$

where  $t = 1$  is equivalent to 1/14 second.

At the end of each half-hour sampling period, the mean horizontal wind direction (resulting  $\bar{v} = 0$ ),  $\eta$ ; the vertical mean wind direction (mean streamline, resulting  $\bar{w} = 0$ ),  $\theta$ ; and the streamline "twist" angle (resulting  $w'v' \approx 0$ ),  $\beta$ , were calculated and the sampled covariance matrix,  $[M]$ , was then rotated three times ( $\eta$ ,  $\theta$  and  $\beta$ ) so that the output covariances were aligned with the mean wind streamline (Wesely 1970).

$$[M] = \begin{bmatrix} \overline{w'^2} & \overline{w'u'} & \overline{w'v'} & \overline{w'T'} & \overline{w'c'} \\ \overline{u'w'} & \overline{u'^2} & \overline{u'v'} & \overline{u'T'} & \overline{u'c'} \\ \overline{v'w'} & \overline{v'u'} & \overline{v'^2} & \overline{v'T'} & \overline{v'c'} \end{bmatrix} \quad [A-3]$$

While the above calculations were made and all summary data (table A-1) were stored, the chemical instruments were zeroed and all parameters were reinitiated for the next sample period. The chemical instruments were then stabilized with ambient air prior to commencement of the next data-collection period. The above tasks required ca 1.8 minutes per half-hour data-acquisition cycle.

### Data Editing

Data handling and editing for eddy-correlation measurements must be accomplished with great care. The flux measurement is a statistical covariance that becomes meaningless if either timing, calibrations, or calculations are off. In addition to the quantities listed in table A-1, calibration values, calibration offsets, and the variance of each covariance are also calculated and stored. There were 171 data averages archived every half hour. Data handling must be carefully monitored. Prior to testing for stationarity and homogeneity, to eliminate data that may have contained bogus or corrupt information, records that met the criteria listed in table A-2 were eliminated. Korrell et al. (1982) used similar wind-related criteria for their surface-layer analysis of Boulder tower data, Fazu and Schwerdtfeger (1989) also applied similar data-editing criteria for wind and temperature flux and gradient data collected over bushland in Australia.

### Ozone Gradient Determination

A correct  $\Delta \bar{c}$  measurement for ozone is important for the eddy-diffusivity calculation [20]. This analysis used  $\Delta \bar{c}$  data determined from two TECO ozone analyzers sampling from two different heights, rather than the traditional approach of switching the inlet of a single analyzer between two levels, which leads to errors (Woodruff 1986). The  $\Delta \bar{c}$  measurement technique used alternated the level each TECO monitored every half hour through the use of two three-way computer-controlled solenoid switches. Since each CAAM was plumbed to a single level and not allowed to switch between levels during any 1-week sampling period while the TECOs did switch, four sets of instrument regression calibrations similar to figure 5 could be extracted: CAAM1:TECO1; CAAM1:TECO2; CAAM2:TECO1; and CAAM2:TECO2. Hence, two separate cali-

Table A-1. — Data acquisition and real-time measured quantities at the Pawnee site.

DT 2805 channel no.	Quantity	Height (m)	Output (every 1/2 hour)
1	w: vertical wind speed component	8	$\bar{w}, w'^2$
2	u: horizontal wind speed component	8	$\bar{u}, u'^2$
3	v: horizontal wind speed component	8	$\bar{v}, v'^2$
4	T: temperature ( $\theta \approx 1.05 T$ )	8	$\bar{T}, T'^2$
5	c: (TECO49): ozone	8	$\bar{c}$
6	c: (CAAM): ozone	8	$\bar{c}, c'^2$
7	water vapor	8	$\bar{q}, q'^2$
8	open		
9	w: vertical wind speed component	3	$\bar{w}, w'^2$
10	u: horizontal wind speed component	3	$\bar{u}, u'^2$
11	v: horizontal wind speed component	3	$\bar{v}, v'^2$
12	T: temperature	3	$\bar{T}, T'^2$
13	c: (TECO49): ozone	3	$\bar{c}$
14	c: (CAAM): ozone	3	$\bar{c}, c'^2$
15	open		
16	open		
*	Momentum flux	3 & 8	$\bar{w'u'}, \bar{w'v'}$
*	Heat flux	3 & 8	$\bar{w'\theta'}$
*	Ozone flux	3 & 8	$\bar{w'c'}$
*	Horizontal wind speed	3 & 8	$(\bar{u}^2 + \bar{v}^2)^{1/2}$
*	Friction velocity	3 & 8	$(\bar{w'u'})^{1/2}$
*	Drag coefficient	3 & 8	$(\bar{w'u'}) / \bar{u}^2$
*	Horizontal wind rotation angle	3 & 8	$\eta$
*	Vertical wind rotation angle	3 & 8	$\theta$
*	Streamline twist angle	3 & 8	$\beta$
*	Sample frequency	3 & 8	$n_s$
*	No. of samples/sample period	3 & 8	N
*	Covariance rotation matrix	3 & 8	[M]
21X	Temperature gradient	3 & 8	$\Delta \bar{\theta}$

\* Data calculated from data recorded for each height.

21X Data acquired with Campbell model 21X data logger.

bration or alignment could be developed for TECO1 compared to TECO2:

$$\bar{C}_{TECO1} = \bar{C}_{TECO2}(CAAM1) \text{ and } \bar{C}_{TECO1} = \bar{C}_{TECO2}(CAAM2).$$

The results for the week June 27-July 4, 1989, are given as an example:

$$\bar{C}_{TECO1} = 0.927 \bar{C}_{TECO2}(CAAM1) - 1.915 \quad [A-4a]$$

$$\bar{C}_{TECO1} = 0.920 \bar{C}_{TECO2}(CAAM1) - 1.927 \quad [A-4b]$$

These equations are practically congruent and thus both verify the validity of, and give the inherent error in this approach for aligning the two TECOs; that is, [A-4a] and [A-4b] are arrived at independently. The two equations

Table A-2. — Data editing criteria.

Quantity	Criteria	Typical no. of values/week
Reynolds stress	$> 0.0 \text{ m}^2 \text{ s}^{-2}$	15
$ \theta $ : vertical angle	$> + 10^\circ$	11
$ \beta $ : twist angle	$> + 20^\circ$	6
TECO variance	$> 10 \text{ ppb}^2$	15
CAAM variance	$> 0.2 \text{ volts}^2$	5
CAAM covariance	8 m direction $\neq$ 3 m direction	5
CAAM covariance variance	$> 0.011 (\text{volts m})^2 \text{ s}^{-2}$	3
$\sigma_{\partial T / \partial z} / (\partial \bar{T} / \partial z)$	$> 10.00$	16
Temperature variance	$> 1.2 \text{ }^\circ\text{C}^2$	4
Temperature covariance	8 m direction $\neq$ 3 m direction	25
Temperature covariance variance	$> 0.4 (\text{ }^\circ\text{C m})^2 \text{ s}^{-2}$	1
$ \bar{w}'\theta' / (\partial \bar{T} / \partial t) $	$< z$	12
$ \bar{w}'c' / (\partial \bar{c} / \partial t) $	$< z$	Occasional
$ \Delta \bar{\theta} $	$< 0.05$	3
Wind speed*	Raining or not	Variable
Wind Speed	$> 15 \text{ m s}^{-1}$	Occasional
Wind speed difference	$\bar{u}(3) \bar{u}(8)$	20
Wind direction	$230^\circ \geq \text{WD} \geq 190^\circ$	10
$ \Delta \bar{u} $	$< 0.05$	3
Instrument malfunction	Electronic	Occasional
Instrument malfunction	Eoysn-y depleted	Occasional
Instrument malfunction	Calibration	2
Instrument malfunction	Broken Sensor	Occasional

\* Sonic anemometers work incorrectly when wet. Wind speeds  $> 15 \text{ m s}^{-1}$  infer gusts  $> 20 \text{ m s}^{-1}$ , the upper limit for ATI sonic anemometers.

are next averaged and then one of the TECOs is aligned with the other; e.g., the result from [A-4a] and [A-4b]:

$$\bar{c}_{\text{TECO2}}(\text{aligned}) = 0.923 \bar{c}_{\text{TECO2}}(\text{original}) - 1.921 \quad [\text{A-5}]$$

In [A-5]  $\bar{c}_{\text{TECO2}}(\text{aligned})$  is the adjustment of  $\bar{c}_{\text{TECO2}}(\text{original})$  required to bring it into alignment with  $\bar{c}_{\text{TECO1}}$ . Once this procedure is accomplished,  $\Delta \bar{c}$  can be calculated by subtraction. An example of the result of this procedure for May 19th, 1989 (Julian day 139) is shown in figure A-1. The saw-tooth effect of the  $\Delta \bar{c}$  an indication that the TECOs were still not completely aligned. Since the TECOs are switched every other half hour, the use of the information within the differences is in order. Equation [A-6] was applied to the aligned  $\Delta \bar{c}$  data; it is equivalent to smoothing over three points with weights 1/4, 1/2, and 1/4:

$$\Delta \bar{c}(t) = \left[ \frac{\Delta c(t-1)}{4} + \frac{\Delta \bar{c}(t)}{2} + \frac{\Delta c(t+1)}{4} \right] \quad [\text{A-6}]$$

The result is the dashed line in figure A-1.

A separate 4-day test was run on the  $\Delta \bar{c}$  ozone data collection and calculation scheme described above. Commencing midday July 22, 1989 (Julian day 202), the intakes of both TECO49s were connected to the same intake manifold; hence, the same level (8 meters) was

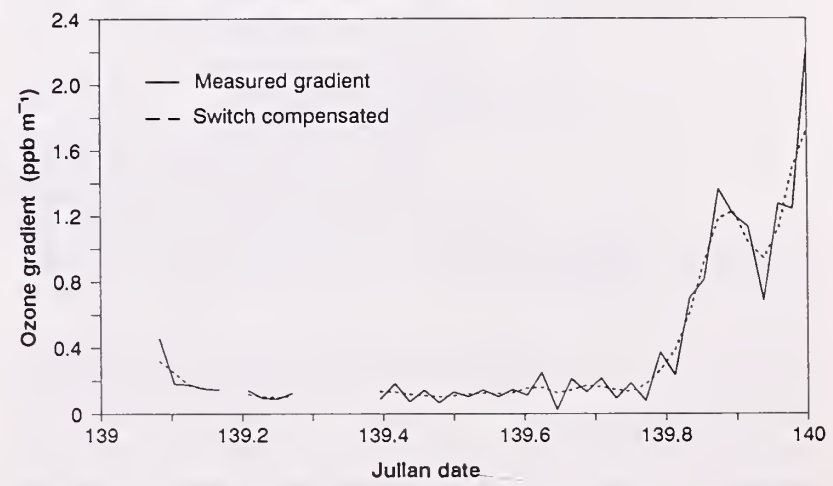


Figure A-1—Detail of ozone gradient data and smoothing (switch compensated) calculation results—May 19, 1989.

sampled by both TECOs. In theory  $\Delta\bar{c}$  should be zero for the period of time both TECOs were sampling the same air.  $\Delta\bar{c}$  data prior to and after midday July 22, 1989, demonstrates the accuracy of the overall  $\Delta\bar{c}$  measurement scheme: for the 4-day test period shown in figure A-2,  $\Delta\bar{c} = + 0.07$  ppb and  $\sigma_{\Delta\bar{c}} = 0.13$  ppb (variance = 0.017 ppb<sup>2</sup>), which represents the bias in the system and the precision of the  $\Delta\bar{c}$  measurement for  $\Delta z = 5$  m.

### Flux Measurement Corrections

Although eddy correlation is the flux-measurement technique of choice, recent attention has been given to the requirement for careful data processing of eddy-correlation data (Businger 1986; Wesely et al. 1989). Businger (1986) lists ten specific items related to flux measurements that researchers in the past have not diligently addressed. In a plea for flux research uniformity, he proposes that the flux correction items listed in table A-3 at least be noted in future research reporting, even if they are not used, so that results can be evaluated on a comparative basis. As indicated, nine applicable areas of concern for gaseous eddy-correlation measurements were considered for the Pawnee site data ana-

lyzed herein. Except for items 1, 2, 6, 7, 8, and 10a, the concerns in table A-3 are not routinely corrected for because they are theoretical in nature and add considerable scatter to the data (Kaimal 1989; Wyngaard 1989a). Flux corrections for items 3 and 4 involve instrument frequency response; these corrections are complicated and are presented in Zeller et al. (1989).

### Effects of Heat and Water Vapor

Webb et al. (1980) provide corrections ([24], Webb et al. 1980) for the effects of heat flux and water vapor flux on mass-flux measurements made with instruments that measure density fluctuations as opposed to mixing-ratio fluctuations. Essentially, gradients of heat and water vapor can cause differences in air density moving upward versus downward. Because the correction for heat is about 5 times that of water (Webb et al. 1980) and because relative humidity is generally low at the Pawnee site [A-7], which accounts for the heat-flux correction only, is used to correct ozone-flux measurements made with the CAAM instruments (Zeller et al. 1989):

$$F_c = F_c(\text{measured}) + \frac{\bar{c} \bar{w}' \theta'}{\bar{\theta}} \quad [\text{A-7}]$$

Table A-3. — List of dry deposition measurement concerns applied to the Pawnee site data set (Businger 1986).

Flux Corrections	Addressed (yes/no)	Affected measurement(s)
1. Effects of heat and water vapor §	yes: ( $\bar{w}'\theta'$ only)	$\bar{w}'c'$
2. Insufficient averaging time	yes <sup>+</sup> : 28.2 min	means, fluxes
3. Inadequate sensor response:		
a. dynamic frequency response	yes*	fluxes, variance
b. sensor mismatching	yes*	$\bar{c}'\bar{w}'$
c. line averaging	yes*	$\bar{u}'\bar{w}'$ , $\bar{w}'\theta'$
d. data logging	yes*	all instruments
e. aliasing	yes*	fluxes, variance
f. volume averaging	yes*	$\bar{w}'c'$
4. Sensor separation	yes*	$\bar{w}'c'$ , $\bar{w}'\theta'$
5. Random noise	no	—
6. Homogeneity and stationarity	yes <sup>+</sup>	fluxes
7. Sampling height	yes <sup>+</sup>	fluxes
8. Inadequate fetch	yes <sup>+</sup>	all measures
9. Deliquescences of particles	NA	NA
10. Flow distortion		
a. mounting structures	yes <sup>+</sup>	vector quantities
b. instrument shadow	yes*	vector quantities

§ The heat flux portion of this correction was applied to all ozone fluxes: both "corrected" and "uncorrected" fluxes referred to in the text have been corrected for heat flux.

\* Evaluated but not corrected for in the eddy diffusivity analyses.

+ Part of data editing criteria (see table A-2).

where  $\bar{\theta}$  is the average potential temperature in °K.

The Webb-Pearmen-Luening correction (Webb et al. 1980), referred to herein as the "heat-flux correction," is the only one routinely made so that  $F_c$  (measured) in [A-7] is the only flux measurement that is actually adjusted on a routine basis. These corrections are generally positive and between 0% and 25% (0 to 0.04 ppb m s<sup>-1</sup>) of the measured ozone flux. The resulting corrected values for  $w'c'$  are therefore less negative or smaller in absolute value.

### Insufficient Averaging Time

The appropriate length of time for a good average in field turbulence measurements is a balance between capturing a statistically significant number of important eddies in the dominant scale while atmospheric conditions remain stationary and homogeneous. Businger (1986) has reviewed this problem and offers the averaging period scale  $T_{\bar{c}}$  as an empirically derived value for estimating the averaging time to determine  $\bar{c}$  with an accuracy of a:

$$T_{\bar{c}} = \frac{20z}{a^2 \bar{u}} \frac{\bar{c}^2}{\bar{c}^2} \quad [A-8]$$

For  $T_{\bar{w}'c'}$ , the corresponding averaging time to determine  $w'c'$  with an accuracy of a (a = 0%, unattainable in practice, means no error):

$$T_{\bar{w}'c'} = \frac{20z}{a^2 \bar{u}} \left( \frac{(\bar{w}'c')^2}{u_*^2 c_*^2} - 1 \right) \quad [A-9]$$

$T$  increases linearly with  $z$ ; therefore for  $z = 8$  m and  $T_{\bar{c}} = 28.2$  minutes, typical average measured values of  $\bar{c}^2 / \bar{c}^2 \approx 0.0017$ , and  $\bar{u} \approx 4.0$  m s<sup>-1</sup> for the week June 13-20, 1989, as an example, gives  $a \approx 0.6\%$ , the accuracy with which  $\bar{c}$  can be measured for the Pawnee site. Using [A-9] with typical values  $u_* = 0.27$  m s<sup>-1</sup>,  $c_* = 0.35$  ppb, and  $(\bar{w}'c')^2 \approx 0.00016$  m<sup>2</sup> ppb<sup>2</sup> s<sup>-2</sup> for the same week in June gives  $a \approx 13.7\%$ , the accuracy with which  $w'c'$  can be expected to be measured within the same 28.2-minute averaging period. The  $T_{\bar{w}'c'}$  value for a, 13.7%, is very reasonable, as Businger (1986) considers values of a = 100% for  $T_{\bar{w}'c'}$  workable based on the fact that the accuracy of  $\bar{c}$  measurements quickly deteriorate when attempting to extract a gradient,  $\Delta \bar{c} / \Delta z$ . This expectation is true for the Pawnee site, based on the data presented in figure A-2, with  $\Delta \bar{c} \approx 0.8$  during the day and  $\Delta \bar{c} \approx 4.0$  ppb at night the accuracy with which  $\Delta \bar{c}$  is made at the Pawnee site ranges from  $a = [(0.07 + 0.13) * 100 / \Delta \bar{c}] = 25\%$  during the day to  $a = 4\%$  at night.

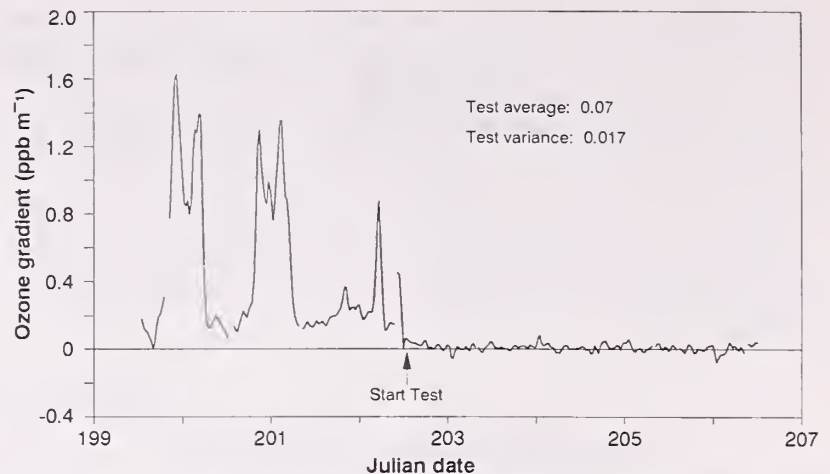


Figure A-2—Demonstration of the accuracy and precision of the ozone gradient measurement—Ozone gradient test: July 21-25, 1989.

### Random Noise

Flux data gathered at the Pawnee site are not adjusted for random noise. With the exception of not employing a Butterworth filter, a significant effort was made to eliminate noise from all sensors and data lines. Ground loops were avoided by grounding signal lines on only one end, the shelter and all systems were grounded, and the data-collection system, PC/DT2805, was operated through an uninterruptable power supply which also provided a constant power source. All 16 input channel data were plotted on the PC screen on a continuous basis. In this way spurious signals and excessive noise in the data were visually detected and eliminated early in the data-collection process. Also, the system was monitored weekly for any changes in sensor performance (Stocker and Lukens 1988).

### Homogeneity and Stationarity

Field micrometeorological measurements never completely satisfy the assumptions of horizontal uniformity and steady-state conditions assumed in the derivation of [7] and [8]. Businger (1986) has provided a gross test for these problems given as follows:

$$h_t = \left| \frac{\frac{w'c'_0}{\partial \hat{c}}}{\frac{\partial \hat{c}}{\partial t}} \right| = \left| \frac{\frac{w'c'}{\partial \hat{c}}}{\frac{\partial \hat{c}}{\partial t}} \right| \quad [A-10]$$

where  $h_t$  is a scaling height, and

$$\frac{\partial \hat{c}}{\partial t} = \frac{1}{z} \int_0^z \frac{\partial \bar{c}}{\partial t} dz$$

If  $h_t \gg z$ , the sampling height, then advection can be disregarded. Data failing the test  $h_t < z$  were eliminated from the analysis herein (see table A-2).

## Sampling Height

Based on reported atmospheric spectra (Caughey 1981; Højstrup 1981; Kaimal et al. 1972; Panofsky and Dutton 1984), measured nondimensional frequencies typically range between:  $10^{-3} \leq f_z / \bar{u} \leq 10$ . Given  $f = 14.6$  Hz and  $\bar{u}$  values between  $1 \text{ m s}^{-1}$  and  $10 \text{ m s}^{-1}$ , theoretically a sampling height of  $z \leq 10 * 1 / 14.6 \approx 70 \text{ cm}$  would be an acceptable measurement height for the Pawnee site system. The sonic anemometer sensing path length becomes the limiting factor near the surface; therefore, 3 meters was chosen as the lowest sampling height for the Pawnee site, based on the eddy-correlation experience of Kaimal (1964) and Haugen et al. (1971) and based on possible chemical reactions between  $\text{O}_3$  and  $\text{NO}_x$  below 2 meters as discussed under Experimental Design. Recently Volkov et al. (1986) have reported valid  $\text{CO}_2$  flux data at 1.7 m height using a 20-cm path length sonic with a 4-Hz sample rate. It is considered that 3 meters is well within eddy-correlation technique height limits reported in the literature.

## Inadequate Fetch

Businger (1986) cites the rule-of-thumb fetch requirement for micrometeorological studies as equal to  $100z$ . The Pawnee site is relatively flat, except for the north-south oriented swale approximately 400 m west of the Pawnee site tower. Analysis of measured  $z_o$  values as functions of wind direction lead to the initial conclusion that this swale is not a problem (Zeller et al. 1989); however,  $K_m$  values reported herein are affected by wind direction. Flux data gathered when the average wind direction was from the instrument shelter and through the tower ( $210^\circ \pm 20^\circ$  azimuth) were disregarded for analysis because of flow distortion (Cermak and Horn 1968). The 3- and 8-meter sampling heights seem to provide an adequate footprint to obtain representative flux measurements. The surface canopy was composed of sparsely vegetated shortgrass prairie (mean plant height  $\sim 25 \text{ cm}$ ) with leaf area indices between 0.4 and 0.6 measured at the Pawnee site during a normal growing season (Zeller and Hazlett 1989).

## Flow Distortion and Shadowing

Flow distortion refers to the deleterious effect of the sensors' geometric configuration and positioning on the quantities being measured because of local changes in the wind-flow patterns. Shadowing refers to the deleterious effect of the flow around the transducers. As stated previously, data associated with upwind directions coming from the instrument shelter and support tower towards the sensor arrays were discarded. By far the most significant impact on wind-related measurements

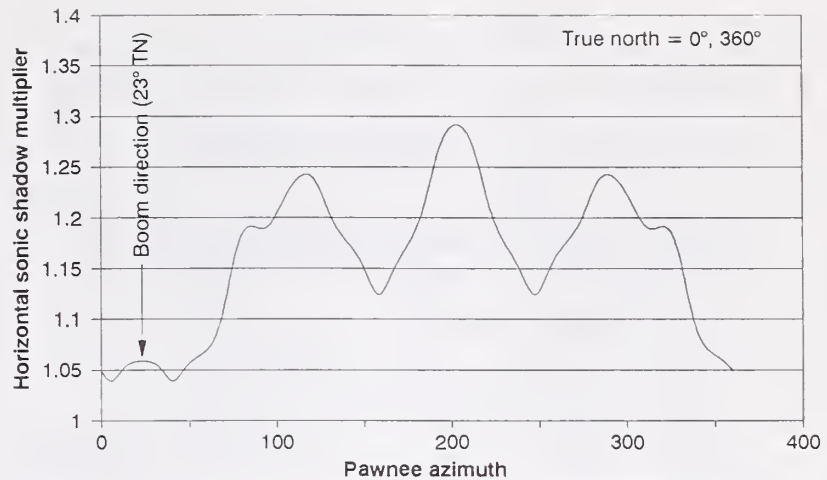


Figure A-3—Composite wind-speed correction as a function of wind direction for the Pawnee-site sonic anemometers.

for the remaining wind directions involves the anemometer itself: transducer shadowing. Sonic anemometer shadowing has only recently been addressed in the literature (Businger 1986; Conklin et al. 1988; Wyngaard and Zhang 1985). The shadowing problem, which results in underestimations in wind velocities because of transducer-generated flow vortices, is currently unresolved and the subject of ongoing research.

Based on the wind-tunnel studies of Conklin (1988) and subsequent tests that have not yet been published (Conklin et al. 1988; Baker 1988), Massman et al. (1990) have constructed a composite flow-distortion correction for wind-speed measurements specific to the ATI, Inc. model BH-478/B3 sonic anemometer. Figure A-3 plots the composite correction multiplier for horizontal wind speeds relative to the Pawnee site configuration and true north (TN) wind direction. The vertical wind component correction for shadowing does not seem to be a function of direction and is taken as 1.16 based on the analysis of Massman et al. (1990). A complete verification of these wind corrections is still wanting. However, based on a comparison of the surface energy balance components between the Pawnee site eddy-correlation measurements and measurements from the nearby CSU soil lysimeter, the corrections can account for differences between the two measurement techniques (Massman et al. 1990).

## Assumptions

A consolidated list of all the assumptions previously discussed or alluded to is provided in table A-4 for completeness. These are assumed to be true throughout the study and in the analysis of the data. The weakest assumptions are horizontal uniformity, satisfactory fetch, and nonreactive trace gas. Analyses of the data show some influence by these factors, as discussed in the main text. The assumption of a logarithmic profile in the surface layer and the resulting choice of 4.9 m as the applicable height for applying the results herein has a directly proportional impact on measured nondimensional gradients, [15a-c].

Table A-4. — Assumptions

1. Stationarity — suspect data records are culled from analyses.
2. Horizontal uniformity — data from wind directions 030° - 250° were analyzed separately from 250° - 030° wind data.
3. Eulerian point average = ensemble average — a 28.2-minute average is sufficient to measure averages, variances, and covariances with a reasonable degree of accuracy.
4. No hot spots or standing waves.
5. Air density is a constant.
6. Coriolis forces are negligible.
7. Satisfactory fetch — data influenced by the swale west of site is analyzed separately from other data.
8. Sensor separation is close enough to provide valid covariance measurements.
9. Ozone can be treated as a nonreactive trace gas between 3 and 8 meters.
10. The analyses of 3- and 8-meter flux and gradient data applies at the geometric mean height of 4.9 meters — (dimensionless gradients are sensitive to the choice of  $z$ ).

## Measurement Errors

Based on the uncertainty interval results shown in table A-5, eddy diffusivities can be estimated with slightly better precision than nondimensional gradients. Sensible heat quantities  $K_h$  and  $\phi_h$  are the best measures, with 10% and 14% uncertainty, respectively, followed by momentum with 24% and 26%, and finally ozone with 40% and 41%. The values chosen for table A-5 and the uncertainty calculations are representative of daytime values, which result in larger uncertainty intervals compared to nighttime measures. Daytime measurement uncertainties for  $K_c/K_m$ ,  $K_h/K_c$ , and  $K_h/K_m$  are  $\pm 41\%$ ,  $\pm 30\%$ , and  $\pm 14\%$ , respectively.

It is impossible to absolutely state the error for the experimentally determined values of  $K_q$  and  $\phi_q$  extracted from the Pawnee site data. This is due to the ever-changing parameters involved, and the basic nature of

micrometeorological field measurements. An “uncertainty interval” can, however, be estimated assuming a linear error with each independent variable (Sandborn 1981). For  $K_q$ , [20], the uncertainty interval,  $\omega_k$ , for eddy diffusivity can be approximated:

$$\omega_K \approx \left[ \left( \frac{\partial K}{\partial (\bar{w}'q')} \right)^2 + \left( \frac{\partial K}{\partial \Delta \bar{q}} \right)^2 + \left( \frac{\partial K}{\partial \Delta z} \right)^2 \right]^{1/2} \quad [A-11]$$

so that

$$\frac{\omega_K}{K} \approx \left[ \left( \frac{\omega_{\bar{w}'q'}}{\bar{w}'q'} \right)^2 + \left( \frac{\omega_{\Delta \bar{q}}}{\Delta \bar{q}} \right)^2 + \left( \frac{\omega_{\Delta z}}{\Delta z} \right)^2 \right]^{1/2} \quad [A-12]$$

For  $\phi_q$ , [15], the uncertainty becomes:

$$\frac{\omega_q}{\phi_q} \approx \left[ \frac{\omega_K^2}{K} + \left( \frac{\omega_{u'w'}}{u'w'} \right)^2 + \left( \frac{\omega_z}{z} \right)^2 + \left( \frac{\omega_k}{k} \right)^2 \right]^{1/2} \quad [A-13]$$

Table A-5 gives the numerical values used to establish uncertainty for  $K_q$ 's and  $\phi_q$ 's for  $\zeta < 0$ . The values in table A-5 are representative of the various measures and no more. They are an attempt to objectively state the uncertainty in each measure. The bases for  $\omega_{\bar{w}'q'}$  in table A-5 are the flux loss estimates provided in Zeller et al. (1989); therefore, the relative  $\bar{w}'q'$  values are 1.0. For ozone,  $\omega_{\Delta \bar{q}}$  is based on figure A-2 and  $\Delta \bar{q}$  on average daytime  $\Delta \bar{c}$  measurements. For temperature,  $\omega_{\Delta \bar{q}}$  is based on the error caused by solar heating. For momentum,  $\omega_{\Delta \bar{q}}$  is based on figure A-3. Table A-5 also presents the uncertainty results, [A-12] and [A-13], in terms of percent error. Uncertainty for the von Karman parameter,  $\omega_k$ , although questioned by some authors (Businger 1986) is not estimated.

Table A-5. — Measurement uncertainty values and percent uncertainty.<sup>+</sup>

Quantity	Ozone	Sensible Heat	Momentum
$\omega_{\bar{w}'q'}$	0.3 (ppb m s <sup>-1</sup> )	0.05 (°C m s <sup>-1</sup> )	0.10 (m <sup>2</sup> s <sup>-2</sup> )
$\omega_{\Delta \bar{q}}$	0.04 (ppb)	0.1 (°C)	0.2 (m s <sup>-1</sup> )
$\omega_{\Delta z}$	0.002 (m)	0.002	0.002
$\omega_z$	0.003 (m)	0.003	0.003
$\omega_{u'w'}$	1.0 (ppb m s <sup>-1</sup> )	1.0 (°C m s <sup>-1</sup> )	1.0 (m <sup>2</sup> s <sup>-2</sup> )
$\Delta \bar{q}$	0.15 (ppb)	1.1 (°C)	0.9 (m s <sup>-1</sup> )
$\Delta z$	5 (m)	5	5
$z$	8 (m)	8	8
$(\omega_k/K)$	40%	10%	24%
$(\omega_\phi/\phi)$	41%	14%	26%

+ daytime only

## APPENDIX B. SPECTRA AND COSPECTRA

### Temperature Spectra

The temperature time-series sampled at 40.32 Hz using AIR, Inc. FT-1A-T platinum resistance temperature sensors at heights 8 and 3 meters between 11:02 and 11:30 MST (Mountain Standard Time) on July 15, 1989, provide an example data set to demonstrate both the response of the sensor used and the validity of sampling at 14 Hz. Fast Fourier Transforms (FFT) require data-set populations of exact powers of 2. In this case the first 65,536 ( $2^{16}$ ) temperature data points were selected out of 68,235 recorded for each height for the 28.2-minute sampling period. Figure B-1a is a log-log plot of 2,048 frequencies for the 8-meter temperature data. The solid curve,  $fS_\theta(f)/\bar{\theta}^2$ , is the empirical spectra [B-1] (Kaimal et al, 1972) multiplied by  $\theta_*^2 / \bar{\theta}^2$ :

$$\frac{fS_\theta(f)}{\theta_*^2} = \begin{cases} 53.4n / (1 + 24n)^{5/3}, & f \leq 0.15 \\ 24.4n / (1 + 12.5n)^{5/3}, & f \geq 0.15 \end{cases} \quad [B-1]$$

where  $n = fz/\bar{u}$ , the nondimensional frequency.

The vertical alignment of Kaimal's theoretical spectrum with that of the data appears to be an art. Several authors "fit" their spectra to Kaimal's (Clark et al. 1982) or normalize relative to one spectral value in the experiment (Volkov et al. 1986). The vertical location of data depends on the number of original data points and frequencies analyzed as well as the energy within the time series. The convention used here is to multiply each power density by  $[\bar{q}^2(\text{field}) / \sigma_q^2(\text{spectrum})]$ .

Figure B-1b is the same as figure B-1a for the 3-meter height. Both figures demonstrate the expected  $-2/3$  eddy cascade in the inertial subrange, and both figures show minimal aliasing at the high-frequency end of the spectra. To test the routine sampling rate, 14 Hz, every third data point was selected from the 8-meter 68,235 point temperature record introduced above to provide a 13.44 Hz data set (i.e.,  $40.32/3$ ). Zeros were added to the

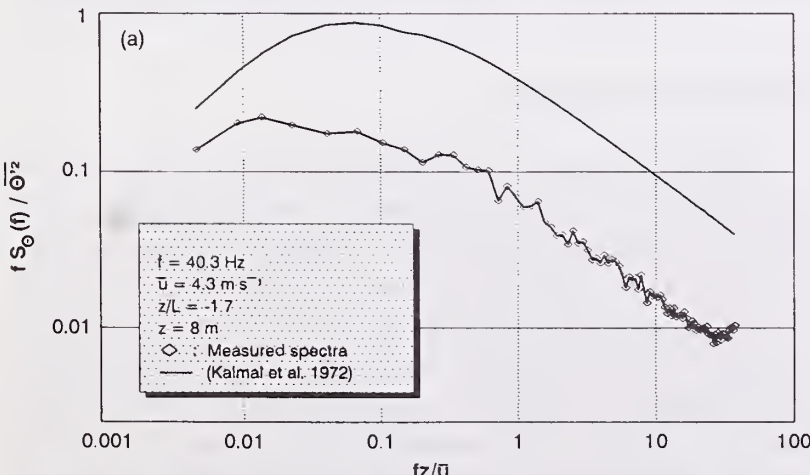


Figure B-1a—Temperature spectra at the Pawnee site, 8-meter data collected at 40.32 hz, 11:02-11:30 MST, July 15, 1989.

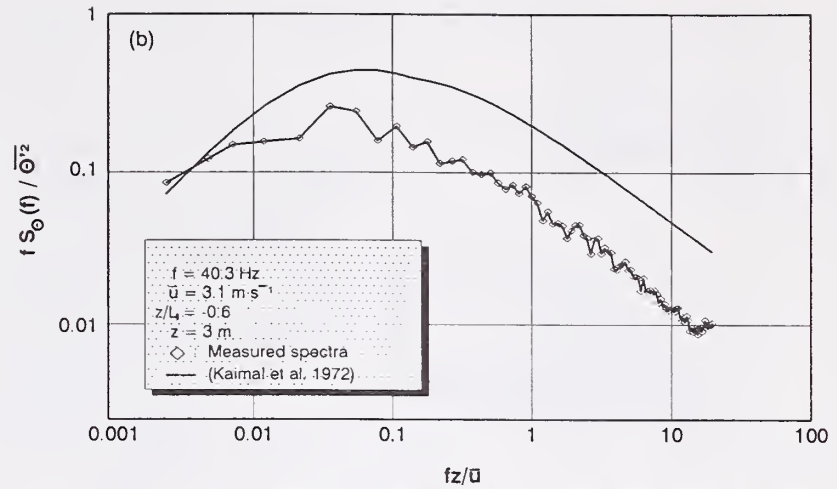


Figure B-1b—Temperature spectra at the Pawnee site, 3-meter data collected at 40.32 hz, 11:02-11:30 MST July 15, 1989.

resulting detrended 22,745 data points to provide a 32,768 point record. Figure B-1c is the same as figure B-1a only for 13.44 Hz rather than 40.32 Hz. Some information is lost at the higher frequencies and the overall spectrum is noisier, even after block averaging; however, the basic shape and variance represented by the lower frequencies is maintained.

These typical spectra results and the recommendation of at least 10 Hz data-acquisition rate (Kaimal 1975) lead to the conclusion that 14 Hz is a reasonable sampling rate for eddy correlation and will provide for the capture of the eddys involved in vertical flux transfer. It is important to note that the spectra in figure B-1a-c are from a single sampling period and are quite reasonable given that [B-1] is the empirical result of many sample period data sets.

### Temperature Cospectra

The temperature cospectra, i.e.  $w'\theta'(n)$  heat flux, for 8 and 3 meters for 23,770 data points collected at 14.04 Hz between 13:32 and 14:00 MST July 7, 1989, are shown in figure B-2. The empirical cospectrum of Kaimal et al. (1972) is depicted by the solid line:

$$\frac{fC_{w\theta}(f)}{u_*\theta_*} = \begin{cases} \frac{11n}{(1 + 13.3n)^{1.75}}, & n \leq 1.0 \\ \frac{4.4n}{(1 + 3.8n)^{2.4}}, & n \geq 1.0 \end{cases} \quad [B-2]$$

where  $C_{w\theta}(f)$  = vertical velocity temperature cospectrum. Each covariance cospectra density was adjusted by the multiplier:

$$\left[ \bar{w}'\theta'^2(\text{field}) / \sigma_w^2 \sigma_\theta^2(\text{cospectrum}) \right]$$

### Vertical Velocity Spectra

Velocity data were collected at 8- and 3-meter heights using Applied Technologies, Inc. model BH-478B/3

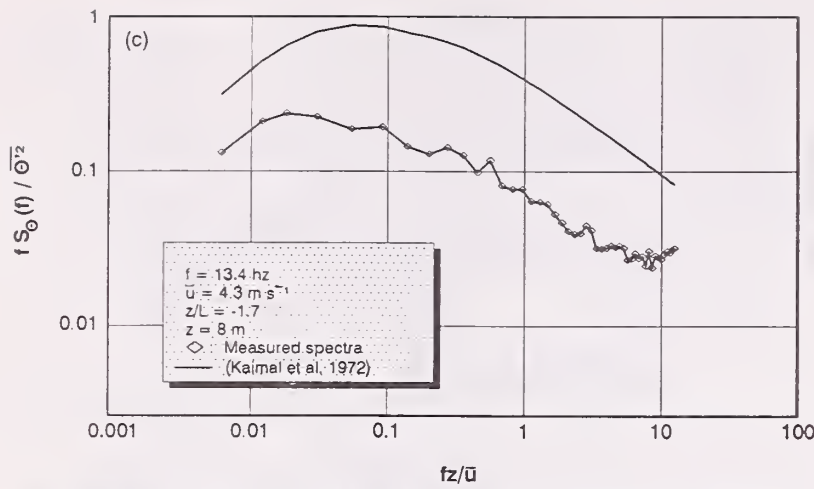


Figure B-1c—Temperature spectra at the Pawnee site, 8-meter data collected at 13.44 hertz, 11:02-11:30 MST, July 15, 1989.

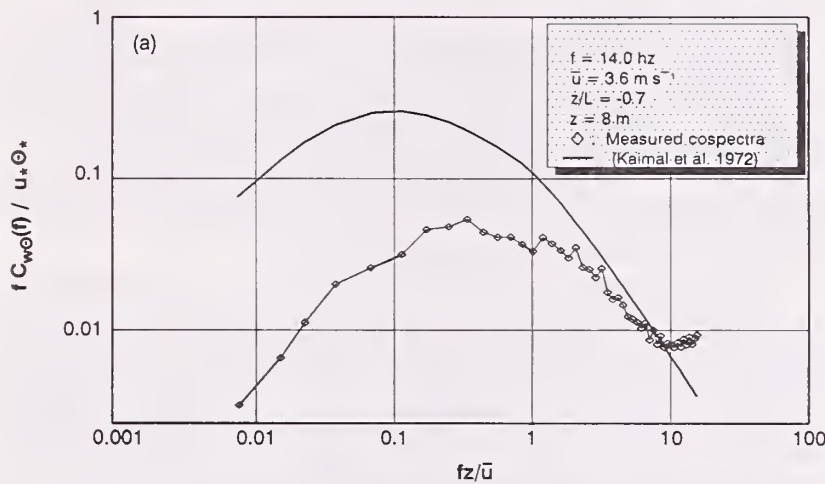


Figure B-2a—Temperature - vertical-velocity cospectra at the Pawnee site, 8-meter data collected at 14.04 hertz, 13:32-14:00 MST July 7, 1989.

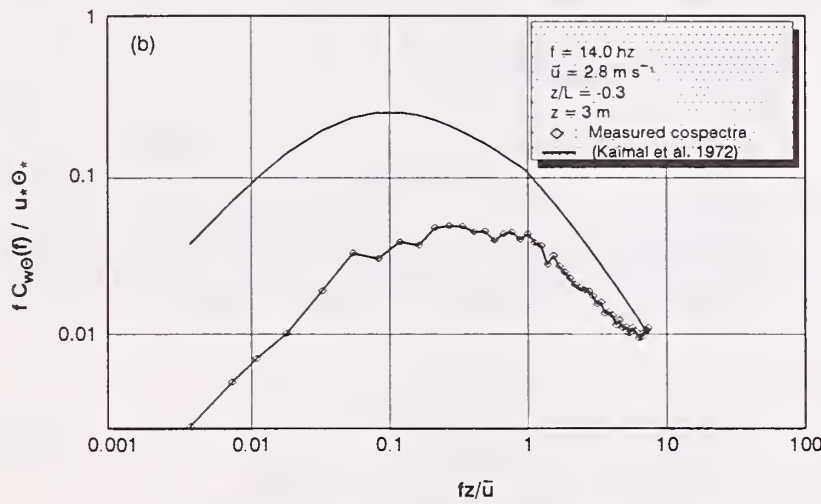


Figure B-2b—Temperature - vertical-velocity cospectra at the Pawnee site, 3-meter data collected at 14.04 hertz, 13:32-14:00 MST July 7, 1989.

sonic anemometers. Figure B-3 shows the vertical velocity spectra for 23,770 data points collected for each height at 14.04 Hz between 13:32 and 14:00 MST on July 7, 1989. Each set was prepared as previously discussed.

The solid curve in figures B-3a and B-3b is the empirical curve for unstable and neutral conditions suggested by Høstrup (1981):

$$\frac{fS_w(f)}{u_*^2} = \frac{32n}{(1+17n)^{5/3}} \zeta^{2/3} + \frac{2n}{(1+5.3n)^{5/3}} \quad [B-3]$$

Note that the spectra in the inertial subrange of figure B-3 fall short of the expected  $-2/3$  slope. This loss in variance is due to an analog filter installed by the sonic manufacturer to provide an equivalent 10-Hz signal; it does not result in any significant loss in measured fluxes (Kaimal 1989). The researcher has the alternative choice of monitoring a digital signal directly from sonic sensor. The analog output was used for the flux measurements discussed herein.

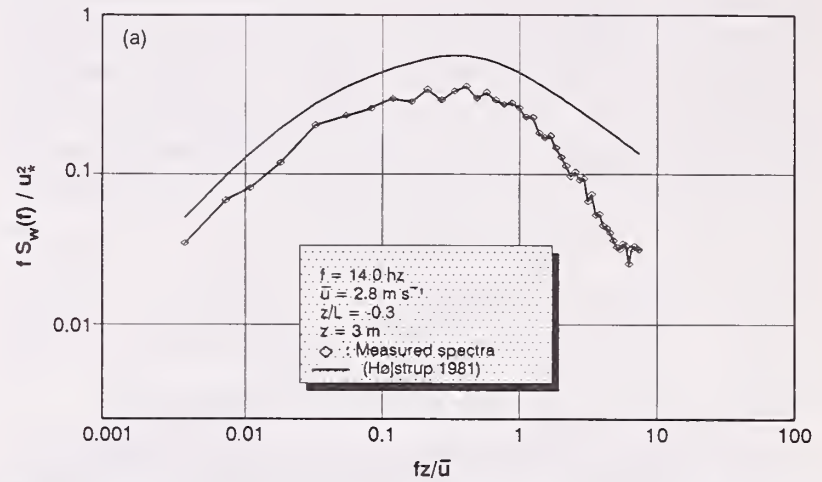


Figure B-3a—Vertical-velocity spectra at the Pawnee site, 8-meter data collected at 14.04 hertz, 13:32-14:00 MST, July 7, 1989.

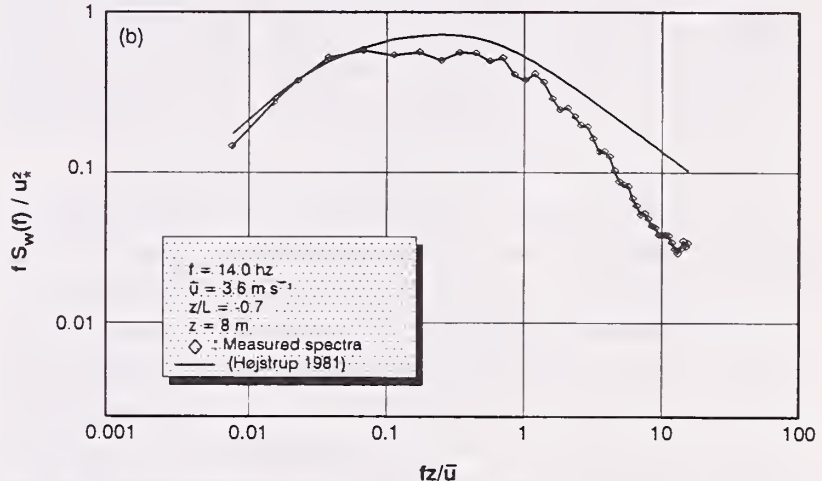


Figure B-3b—Vertical-velocity spectra at the Pawnee site, 3-meter, data collected at 14.04 hertz, 13:32-14:00 MST, July 7, 1989.

### CAAM Ozone Spectra

Figure B-4 shows the spectra for the CAAM (ozone) data collected from the 8-meter level on July 7, 1989 between 13:32 and 14:00 MST. The solid curve in figure B-4 is [B-1] for  $fS_c(f)/c_*^2$ . The tail at the high frequency end of the spectra starts between  $1/f = 1.5$  to  $2.0$  seconds. This feature is aliasing due to the CAAM instrument response and the effect of the intake system. This aliasing feature was also experienced in the 3-meter spectra. The CAAM signal aliasing did not seem to affect flux measurements, as presented next.

## CAAM (Ozone) Cospectra

The CAAM or ozone cospectra,  $w'c'(n)$  ozone flux, for 8 and 3 meters for 23,770 data points collected at 14.04 Hz between 13:32 and 14:00 MST, July 7, 1989, is presented in figure B-5. The solid curve is [B-2] with  $C_{wc}(f)$  and  $c_*$  replacing the values for temperatures as all scalars are expected to behave similarly. The relative location of the empirical cospectrum to the data cospectrum would indicate either that the covariance loss is greater with the CAAM instruments than it is with the platinum resistance temperature sensors or that there is relatively less ozone transport. Some loss is expected and has been noted before (Kristensen and Fitzjarrald 1984; Moore 1986; Zeller et al. 1989).

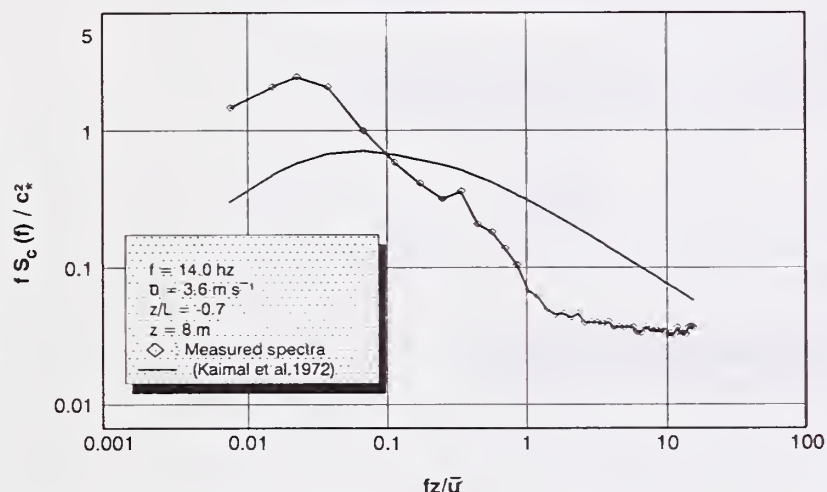


Figure B-4—Ozone spectra at the Pawnee site, 8-meter data collected at 14.04 hertz, 13:32-14:00 MST July 7, 1989.

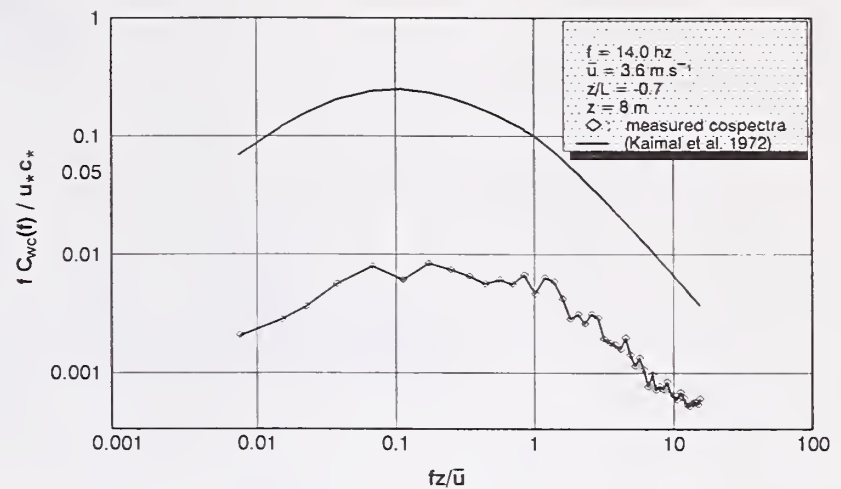


Figure B-5a—Ozone - vertical-velocity cospectra at the Pawnee site, 8-meter data collected at 14.04 hertz, 13:32-14:00 MST July 7, 1989.

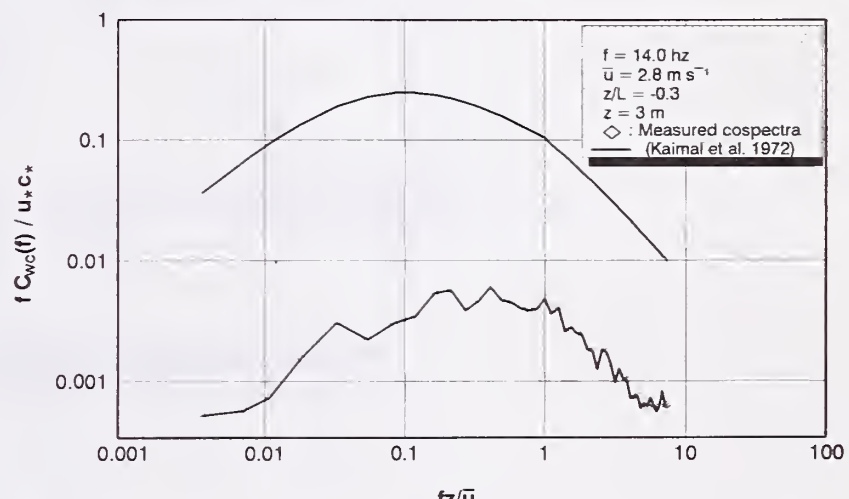


Figure B-5b—Ozone - vertical-velocity cospectra at the Pawnee site, 3-meter data collected at 14.04 hertz, 13:32-14:00 MST July 7, 1989.

## APPENDIX C DATA PLOTS

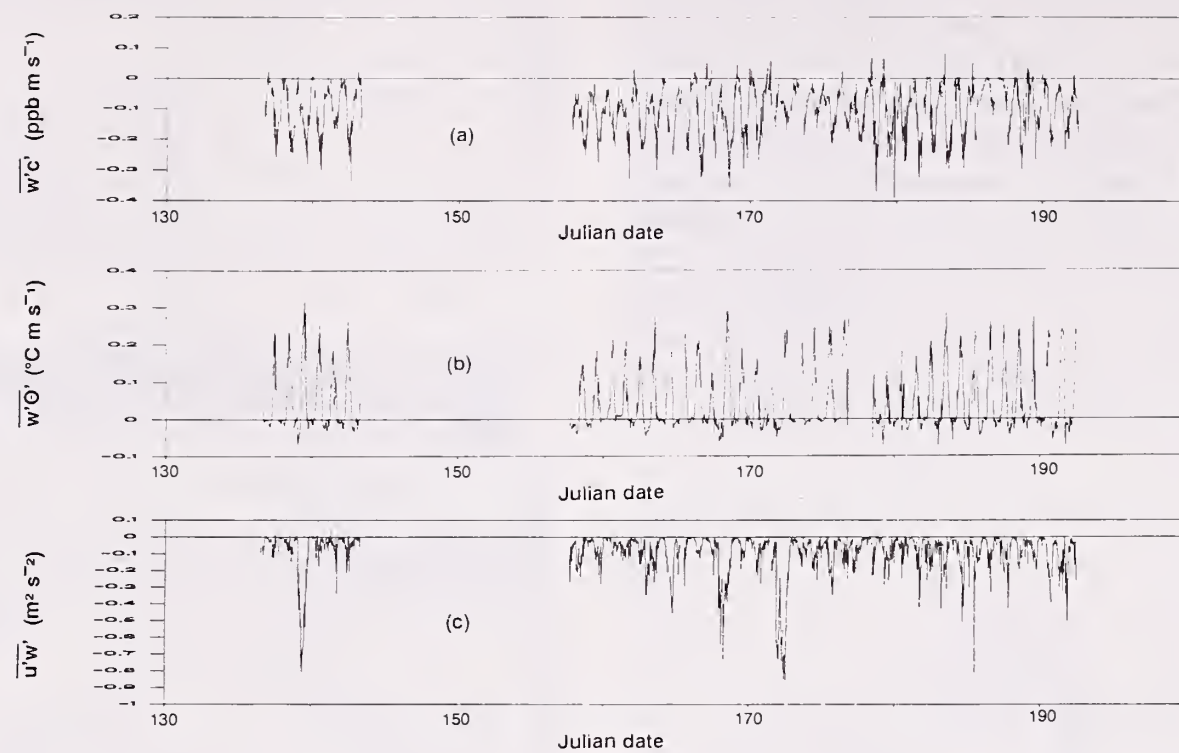


Figure C-1—Unedited flux data: (a) ozone; (b) sensible heat; and (c) momentum.

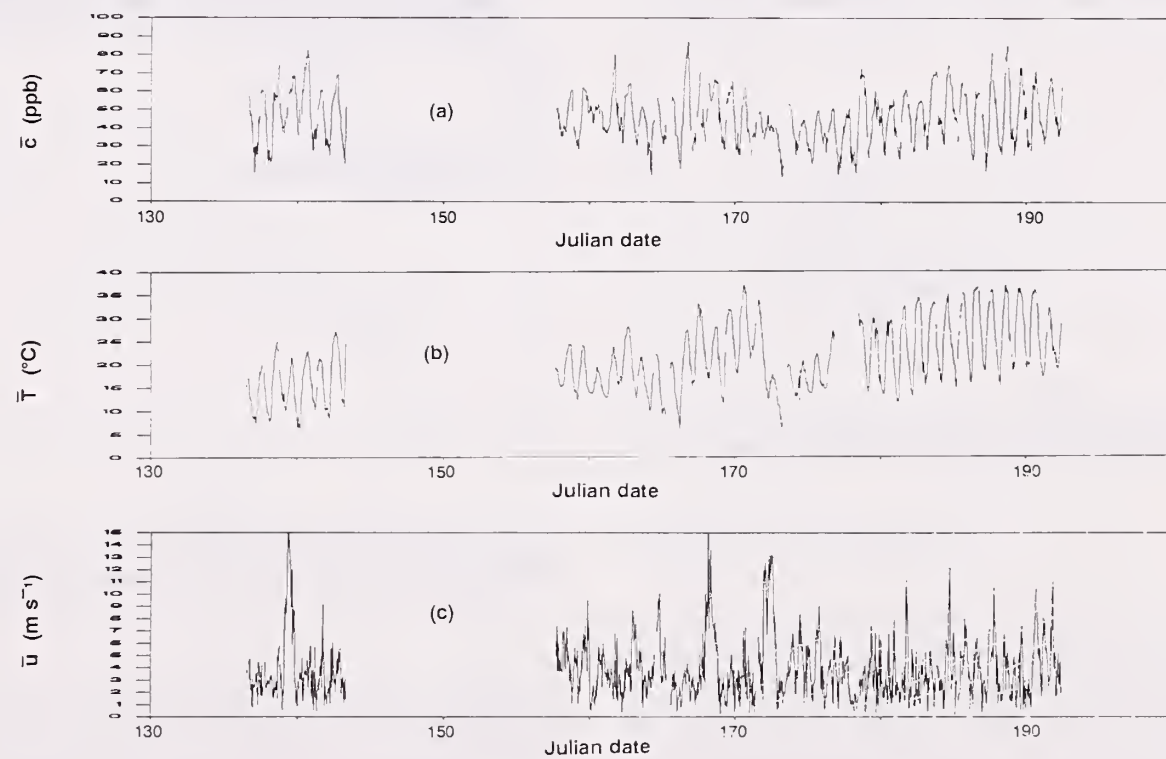
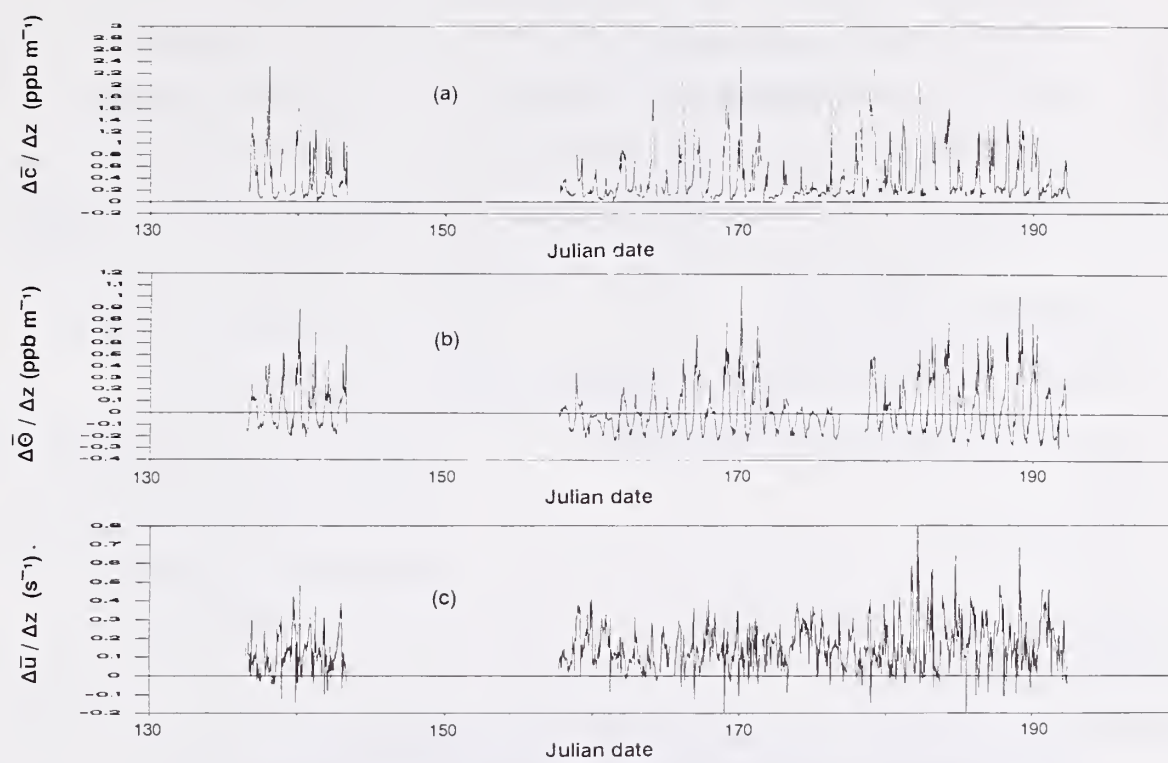
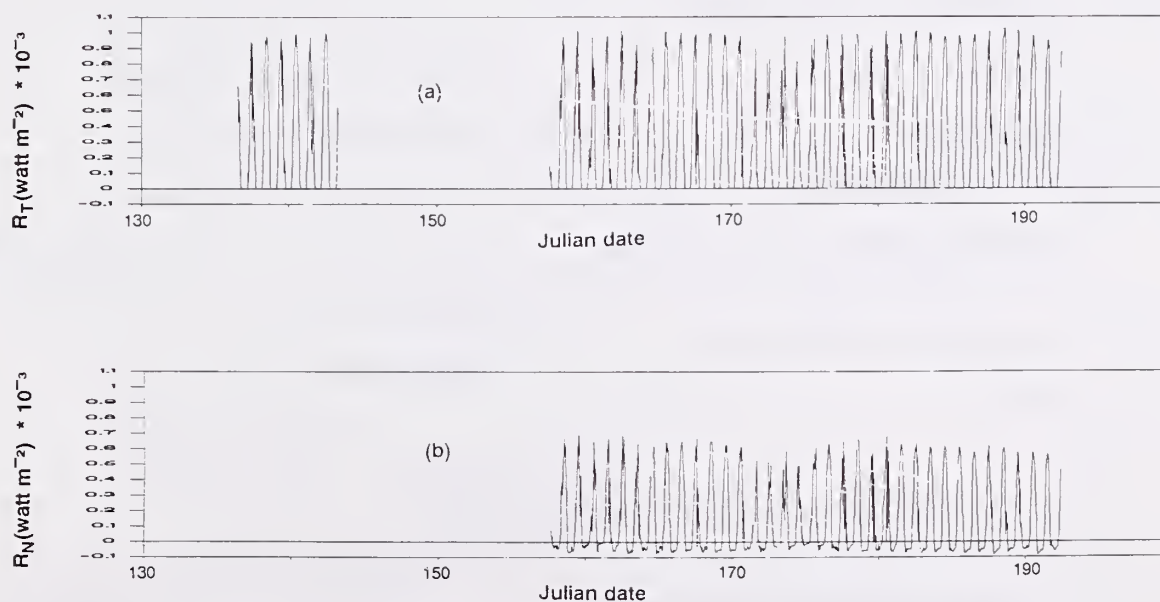


Figure C-2—Unedited data: (a) ozone concentration; (b) temperature; and (c) wind speed.



**Figure C-3—Unedited data: (a) ozone gradient; (b) potential temperature gradient; and (c) horizontal wind speed gradient.**



**Figure C-4—Unedited data: (a) total solar radiation; and (b) net radiation.**

## APPENDIX D. TABLE OF SYMBOLS

<u>Symbol</u>	<u>Definition</u>	<u>Unit</u>
a	% accuracy expected for average time $T$	
c	pollutant ozone concentration	$\text{g m}^{-3}$ ; or ppb
$c_*$	ozone concentration scale ( $\overline{w'c'}/u_*$ )	ppb
$C_p$	specific heat at constant pressure	$1005 \text{ J kg}^{-1} \text{ }^{\circ}\text{K}^{-1}$
$C_{wq}(n)$	atmospheric cospectrum of w and q as a function of n	$\text{m s}^{-1}\text{ppb}$ ; $\text{m s}^{-1}\text{ }^{\circ}\text{K}$ ; $\text{m}^2 \text{ s}^{-2}$
$D_c$	molecular diffusivity	$\text{cm}^2 \text{ s}^{-1}$
$f$	nondimensional frequency ( $n \overline{u}/z$ )	
$F_c$	measured pollutant (ozone) flux	$\text{gm m}^{-2} \text{ s}^{-1}$ ; or ppb $\text{m s}^{-1}$
$F_q$	flux of q	$\text{gm m}^{-2} \text{ s}^{-1}$ ; or ppb $\text{m s}^{-1}$
$g$	acceleration due to gravity	$\text{m s}^{-2}$
H	sensible heat flux	$\text{gm m}^{-2} \text{ s}^{-1}$
$H_{wq}(n)$	total cospectral response function for vertical wind w and quantity q as a function frequency	
k	von Karman constant	
$K_q$	eddy diffusivity of quantity q	$\text{cm}^2 \text{ s}^{-1}$
L	Monin-Obukov length, $\frac{-u^3 \overline{T}}{kg \overline{w' \theta'}}$	m
[M]	covariance rotation matrix	
n	frequency (hertz)	$\text{s}^{-1}$
$\bar{n}$	unit reactor	
$n_s$	sampling frequency	$\text{s}^{-1}$
q	specific density of an arbitrary measured quantity or any quantity	$\text{gm m}^{-3}$ ; ppb; or $\text{m s}^{-1}$
rho	correlation coefficient ( $\rho$ )	
R	radius	m
Ri	gradient Richardson number, $g \frac{\partial \bar{\theta}}{\partial z} / \bar{\theta} \left( \frac{\partial \bar{u}}{\partial z} \right)^2$	
$S_q(n)$	variance spectra density for any quantity q as a function of n	$\text{ppb}^2$ ; ${}^{\circ}\text{K}^2$ ; or $\text{m}^2 \text{ s}^{-2}$
t	time	s
T	temperature	${}^{\circ}\text{C}$ ; or ${}^{\circ}\text{K}$

$T_d(n)$	response function for dynamic frequency response	
$T_l(n)$	response function for line averaging	
$T_m(n)$	response function for mismatched sensors	
$T_R(n)$	response function for high-pass recursive filter	
$T_s(n)$	response function for sensor separation	
$T_v(n)$	response function for volume averaging	
$T$	time scale for averaging time to obtain a % accuracy	s
$u$	horizontal wind speed	$m s^{-1}$
$u_*$	friction velocity, $\sqrt{-u'w'} = \sqrt{\tau_0 / \rho}$	$m s^{-1}$
$v$	water vapor density	$g m^{-3}$
$V_d$	deposition velocity	$cm s^{-1}$
$w$	vertical wind speed	$m s^{-1}$
$\overline{w'c'}$	ozone flux	ppb $m s^{-1}$ ; or gm $m^{-2} s^{-1}$
WD	wind direction related to true north	Degree
$x_i$	ith coordinate ( $x_1 = x$ ; $x_2 = y$ , $x_3 = z$ )	
$y_i$	$= k_i/k_1$ , $i = 2,3$	
$z$	vertical coordinate	m
$z_o$	roughness length	cm
$\alpha$	$K_h/K_m$	
$\gamma_q$	$\phi_q(\text{measured})/\phi_q(\text{empirical})$	
$\Gamma$	adiabatic lapse rate	$0.0098 \text{ } ^\circ\text{K } m^{-1}$
$\zeta$	stability parameter ( $z/L$ )	
$\eta$	horizontal wind rotation angle	radians
$\theta$	potential temperature, or verticale angle of mean wind vector	$^\circ\text{K}$ ; or radians
$\theta_*$	temperature scale $\overline{w'\theta'}/U_*$	$^\circ\text{K}$
$k_1$	wave number in x direction	cycles $m^{-1}$
$\lambda$	latent heat of evaporation	$2.45 \times 10^6 J \text{ kg}^{-1}$
$\lambda E$	latent heat flux	$gm m^2 s^{-1}$
$\rho$	density of air	$g m^{-3}$
$\sigma_\theta^2$	temperature variance	$^\circ\text{K}^2$
$\sigma_c^2$	variance of c	ppb $^2$
$\sigma_w^2$	vertical velocity variance	$m^2 s^{-2}$

$\tau$	momentum flux; and sensor response time	gm m <sup>-1</sup> s <sup>-2</sup> ; s
$\tau_o$	surface sheer stress	gm m <sup>-1</sup> s <sup>-2</sup>
$\phi_c$	dimensionless ozone gradient, $\frac{kz}{c_*} \frac{\partial \bar{c}}{\partial z}$	
$\phi_h$	dimensionless sensible heat gradient = $\frac{kz}{\theta_*} \frac{\partial \bar{\theta}}{\partial z}$	
$\phi_m$	dimensionless wind shear = $\frac{kz}{u_*} \frac{\partial \bar{u}}{\partial z}$	
$\varphi$	phase angle due to sensor mismatch	radians
$\psi_q$	universal stability influence function	
$\omega_q$	uncertainty interval for q	

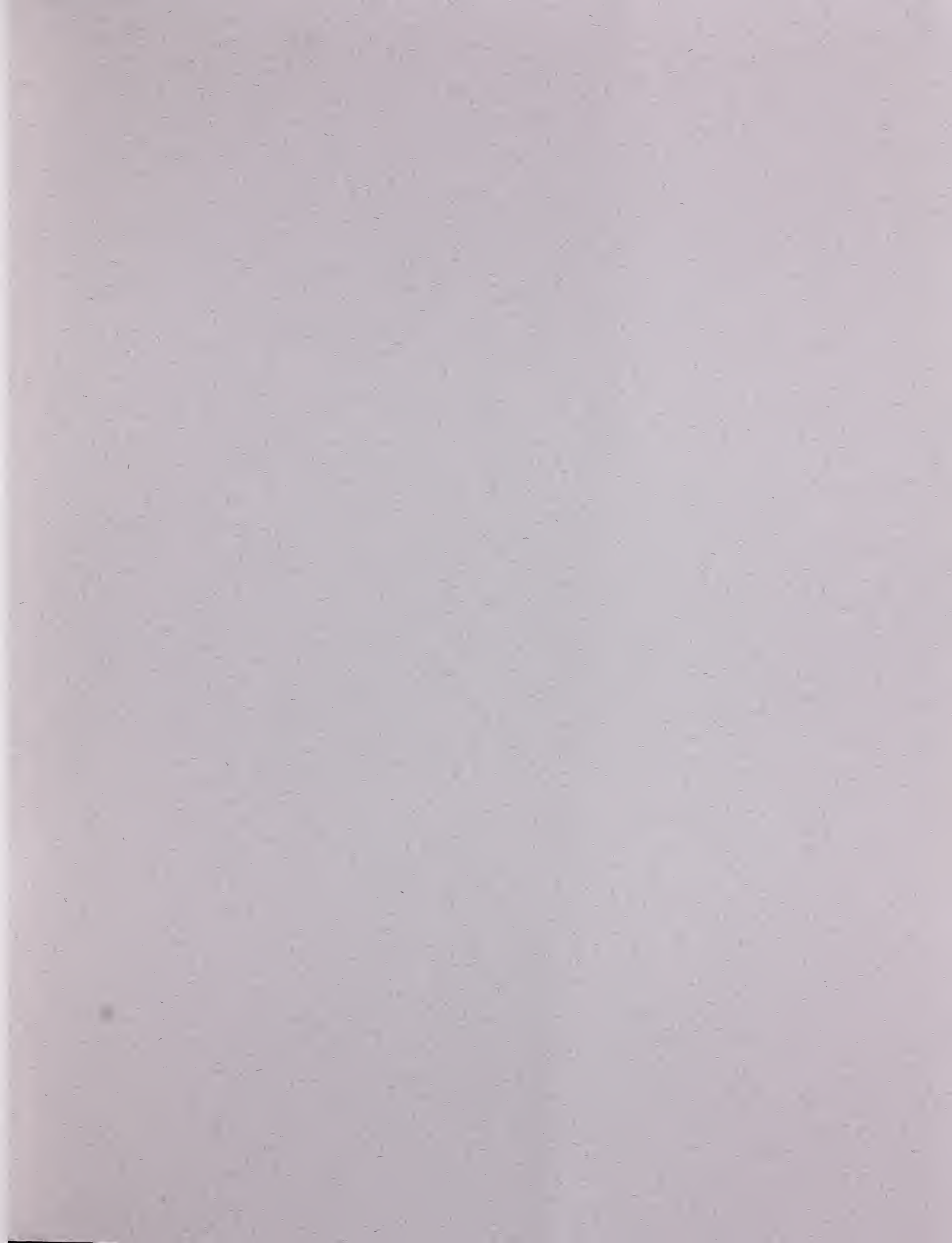
Zeller, Karl. 1993. Eddy diffusivities for sensible heat, ozone, and momentum from eddy correlation and gradient measurements. Res. Pap. RM-313. Fort Collins, CO: U.S. Department of Agriculture, Forest Service, Rocky Mountain Forest and Range Experiment Station. 44 p.

A method developed to accurately measure trace gas mass (ozone) fluxes and gradients from dry grassland canopy using surface-layer-based meteorological towers to investigate the behavior of eddy diffusivities in the atmospheric surface layer.

**Keywords:** Eddy correlation, dry deposition, Pawnee Grasslands, O<sub>3</sub>, micrometeorology, eddy correlation, trace gas fluxes, ozone deposition, eddy diffusivity, sensible heat flux, atmospheric surface layer, Monin-Obukov Similarity.

"The policy of the United States Department of Agriculture Forest Service prohibits discrimination on the basis of race, color, national origin, age, religion, sex, or disability, familial status, or political affiliation. Persons believing they have been discriminated against in any Forest Service related activity should write to: Chief, Forest Service, USDA, P.O. Box 96090, Washington, DC 20090-6090."







Rocky  
Mountains



Southwest



Great  
Plains

U.S. Department of Agriculture  
Forest Service

## Rocky Mountain Forest and Range Experiment Station

The Rocky Mountain Station is one of eight regional experiment stations, plus the Forest Products Laboratory and the Washington Office Staff, that make up the Forest Service research organization.

### RESEARCH FOCUS

Research programs at the Rocky Mountain Station are coordinated with area universities and with other institutions. Many studies are conducted on a cooperative basis to accelerate solutions to problems involving range, water, wildlife and fish habitat, human and community development, timber, recreation, protection, and multiresource evaluation.

### RESEARCH LOCATIONS

Research Work Units of the Rocky Mountain Station are operated in cooperation with universities in the following cities:

Albuquerque, New Mexico  
Flagstaff, Arizona  
Fort Collins, Colorado\*  
Laramie, Wyoming  
Lincoln, Nebraska  
Rapid City, South Dakota

\*Station Headquarters: 240 W. Prospect Rd., Fort Collins, CO 80526